ANALYSIS AND DESIGN OF MATCHED FEEDS FOR OFFSET PARABOLIC REFLECTOR ANTENNAS USING ANALYTICAL AND NUMERICAL TECHNIQUES

A

Thesis submitted

for the award of the degree of

DOCTOR OF PHILOSOPHY

By

Rajib Jana

Department of Electronics and Electrical Engineering

INDIAN INSTITUTE OF TECHNOLOGY GUWAHATI

GUWAHATI - 781 039, ASSAM, INDIA

JANUARY 2016

भारतीय प्रौद्योगिकी संस्थान गुवाहाटी
Indian Institute of Technology Guwahati

ANALYSIS AND DESIGN OF MATCHED FEEDS FOR OFFSET PARABOLIC REFLECTOR ANTENNAS USING ANALYTICAL AND NUMERICAL TECHNIQUES

A

Thesis submitted

for the award of the degree of

DOCTOR OF PHILOSOPHY

By

Rajib Jana

Department of Electronics and Electrical Engineering

INDIAN INSTITUTE OF TECHNOLOGY GUWAHATI

GUWAHATI - 781 039, ASSAM, INDIA

JANUARY 2016

भारतीय प्रौद्योगिकी संस्थान गुवाहाटी
Indian Institute of Technology Guwahati

Certificate

This is to certify that the thesis entitled "**ANALYSIS AND DESIGN OF MATCHED FEEDS FOR OFFSET PARABOLIC REFLECTOR ANTENNAS USING ANALYTICAL AND NUMERICAL TECHNIQUES**", submitted by **Rajib Jana** (09610210), a research scholar in the *Department of Electronics and Electrical Engineering, Indian Institute of Technology Guwahati*, for the award of the degree of **Doctor of Philosophy**, is a record of an original research work carried out by him under my supervision and guidance. The thesis has fulfilled all requirements as per the regulations of the institute and in my opinion has reached the standard needed for submission. The results embodied in this thesis have not been submitted to any other University or Institute for the award of any degree or diploma.

Dated:

Guwahati.

Prof. Ratnajit Bhattacharjee
Department of Electronics and Electrical Engineering
Indian Institute of Technology Guwahati
Guwahati - 781 039, Assam, India.

भारतीय प्रौद्योगिकी संस्थान गुवाहाटी
Indian Institute of Technology Guwahati

To

My dear mom

Kajal bala Jana

for her love and support

&

My siblings

Sanjoy Jana and Sarmila Mondal

for their encouragement

भारतीय प्रौद्योगिकी संस्थान गुवाहाटी
Indian Institute of Technology Guwahati

Acknowledgements

First and foremost, I feel it as a great privilege in expressing my deepest and most sincere gratitude to my supervisor Prof. Ratnajit Bhattacharjee, for his excellent guidance throughout my study. His kindness, dedication, hard work and attention to detail have been a great inspiration to me. My heartfelt thanks to you sir for the unlimited support and patience shown to me. I would particularly like to thank him for all his help in patiently and carefully correcting all my manuscripts.

I am also very thankful to my doctoral committee members Prof. Anup Kumar Gogoi, Dr. Kshetrimayum Rakhesh Singh and Dr. Tarak Nath Dey for sparing their precious time to evaluate the progress of my work. I express my heartfelt thanks to Dr. Brijesh Kumar Rai for his suggestions.

I would also like to thank the Head of the Department and the other faculty members for their kind help in carrying out this work. I am also grateful to all the members of the research and technical staff of the department without whose help I could not have been completed this thesis. My special thanks to Sanjib Das sir and Utpal Kumar Sarma sir for maintaining an excellent computing facility and various resources useful for the research work.

Thanks go out to all my friends at the microwave and communication Laboratories. They have always been around to provide useful suggestions, companionship and created a peaceful research environment. They all contributed directly or indirectly to this thesis, be it academic help, proofreading and volunteering to be a test subject.

I have no words to express my thanks to most important persons namely, Sayantan Hazra, Sanjoy Mondal, Om Prakash Singh, Rajiv Panigrahi, Ramesh Chandra Mishra, Kuntal Deka, Haris B.C and Himanshu Bhaumik. My work in this remote place definitely would not be possible without their love and care that helped me to enjoy my new life in this IITG.

I thank all my fellow research students and M. Tech students for their cooperation. During these four years at IITG I have had several friends that have helped me in several ways, I would like to say a big thank you to all of them for their friendship and support.

I also acknowledge my thankfulness for being given an opportunity to get associated with a project from ISRO (project title: Analysis and development of Matched feed for offset parabolic antenna system, project id: OGP65) in the initial stage of my research which helped me to understand the problems that exist in design of such systems and formulate my research problems accordingly. I also

thankfully acknowledge the help extended by Mr. Satyajit Chakraborty of SAMEER Kolkata center in carrying out the measurements of some proposed feed structures.

My deepest gratitude goes to my family for their continuous love and support throughout my studies. The opportunities that they have given me and their unlimited sacrifices are the reasons where I am and what I have accomplished so far.

Finally, I believe this research experience will greatly benefit my career in the future.

Rajib Jana

Abstract

This research deals with the analysis and design of few novel matched feed structures for offset parabolic reflector antenna systems. An effective hybrid numerical technique is developed to evaluate the performance of a complete system of feed and reflector which reduces computation time and memory requirement at the same time maintain appropriate level of accuracy. The hybrid technique is formed by using the combination of mode matching (MM) and 2-D finite element method (FEM) for interior field analysis of horn; method of moment (MoM) solution for Kirchoff Huygen's equation using Rao, Wilton and Gilsson (RWG) basis functions for open ended waveguide problem; physical optics (PO) to evaluate the far field radiation pattern of the reflector. The performance of this technique is compared with simulated results of HFSS and close match is obtained. Further, particle swarm optimization (PSO) technique and analytical or computed semi-analytical far field pattern of feed aperture using the available analytical or 2-D FEM based solution of Helmholtz equation respectively, are incorporated for conjugate matching to estimate the mode coefficients and relative phases in the matched feed design. In this thesis, the details of conjugate matching and matched feed design is investigated and also, few novel matched feed configurations are introduced. The proposed matched feed structures reported in this thesis have the ability to achieve the wide bandwidth for both return loss and conjugate matching.

Keywords: Matched feed, offset parabolic reflector, mode matching, 2-D finite element method, method of moment, Rao, Wilton and Gilsson basis functions, physical optics, Particle Swarm Optimization.

भारतीय प्रौद्योगिकी संस्थान गुवाहाटी
Indian Institute of Technology Guwahati

Contents

List of Figures

List of Tables

List of Acronyms

CAD	Computer Aided Design
CST MWS	Computer Simulation Technology Microwave Studio
dB	Decibel
EM	Electromagnetic
FD	Finite Difference
FDTD	Finite Difference Time Domain
FEM	Finite Element Method
FIT	Finite Integral Technique
GO	Geometric Optics
GSP	Generalized Scattering Parameter
GTD	Geometric Theory of Diffraction
HFSS-14/15	High Frequency Structural Simulator version-14/15
MATLAB	Matrix Laboratory
MM	Mode Matching
MoM	Method of Moment
PO	Physical Optics
PTD	Physical Theory of Diffraction
PSO	Particle Swarm Optimization
RTS	Rectangular to Spherical Transformation
STR	Spherical TO RectangularTransformation
TE	Transverse Electric
TM	Transverse Magnetic
TEM	Transverse Electromagnetic

2-D	Two-dimensional
3-D	Three-dimensional

List of Symbols

F	Focal length of offset parabolic reflector
D	Diameter of offset parabolic reflector
H	Offset height of reflector
α	Tilt angle of feed
θ_F	Half illuminated angle of offset parabolic reflector
$\{X_A,\ Y_A,\ Z_A\}$	Coordinate of reflector
$\{X_F,\ Y_F,\ Z_F\}$	Feed axis or excitation axis of reflector
$\{X_R,\ Y_R,\ Z_R\}$	Radiation axis of reflector
∇	Del or Nabla
$\times$	Cross product
$\cdot$	Dot product
$\vec{E}$	Electric field
$\vec{H}$	Magnetic field
Ψ	Scaler potential
Ψ_t^e	Tangent part of scaler potential for electric field
Ψ_t^h	Tangent part of scaler potential for magnetic field
γ	Propagation constant
J_n	First kind bessel function
J_n'	Derivative of first jind bessel function
x_{np}	p^{th} root of J_n bessel function
x_{np}'	p^{th} root of J_n' bessel function
$a \times b$	Dimensions of rectangular waveguide
r	Radius of circular waveguide

μ	Permeability
ϵ	Permittivity
$\hat{n}$	Unit vector of normal
$\hat{u}_z$	Unit vector in z direction
e	Normalized tangent electric field
h	Normalized tangent magnetic field
A^+	Forward cofficent
A^-	Backward cofficent
Z_0^e	TE mode impedance
Z_0^h	TM mode impedance
$\vec{E}_t$	Tangential electric field
$\vec{H}_t$	Tangential magnetic field
$\mathbf{S} = \begin{bmatrix} S_{11} & S_{12} \\ S_{21} & S_{22} \end{bmatrix}$	Scattering parameters
P	Reaction matrix
$\phi_{e_i}^n$	Scaler potential of i^{th} node of n^{th} element
$\mathbf{C}_e^n$ $\mathbf{T}_e^n$	Local coefficient matrix of n^{th} element
C T	Global coefficient matrix in the FEM solution
$[\alpha_1\ \alpha_2\ \alpha_3...]$	Shape function
$[\phi_f]$	Free node scaler potential
$[\phi_p]$	Prescribed node scaler potential
ϕ_s^e	TE mode scaler potential of smaller waveguide
ϕ_s^h	TM mode scaler potential of smaller waveguide
ϕ_b^e	TE mode scaler potential of bigger waveguide
ϕ_b^h	TM mode scaler potential of bigger waveguide
e_s^e	TE mode electric field of smaller waveguide
e_s^h	TM mode electric field of smaller waveguide
e_b^e	TE mode electric field of bigger waveguide
e_b^h	TM mode electric field of bigger waveguide
k_s	Mode cutoff value of smaller waveguide

k_b	Mode cutoff value of bigger waveguide
L_s	Boundary of smaller waveguide
Ω_s	Surface of smaller waveguide
$\vec{J}_{S_R}$	Approximated surface current for PO with respect to radiation axis
$\hat{n}_R$	Normal of offset reflector with respect to radiation axis
$\vec{H}_{i_R}(\hat{i}_R,\ \hat{j}_R,\ \hat{k}_R)$	Incident magnetic field on the reflector with respect to radiation axis
k	Free space wavenumber
$r_R,\ \theta_R,\ \phi_R$	Field observation point with respect to radiation axis
$\vec{E}_R(\theta_R, \phi_R)$	Radiated field with respect to radiation axis
$\mathbf{R}_{\mathrm{Eu}}$	Euler transform matrix

भारतीय प्रौद्योगिकी संस्थान गुवाहाटी
Indian Institute of Technology Guwahati

List of Publications

Journal Publications:

1. R. Jana and R. Bhattacharjee, "Matched feed design employing TE_{01} and TM_{11} modes in a smooth walled rectangular waveguide for cross-polar reduction in offset reflector antenna systems," *AEÜ International Journal of Electronics and Communications*, vol-69, pp. 873 - 877, 2015.

2. R. Jana and R. Bhattacharjee, "A Novel Matched Feed Structure for Achieving Wide Cross-polar Bandwidth for an Offset Parabolic Reflector Antenna System," *IEEE Antenna and Wireless Propagation Letters*, vol-14, pp. 1590-1593, 2015.

Conference Publications:

1. R. Jana and R. Bhattacharjee, "Analysis of waveguide junctions using mode matching technique," *in IEEE Applied Electromagnetics Conference (AEMC)*, pp.1-4, 18-22 Dec., 2011.

2. R. Jana and R. Bhattacharjee, "Analysis of horn antennas including the horn transition into half space employing a full wave hybrid technique," *in IET International Radar Conference*, pp.1-4, 14-16 April, 2013.

3. R. Jana and R. Bhattacharjee, "Analysis of Scattering Parameters of a Stepped Cylindrical Horn containing inner Posts using MM and 2-D FEM," *in Twentieth National Conference communications (NCC)*, pp.1-6, Feb. 28-March 2, 2014.

4. R. Jana and R. Bhattacharjee, "A Tri-mode Low Cross-polarized Circular Matched Feed for Offset Reflector Antenna System," *in Twenty First National Conference communications (NCC)*, pp.1-6, Feb. 27-March 1, 2015.

5. R. Jana and R. Bhattacharjee, "A Hybrid Numerical Technique to Investigate the Performances of Offset Reflector and Matched Feed," *in IEEE Applied Electromagnetics Conference (AEMC)*, 18-21 Dec., 2015.

Manuscript Under Preparations:

1. R. Jana and R. Bhattacharjee, "Design of a novel dual-mode diagonal matched feed to achieve wide cross-polar bandwidth for an offset reflector antenna," *under preparation.*

2. R. Jana and R. Bhattacharjee, " Wide-band matched feed design employing conjugate field radiated from a square choke excited by two slots on a diagonal waveguide," *under preparation.*

3. R. Jana and R. Bhattacharjee, " A Matched feed design using the combined of 2-D full wave hybrid numerical technique and a hybrid probabilistic optimization technique," *under preparation.*

1

Offset Parabolic Antenna system: a brief introduction

Contents

This chapter presents the introduction and basic theory of an offset reflector antenna. The motivation of the work and summary of the contributions of the thesis are reported in this chapter. A flow chart is also presented which highlights the individual chapter's work.

1.1 Introduction

Offset reflector antennas offer features such as reduced aperture blockage, low side lobe levels, and isolation between feed and reflector as compared to their axisymmetric counterpart. Such features have been made use of in various applications like satellite communication, telemetry, remote sensing and mono-pulse tracking radar, etc [1]. In spite of these advantages, such reflector antennas often have limitations in exploiting the benefit of frequency reuse and effect the accuracy of the signal tracking by exhibiting high cross-polarization level when illuminated with linearly polarized feed. On the other hand, it also suffers from beam squinting when illuminated by a circularly polarized feed. Several remedial measures to reduce the depolarization effect of such antenna which have been reported in literature are as follows:

- Maintaining large focal-length-to-diameter ratio (F/D) and small tilt angle (α) helps in solving such problem [2]. However, large F/D results in a bulky and heavy structure.
- Use of the polarization selective grid has been proposed for offset reflector, so that it discriminates the cross-polar level in the secondary pattern [3]. Such solution may add complexity and increase system cost.
- Use of conventional dielectric lens in front of the horn is a way of reducing cross-polar power of an offset reflector antenna [4]. However, presence of dielectric increases the noise temperature as well as reduces the system gain.
- Rudge and Adatia proposed the conjugate matching technique which combines appropriate amount of desired higher order modes with dominant mode to reduce the cross-polar power of secondary pattern [1]. This technique is widely used nowadays for the design of feed as a multi-mode horn or antenna array. Such feeds are called matched feed.

With the increase in number of satellites on orbits, reducing the possibility of interference with other satellites is becoming increasingly important now a days. To minimize this interference, the

amount of side lobe and cross-polarization energy should be as low as possible in the principal plane of transmitting and receiving antenna; and a narrow main beam is also preferable for satellite communication. Taking those considerations into account, offset parabolic reflector antennas are often preferred over other narrow beam antennas, such as center feed parabolic antenna which suffers due to aperture blockage, dual reflector system which has drawback of noise temperature and low efficiency, and antenna array which has narrow bandwidth and high power loss etc [1]. Offset parabolic reflector antenna, which is a variant of parabolic reflector antenna, is extensively used in satellite communication systems like remote sensing, telemetric and TV broadcasting.

Design of compact offset reflector antenna system requires low values of F/D (F: focal length, D: diameter of the offset paraboloid antenna). Further, small F/D reduces the side lobe energy and creates very narrow pencil beam [1]. However, it increases cross polarization for a linear polarized feed. As mentioned earlier, literature provides the conjugate matching techniques to suppress the cross polar power with the use of multi-mode horns [1,5,6]. Also, it is mentioned in [1] that the performance of offset parabolic reflector antennas is strongly dependent on the feed characteristics. Although the concept of matched feed is known to the research community for a long time, it may be mentioned that the design methodologies of such feeds have not been dealt comprehensively in literature. The design of such feeds is quite involved and simulation of the entire system using CAD-tool is often very time-consuming. Matched feed design for offset reflector is still an active area of research as apparent from recent publications in this field. A tri-mode ($TE^1_{11}, TM^1_{11}, TE^1_{21}$) circular matched feed [7] has been used to feed the gravitationally balanced back-to-back reflector antenna, a rectangular matched feed has been proposed for mono-pulse radar using TE_{01} and TE_{11} modes [6], and a corrugated circular matched feed using HE^1_{11} and HE^1_{21} hybrid modes have also been developed [8]. A simplified analytical study on the dual-mode circular matched feed using TE^1_{11} and TE^1_{21} modes has been presented in [9] and a ring choke excited compact dual-mode circular waveguide feed using similar type of modes has also been proposed in [10]. A novel dual-mode dual-polarized circular waveguide feed excited by concentrically shorted ring patch is presented in [11]. A new kind of feed having symmetrical cascaded discontinuities which are created using intersection of three off-centered junctions of circular waveguide placed symmetrically with angular spacing of 120^0 operated with TE^1_{11} and TE^1_{21} modes, is proposed in circular waveguide for broadband operation of conjugate matched feed [12]. Several other literature related to conjugated matching are also available [13–15]. Such recent works motivates us

to investigate the various aspects of the design of multi-mode matched feed.

There has been considerable development in solving the electromagnetic (EM) problems using numerical techniques such as finite-element method (FEM), method of moment (MoM), finite difference time domain method (FDTD) etc. Such techniques can be applied along with geometric optics (GO), physical optics (PO), geometric theory of diffraction (GTD) and physical theory of diffraction (PTD) for calculation of radiated fields. However, solving practical problem using such techniques are quite involved. Instead of using a single techniques, combination of techniques are preferable. A combination of these techniques can be applied keeping in view the accuracy of solution, requirement of computation resources and time. Therefor, objective of this research is also to develop hybrid techniques for analysis and design of multi-mode feed horn structures and investigate the performance of the complete system including the offset reflector. Literature which have mostly inspired or motivated us to develop the hybrid technique to analysis the entire system of offset reflector antenna, are mentioned in [16–19].

1.2 Basic Theory and Literature Survey

The use of the reflectors started even before the 2$^{\text{nd}}$ world war in the fields of defense and space communication. World's largest radio telescope; Green Banks uses an offset reflector [20] having diameter 100-m. The basic theory on feed and reflector system are found in some classic text books [21–26]. Mainly, an offset reflector system is composed of three parts; reflector, feed and supporting stand for feed. The supporting-stand and feed do not make any blockage for the main lobe which is highly preferable for such type of systems. Conventionally, horn is considered as a primary feed due to its ability to control the reflector radiated field by the suitable excitation of feed pattern.

The schematic and focal plane aperture of an offset parabolic reflector is illustrated in Figure 1.1. In practical application, different kind of aperture shapes like elliptical, circular, rectangular etc are used. Offset parabolic reflector having circular aperture is most widely used in practical application and has been considered for this thesis. The detail of configurations of offset reflector system including its all relevant axies are shown in Figure 1.1. Here, $\{x_A,\ y_A,\ z_A\}$, $\{x_F,\ y_F,\ z_F\}$ and $\{x_R,\ y_R,\ z_R\}$ are the coordinate of the reflector, the feed and the reflector radiation field, respectively. F, D and H are the dimensions of reflector viz. focal length, diameter and offset height. The other parameters used to model of such system are tilt angle (α) of feed and half illuminated angle (θ_F). These can be

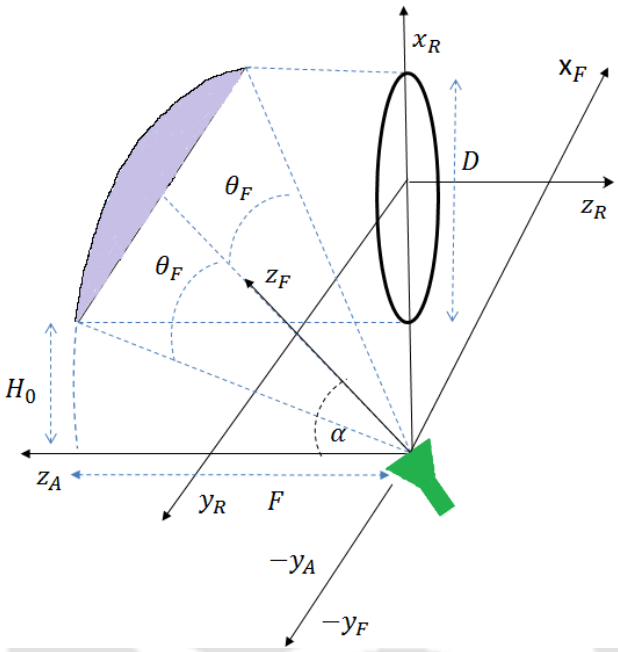

Figure 1.1: Offset reflector illuminated with feed.

represented as:

$$\theta_F = \tan^{-1}\frac{D+H}{2F} - \tan^{-1}\frac{H}{2F} \tag{1.1}$$

$$\alpha = \tan^{-1}\frac{D+H}{2F} + \tan^{-1}\frac{H}{2F} \tag{1.2}$$

As mentioned earlier, offset reflector is most preferable in practical applications for having features such as reduced aperture blockage, high antenna efficiency, low side lobe levels, and isolation between feed and reflector as compared to other narrow beam antennas. On the other hand, literature provides the evidence on the basis of measurement as well as based on the analytical study that offset reflector has a strong depolarization effect on the main lobe [1, 27]. Due to such depolarization effect, cross polarization appears in the main lobe when reflector is illuminated with linear polarized feed and on the other hand beam squinting occurs when the reflector is excited with circular polarized feed. As mentioned in Section 1.1, such depolarization effect degrades the system performance and such effects are more pronounced when F/D ratio is small. To remove the depolarization effect, several techniques [1–4,28] have been proposed in literature as specified in earlier Section. Based on literature survey, focal plane matching technique is found to be one of the most attractive solution to eliminate the cross-polar power of offset reflector antenna. It may be noted that the linear polarized matched feed

has wide applicability in the development of the frequency reuse systems. For such systems, achieving cross polar power level 30 dB below the reference power (co-polar power) is generally considered acceptable.

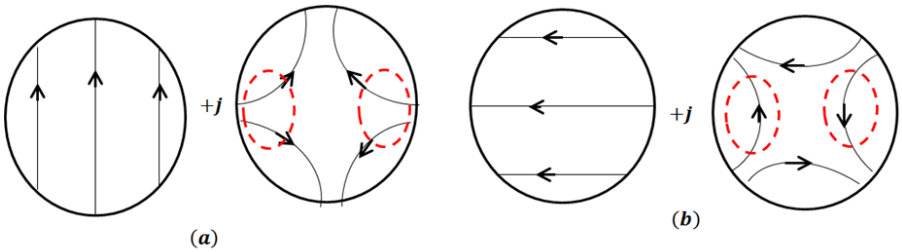

Figure 1.2: (a) focal plane field for x-polarized feed; (b) focal plane field for y-polarized feed.

Focal plane fields of an offset reflector are illustrated in Figure 1.2 for the excitation of linear x and y polarized feed, respectively. It can be observed that an unwanted field of complex value appears along with the desired field. The basic principle of the focal plane matching technique, is used to suppress such unwanted power, which satisfies the criteria that the tangential electric fields at feed's aperture are complex conjugate of the focal plane fields of the offset reflector antenna (as specified for linear polarized feed in Figure 1.2). Also, it is found in literature [1, 29] that multi-mode horn and antenna array have the ability to meet such criteria. Rudge and Adatia in [1] have shown the use of appropriate higher order mode(s) along with fundamental mode to compensate the cross-polar power. Also, several combination of modes are proposed for the matched feed design which are enlisted in Table 1.1.

Table 1.1: Waveguide modes for multi-mode matching

Feed structure	plane of symmetry (x)	plane of asymmetry (y)
Smooth-walled cylinder	$TE^1_{11} + TM^1_{11} + TE^1_{21}$	$TE^2_{11} + TM^2_{11} + TE^2_{21}$
Corrugated cylinder	$HE^1_{11} + HE^1_{21}$	$HE^2_{11} + HE^2_{21}$
Smooth-walled rectangular	$TE_{01} + TE_{11}/TM_{11}$	$TE_{10} + TE_{20}$

As we know, generating the conjugate mode inside the horn using the junction(s) always affects the return loss. On the other hand, maintaining the conjugate phase of higher order mode(s) for wide band at the feed aperture is a quite difficult task because main operating mode and the conjugate mode always propagate with different propagation constants. Current trend in matched feed design is to achieve the wide-band conjugate matching and maintaining the return loss within the operating band, which is very challenging. Several matched feed structures are recently reported in literature [6–12]

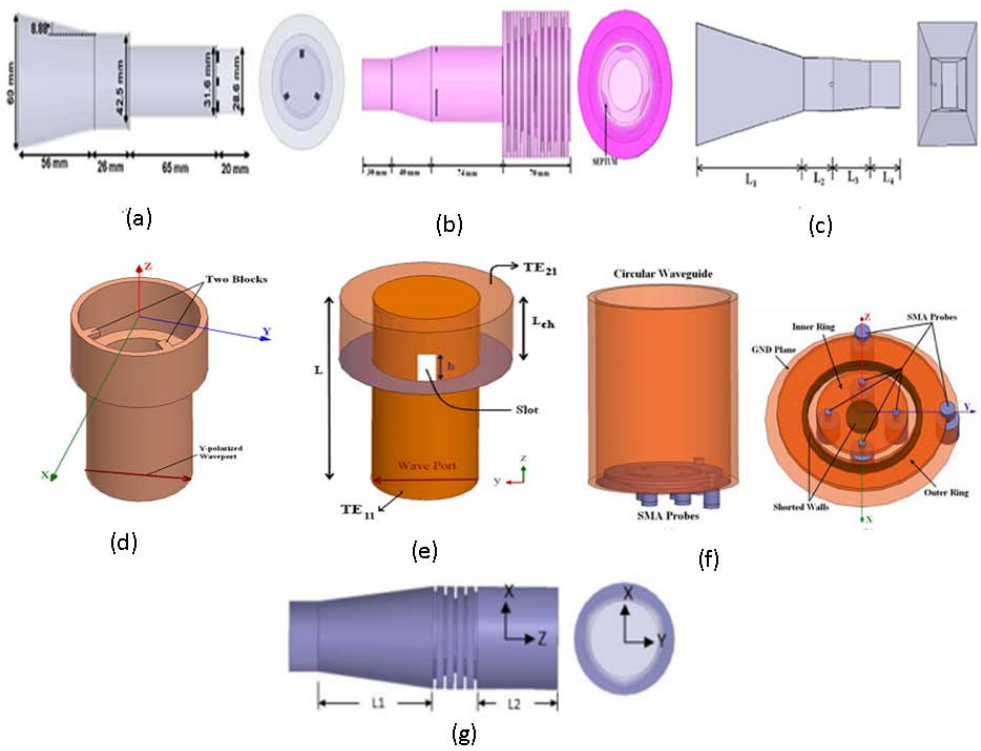

Figure 1.3: Matched feed configurations: (a) using $TE^1_{11} + TM^1_{11} + TE^1_{21}$ published in 2009 [6]; (b) operated with $HE^1_{11} + HE^1_{21}$ published in 2009 [7]; (c) employing $TE_{01} + TE_{11}$ appeared in 2009 [8] ; (d) using $TE^1_{11} + TE^1_{21}$ published in 2011 [9]; (e) operated with $TE^1_{11} + TE^1_{21}$ published in 2012 [10]; (f) employing $TE^1_{11} + TE^1_{21}/TE^2_{11} + TE^2_{21}$ appeared in 2013 [11]; (g) using $TE^1_{11} + TE^1_{21}$ published in 2015 [12];

based on the operating modes as specified in Table 1.1. Such motivating works are already introduced in Section 1.1. Most attractive and some good performing matched feed configurations reported in literature are shown in Figure 1.3.

Design of matched feeds using the available CAD tools is a challenging task. Basically, CAD tools are built based on any low frequency methods like FEM, MOM, FIT and FDTD employ volume or surface meshing. Generally, two kind of simulation models are used to analyze the feed and reflector model as (a) feed is kept within same radiation boundary to obtain the reflector pattern and (b) feed and reflector patterns are solved separately where evaluated far-field pattern of feed is used as a source for reflector. Usually, the reflector is at least several wavelengths in diameter. The number of meshes needed to solve scattering from such structures becomes huge and it demands very large amount of computing resources and time. Some recent CAD tools address this issue by providing a hybrid platform for computation. Generally, reflector pattern is calculated using PO while the reflector is illuminated by the feed pattern computed using the basic method used in a particular CAD tool.

With PO, main lobe pattern can be computed quite accurately, although the predictions of the far side lobe pattern is not accurate [8]. Keeping in view the facts mentioned, in this thesis, PO has been used to compute the reflector pattern and a 2-D field solver is developed to keep the computation requirements reasonable. On the other side, to analyze the feed, authors are motivated to develop the feed model using 2-D solver for overall efficient analysis. A hybrid technique which is a combination of MM/2D-FEM/MOM, is decided based on the literature [16–19] to analyze the feed.

1.3 Objectives

From the discussions presented in the earlier section, it can be seen that a feed antenna has a critical role in determining the overall performance of the offset parabolic antenna system. Moreover, performance evaluation of the complete system involving the offset reflector and the feed is quite involved. The objective of the thesis work is to investigate and propose new matched feed structures and implement the hybrid technique to investigate the entire system of offset reflector antenna. In order to meet the thesis objective, following majors tasks are to be carried out:

- Pattern calculation in case of an offset parabolic reflector for a given feed excitation.
- Development of an efficient hybrid numerical computing technique to analyze the feed antenna.
- Design of matched feed for a given specification of parabolic reflector.
- Development of analytical/numerical technique for synthesizing the feed and reflector.

1.4 Thesis Contribution

Various factors which influence the cross-polar performance of a conjugately matched feed have been investigated in detail.

Novel matched feed configurations have been proposed for obtaining wideband cross polar performance. Rectangular matched feed employing TE_{01} and TM_{11} modes have been designed and its cross polar performance has been investigated. Circular matched feed structure involving TE_{11}^1, TM_{11}^1 and TE_{21}^1 modes has been developed. Matched feed design involving non-regular geometries and waveguide modes have also been introduced. A diagonal matched feed has been investigated for the application

of horizontal-polarization. A rectangle choke excited by two slots on a diagonal waveguide has been proposed for the wide-band application.

Hybrid methods along with numerical codes have also been developed to investigate the performance of the proposed horn geometries. The proposed methods are reasonably accurate with comparatively lower computation complexity. For the adopted hybrid technique, the major steps are outlined in Flow chart 1 and the following major issues have been addressed appropriately in this thesis:

(a) Formulation of closed form expressions of reaction matrix for waveguide junctions for application of mode matching technique.

(b) Investigation of discontinuities using combination of MM and 2D-FEM techniques.

(c) Use of Kirchhoff-Huygen's principle to solve problems related to horn aperture in a finite ground plane and computation of field quantities employing RWG functions and 2D MOM.

(d) Development of PO technique for evaluation of reflector pattern.

1.5 Thesis Organization

The rest of this thesis is organized as follows:

Chapter 2: Interior Field Analysis using MM Technique

In this chapter, analysis of scattering parameters of regular shape horn (like rectangular and circular) using mode matching (MM) technique is reported. In case of tapered junction of regular horn structure, the closed-form expression of reaction matrix which aids in efficient implementation of the codes for junction analysis is formulated. Also, the convergence issue of MM technique is discussed. In addition, the theory of generalize scattering parameter (GSP) is presented in this chapter. To evaluate the performance of this technique, several horn structures having smooth, stepped and corrugated walls are studied and for such horn structures, results computed using our developed code in MATLAB are compared with simulated results of HFSS.

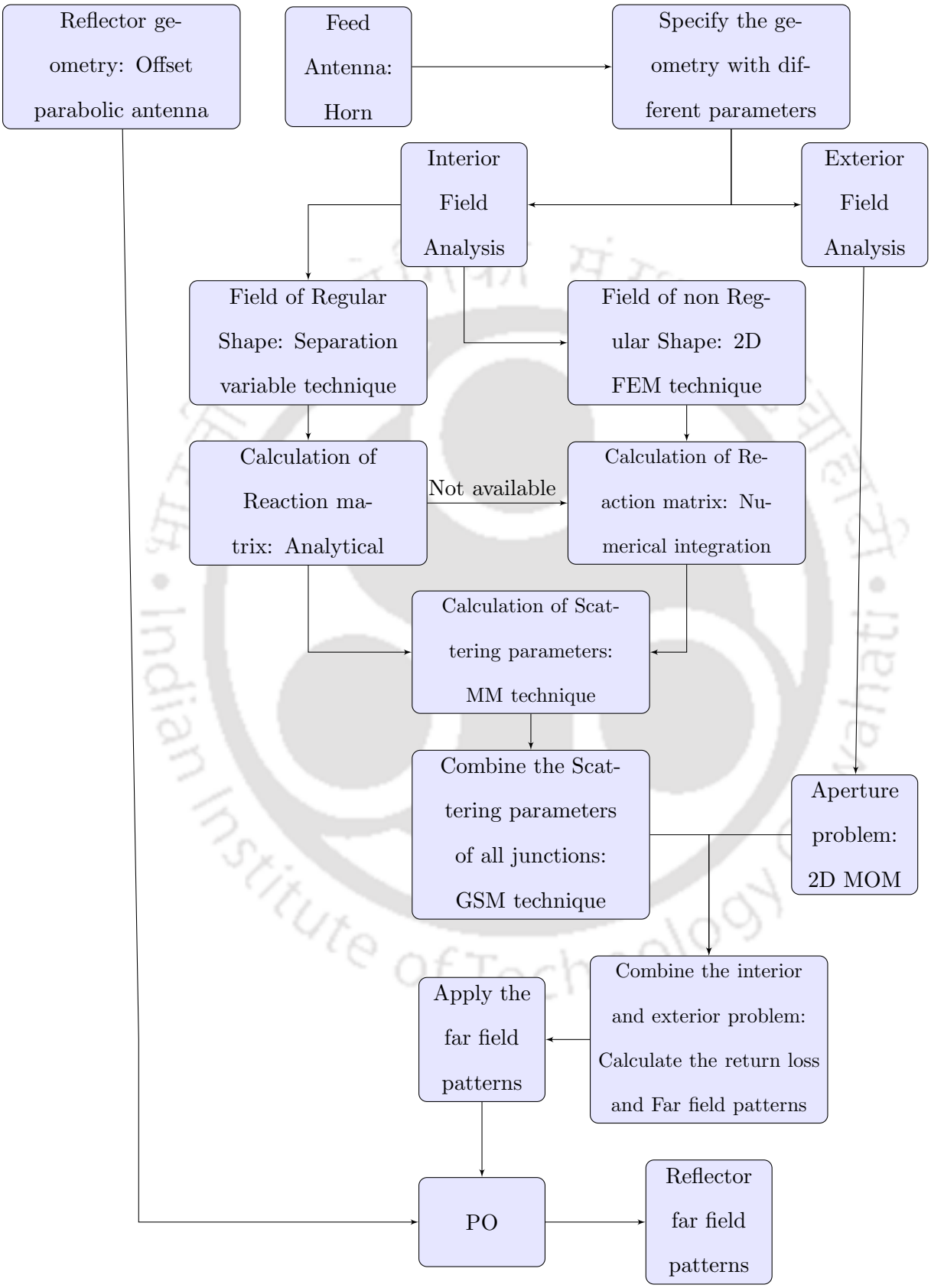

Flow chart 1**:** Integrated environment to analyze the matched feed and offset reflector antenna.

Chapter 3: A Hybrid MM/FE Technique to Analyze Horn having Discontinuities

This chapter presents the solution of Helmholtz equation using 2-D finite element method (FEM) to calculate the fields and their cutoff wave-numbers for non-regular surfaces. Delaunay triangulations are used to develop the FEM solution. The related theory for accurate prediction of eigenvalue and eigenvector for the solution of Helmholtz equation is discussed. The issues related to the calculation of reaction matrix for non-regular junction employing MM technique are elaborately discussed. The performance of this hybrid technique which is a combination of MM and 2-D FEM is evaluated in case of stepped cylindrical horn containing inner posts.

Chapter 4: Analysis of Open Ended Waveguide using MoM Technique

This chapter discusses the theory based on which the aperture problem related to multi-mode horn is modeled using the method of moment (MOM). The Rao-Willton-Gillson function (RWG) and Delaunay triangulations are used for 2D MOM solution to model for cases of horn having aperture on finite and infinite ground plane. Kirchhoff-Huygen's principle has been applied to model the horn aperture on a finite ground plane. The singular problem of the solution of scattering electric and magnetic field equation (EFIE, MFIE) is also described in this modeling. The performance of several horn structures are investigated using those techniques and the results are also compared with the simulated results obtained using HFSS-15. The theory behind the calculation of approximate far field pattern of multi-mode feed using Chu's model (analytical model) is also elaborately explained.

Chapter 5: An Analytical/Semi-analytical and Proposed Hybrid Technique for Reflector-Feed model

In this chapter, the far field pattern calculation of an offset reflector antenna using physical optics (PO) is reported. A brief discussion on particle swarm optimization technique (PSO) is presented as PSO has been used as a tool for optimization. Matched feed design using this optimization technique along with analytical or semi-analytical model of feed and reflector is also presented. For the rest of this chapter, the performance of our proposed hybrid technique comprising of MM, FEM, MoM and PO is evaluated for a proposed new kind of circular matched feed structure. The matched feed design involves TE_{11}^1, TM_{11}^1 and TE_{21}^1 modes as the operating modes.

Chapter 6: Design of Novel Matched Feed Structures

In this chapter, several matched feed structures are designed using PSO optimization technique along with analytical or semi-analytical model of feed and reflector. The first design is a rectangular matched feed based on TE_{01} and TM_{11} operating modes. In the next design, a non-regular type of matched feed structure for wide-band application is presented in this chapter. This is followed by a wide-band diagonal matched feed which is introduced to suppress the cross-polar power of the asymmetric-plane of an offset reflector antenna. A feed structure utilizing the conjugate field radiated from a rectangular choke excited by two slots on a diagonal horn to suppress the wide-band cross-polar power of an offset reflector antenna is also proposed. Design techniques for all the horn structures are explained in details.

Chapter 7: Summary and Future Work

In this chapter, the summary of the works is presented and conclusions are drawn. Possible directions of extending some of these works are also discussed in the chapter.

1.6 Conclusion

This chapter presents a brief introduction about the offset reflectors and associated feed structures. After discussing some relevant literature and thesis objectives, the problem statements have been presented. The overall thesis contribution has been discussed next. The chapter ends by presenting thesis organization and summary of all the subsequent chapters of the thesis.

2

Interior Field Analysis using MM Technique

Contents

In this chapter, analysis of scattering parameters of regular shape horn (like rectangular and circular) using mode matching (MM) technique is reported. In case of tapered junction of regular horn structure, the closed-form expression of reaction matrix which aids in efficient implementation of the codes for junction analysis is formulated. Also, the convergence issue of MM technique is discussed. In addition, the theory of generalize scattering parameter (GSP) is presented in this chapter. To evaluate the performance of this technique, several horn structures having smooth, stepped and corrugated walls are studied and for such horn structures, results computed using our developed code in MATLAB are compared with simulated results of HFSS.

2.1 Waveguide junction and modal solution

Waveguide junctions are used to generate the multiple modes. A multi-mode horn can minimize the cross polarization power for the direct radiation or when used as a feed for reflector antenna in satellite and radar communication systems. In order to generate the higher order modes inside the waveguide, the following methods are generally used: step discontinuity, smooth walled taper or transition, iris, corrugation, septum and bending of waveguide. There are several numerical techniques available to analyze the interior field of waveguide junction. Techniques such as finite difference time domain (FDTD), finite element method (FEM) and method of moment (MoM) [30] offer high flexibility but, often the computation complexity of such algorithms are high. Fast algorithm like the mode-matching (MM) method is an efficient alternative [31]. In analyzing the performance of a horn, a hybrid scheme may also be used, such as the use of mode matching technique for interior field of horn and the method of moment for open ended waveguide problem [32,33]. A good review on mode matching technique can be found in the references [34–38]. In this section, the theory related to the field solution of waveguide is briefly discussed.

It is well known that Maxwell's equations in source free region are defined as:

$$\nabla \times \vec{E} = -j\omega\mu\vec{H} \tag{2.1}$$

$$\nabla \times \vec{H} = j\omega\varepsilon\vec{E} \tag{2.2}$$

$$\nabla \cdot \vec{E} = 0 \tag{2.3}$$

$$\nabla \cdot \vec{H} = 0 \tag{2.4}$$

Using the equations (2.1), (2.2), (2.3) and (2.4), Helmholtz equation or wave equation can be easily constructed as $\nabla^2\vec{H} + k^2\vec{H} = 0$ and $\nabla^2\vec{E} + k^2\vec{E} = 0$ for TE and TM modes which has a general form of wave equation as $\nabla^2\Psi + k^2\Psi = 0$. Using the method of separation, Ψ can be written as $\Psi = \Psi_t(x,y)\Psi(z)$ in rectangular coordinate and $\Psi = \Psi_t(\rho,\phi)\Psi(z)$ in cylindrical coordinate. In the solution of this equation, $\Psi(z) = A^+e^{-\gamma z} + A^-e^{+\gamma z}$, A^+ represents the forward, A^- presents the backward coefficient and γ is wave propagation constant. The normalized scalar potential can be easily constructed for rectangular waveguide using the separation variables technique employed with Dirichlet and Neumann boundary conditions as found in [39] and the solutions are given as:

$$\text{TE mode:} \quad \Psi_t^{e_{mn}}(x,y) = \frac{2}{\pi}\sqrt{\frac{ab}{(1+\delta_{0m})(1+\delta_{0n})(mb)^2+(na)^2}}\cos(\frac{m\pi}{a}x)\cos(\frac{n\pi}{b}y) \tag{2.5}$$

$$\text{TM mode:} \quad \Psi_t^{h_{mn}}(x,y) = \frac{2}{\pi}\sqrt{\frac{ab}{(mb)^2+(na)^2}}\sin(\frac{m\pi}{a}x)\sin(\frac{n\pi}{b}y) \tag{2.6}$$

where $\delta_{0n} = \begin{cases} 0 & n \neq 0 \\ 1 & n = 0 \end{cases}$

Here, $a \times b$ presents the dimensions of rectangular waveguide and mn represents the mode numbers. Similarly, the normalized scalar potential of circular waveguide can be formulated as:

$$\text{TE mode:} \quad \Psi_t^{e_{np}}(\rho,\phi) = \sqrt{\frac{2}{\pi(1+\delta_{0n})(x'^2_{np}-n^2)}}\frac{J_n(\frac{x'_{np}\,\rho}{r})}{J_n(x'_{np})}\begin{cases}\sin(n\phi)\\ \cos(n\phi)\end{cases} \tag{2.7}$$

$$\text{TM mode:} \quad \Psi_t^{h_{np}}(\rho,\phi) = \sqrt{\frac{2}{\pi(1+\delta_{0n})}}\frac{J_n(\frac{x_{np}\,\rho}{r})}{J_{n+1}(x_{np})}\begin{cases}\sin(n\phi)\\ \cos(n\phi)\end{cases} \tag{2.8}$$

Here, x'_{np} represents the p^{th} root of the derivative of the bessel function (J_n) of the first kind ($J'_n(x'_{np}) = 0$) and r is radius of the circular waveguide. Similarly, x_{np} represents the p^{th} zero of the bessel function (J_n) of the first kind ($J_n(x_{np}) = 0$).

Different notations which are mostly used in subsequent sections/chapters of the thesis, are given in Table 2.1.

Table 2.1: Summary of TE and TM mode solution.

	TE mode	TM mode
Boundary (C) conditions	Neuman: $\frac{d\psi^e}{d\hat{n}} = 0$ on C	Dirichlet: $\psi^h = 0$ on C
Mode vectors	$\mathbf{e}^e = \hat{u}_z \times \nabla_t \psi^e$ $\mathbf{h}^e = -\nabla_t \psi^e$	$\mathbf{e}^h = -\nabla_t \psi^h$ $\mathbf{h}^h = -\hat{u}_z \times \nabla_t \psi^h$
General conversions	$\mathbf{e} = \mathbf{h} \times \hat{u}_z$ $\mathbf{h} = \hat{u}_z \times \mathbf{e}$	
Normalization	$\iint \mathbf{e}^2 ds = \iint \mathbf{h}^2 ds = -k_c^2 \iint \psi^2 ds$	
Propagation constant	$\gamma = \sqrt{k_c^2 - k^2}$	
Characteristic impedance	$Z_o^e = \frac{j\omega\mu}{\gamma}$	$Z_o^h = \frac{\gamma}{j\omega\epsilon}$
Transverse field	$\vec{E}_t = \sqrt{Z_o}\mathbf{e}(A^+ e^{-\gamma z} + A^- e^{\gamma z})$ $\vec{H}_t = \frac{1}{\sqrt{Z_o}}\mathbf{h}(A^+ e^{-\gamma z} - A^- e^{\gamma z})$	
Longitudinal field	$H_z^e = \frac{k_c^2}{k^2}\psi^e \frac{d\psi(z)}{dz}$	$E_z^h = \frac{k_c^2}{j\omega\epsilon}\psi^h \psi(z)$

2.2 Mode Matching Technique

MM technique is a very popular technique and its basic theory is well established in literature [34–38]. In this technique, the fields at the discontinuity region of the waveguide are expanded using suitable number of modes with unknown coefficients. Scattering parameters are computed using continuity of tangential electric and magnetic fields at the discontinuity and the application of the reaction theorem. The values of scattering parameters depend on the reaction matrix which represents the coupling of fields on the both sides as TE, TM and TEM waves. Hollow wave guide does not support the TEM mode. In this analysis, only TE and TM mode couplings are considered.

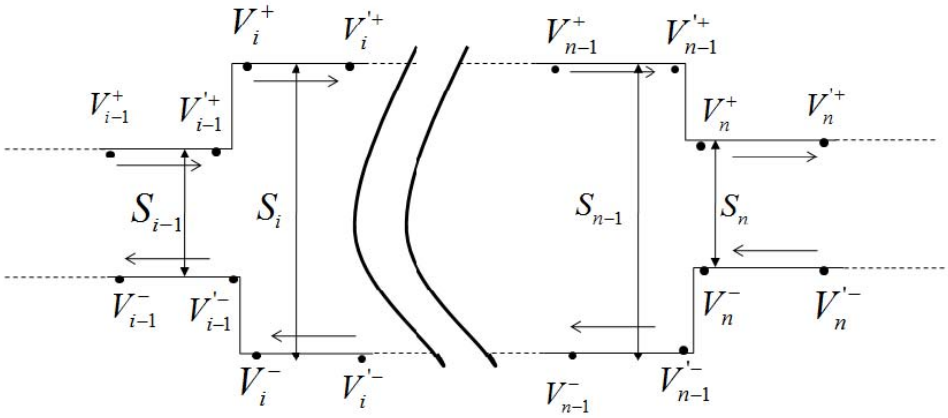

Figure 2.1: Step junction discontinuity: i^{th} number junction is step up and n^{th} junction is step down and S_{i-1}, S_i, S_{n-1} and S_n are the waveguide surfaces.

Discontinuity of waveguide surface can be represented as a step up or step down junction as shown

in Figure 2.1. Considering that i^{th} junction is located at $z = 0$, the fields to the left of junction ($z = 0^-$) are represented in matrix form as:

$$\vec{E}_{i-1} = [\mathbf{e}_{i-1}]_{1\times N}[Y_{i-1}]^{-1}_{N\times N}\left[V^{'+}_{i-1} + V^{'-}_{i-1}\right]_{N\times 1} \tag{2.9}$$

$$\vec{H}_{i-1} = [\mathbf{h}_{i-1}]_{1\times N}[Y_{i-1}]_{N\times N}\left[V^{'+}_{i-1} - V^{'-}_{i-1}\right]_{N\times 1} \tag{2.10}$$

where $[\bar{e}_{i-1}]$ and $\left[\bar{h}_{i-1}\right]$ are column vectors which contains N number of orthogonal, normalized electric and magnetic fields. $[Y_{i-1}] = \left[\frac{1}{\sqrt{Z^n_{0_{i-1}}}}\right]$ is a diagonal matrix, $Z^n_{0_{i-1}}$ is the n^{th} mode impedance, $V^{'+}_{i-1}$, $V^{'-}_{i-1}$ are row matrix containing forward and backward voltage equivalent coefficients of different modes.

Similarly, the fields to the right of junction ($z = 0^+$) are represented in matrix form as

$$\vec{E}_i = [\mathbf{e}_i]_{1\times M}[Y_i]^{-1}_{M\times M}\left[V^{+}_{i} + V^{-}_{i}\right]_{M\times 1} \tag{2.11}$$

$$\vec{H}_i = [\mathbf{h}_i]_{1\times M}[Y_i]_{M\times M}\left[V^{+}_{i} - V^{-}_{i}\right]_{M\times 1} \tag{2.12}$$

The boundary conditions at the junction are that the tangential electric and magnetic fields are continuous across the common aperture and tangential electric fields on PEC are zero.

$$\vec{E}_i = \begin{cases} \vec{E}_{i-1} & \text{on } S_{i-1} \\ 0 & \text{on } S_i - S_{i-1} \end{cases} \tag{2.13}$$

$$\vec{H}_i = \begin{cases} \vec{H}_{i-1} & \text{on } S_{i-1} \\ unknown & \text{on } S_i - S_{i-1} \end{cases} \tag{2.14}$$

Using the reaction theorem, from equation (2.13), we can write

$$\iint\limits_{S_{i-1}} \vec{E}_{i-1} \times \ \mathbf{h}^m_i \cdot d\vec{S} = \iint\limits_{S_i} \vec{E}_i \times \mathbf{h}^m_i \cdot d\vec{S} \tag{2.15}$$

In matrix form, equation (2.15) using the equations (2.9) and (2.11) can be written as:

$$[P]_{M\times N}[Y_{i-1}]^{-1}_{N\times N}\left[V^{'+}_{i-1} + V^{'-}_{i-1}\right]_{N\times 1} = [R]_{M\times M}[Y_i]^{-1}_{M\times M}\left[V^{+}_{i} + V^{-}_{i}\right]_{M\times 1} \tag{2.16}$$

where elements of reaction matrix are calculated as:

$$p_{nm} = \iint\limits_{S_{i-1}} \mathbf{e}_{i-1}^{n} \times \mathbf{h}_{i}^{m} \cdot d\vec{S}$$

$$R_{nm} = \iint\limits_{S_i} \mathbf{e}_{i}^{n} \times \mathbf{h}_{i}^{m} \cdot d\vec{S} = \begin{cases} 1 & n=m \\ 0 & n\neq m \end{cases}$$

Similarly, from the equation (2.14) and using the equations (2.10) and (2.12), we can write

$$\iint\limits_{S_{i-1}} \mathbf{e}_{i-1}^{n} \times \vec{H}_{i-1} \cdot d\vec{S} = \iint\limits_{S_{i-1}} \mathbf{e}_{i-1}^{n} \times \vec{H}_{i} \cdot d\vec{S}$$

$$[Q]_{N\times N}[Y_{i-1}]_{N\times N}\left[V_{i-1}^{\prime +} - V_{i-1}^{\prime -}\right]_{N\times 1} = [P]^{T}{}_{N\times M}[Y_i]_{M\times M}\left[V_i^{+} - V_i^{-}\right]_{M\times 1} \tag{2.17}$$

$$Q_{nm} = \iint\limits_{S_{i-1}} \mathbf{e}_{i-1}^{n} \times \mathbf{h}_{i-1}^{m} \cdot d\vec{S} = \begin{cases} 1 & n=m \\ 0 & n\neq m \end{cases}$$

Here, $[...]^T$ represents the transpose of a matrix. The expressions of the sub-matrices of scattering parameter are given below using the equations (2.16) and (2.17).

$$\begin{aligned}
\left[S_{11}^{i}\right]_{N\times N} &= \left[Y_{i-1} + Y_{L_{i-1}}\right]^{-1}\left[Y_{i-1} - Y_{L_{i-1}}\right] \\
\left[S_{12}^{i}\right]_{N\times M} &= 2\left[Y_{i-1} + Y_{L_{i-1}}\right]^{-1} P^{T} Y_i \\
\left[S_{21}^{i}\right]_{M\times N} &= 2\left[Y_{i}^{-1} + Y_{L_i}\right]^{-1} P Y_{i-1}^{-1} \\
\left[S_{22}^{i}\right]_{M\times M} &= \left[Y_{i}^{-1} + Y_{L_i}\right]^{-1}\left[Y_{L_i} - Y_{i}^{-1}\right]
\end{aligned}$$

where $\mathbf{Y}_{L_{i-1}} = \mathbf{P}^{T}\mathbf{Y}_{i}\mathbf{Y}_{i}\mathbf{P}\mathbf{Y}_{i-1}^{-1}$ and $\mathbf{Y}_{L_i} = \mathbf{P}\mathbf{Y}_{i-1}^{-1}\mathbf{Y}_{i-1}^{-1}\mathbf{P}^{T}\mathbf{Y}_{i}$.

The n^{th} junction is antisymmetric junction of the i^{th} junction, to evaluate the scattering parameter the junction is rotated by 180°. To calculate the $\mathbf{P}$ matrix with respect to S_n surface, the scattering parameter can be calculated in the similar way as done in the case of i^{th} junction.

2.3 Closed form expression of reaction matrix

As discussed earlier, the scattering parameters calculation using MM technique depends on the values of reaction matrix which represents coupling values between the fields at the both sides of the

junction. Closed form solution of reaction matrix can be formulated for junctions of regular shaped waveguides. Closed solutions are accurate and saves computation time.

The generalized closed-form expressions of the reaction matrix for circular symmetric step junction are formulated here as:

$$P^{ee} = \begin{cases} \frac{2\delta_{n_1n_2}\alpha_s^2\beta_b r_s J'_n(\beta_b r_s)}{\left(\alpha_s^2-\beta_b^2\right)J_n(\beta_b r_b)\sqrt{(\alpha_s^2 r_s^2-n^2)\left(\beta_b^2 r_b^2-n^2\right)}} \ldots\ldots\ldots [\alpha_s \neq \beta_b, \quad \mathrm{TE}_s^{x,y} \otimes \mathrm{TE}_b^{x,y}] \\ \delta_{n_1n_2}\sqrt{\frac{\alpha_s^2 r_s^2-n^2}{\beta_b^2 r_b^2-n^2}}\frac{J_n(\alpha_s r_s)}{J_n(\beta_b r_b)} \ldots\ldots\ldots\ldots\ldots\ldots [\alpha_s = \beta_b, \quad \mathrm{TE}_s^{x,y} \otimes \mathrm{TE}_b^{x,y}] \end{cases}$$

$$P^{hh} = \begin{cases} \delta_{n_1n_2}\frac{2\beta_b}{r_b\left(\alpha_a^2-\beta_b^2\right)}\frac{J_n(\beta_b r_s)}{J_{n+1}(\beta_b r_b)} \ldots\ldots\ldots\ldots\ldots\ldots [\alpha_a \neq \beta_b, \quad \mathrm{TM}_s^{x,y} \otimes \mathrm{TM}_b^{x,y}] \\ \delta_{n_1n_2}\frac{r_s}{r_b}\frac{J_{n+1}(\alpha_s r_s)}{J_{n+1}(\beta_b r_b)} \ldots\ldots\ldots\ldots\ldots\ldots\ldots\ldots [\alpha_s = \beta_b, \quad \mathrm{TM}_s^{x,y} \otimes \mathrm{TM}_b^{x,y}] \end{cases}$$

$$P^{eh} = \begin{cases} \delta_{n_1n_2}\frac{2n}{\beta_b r_b\sqrt{\alpha_s^2 r_s^2-n^2}}\frac{J_n(\beta_b r_s)}{J_{n+1}(\beta_b r_b)} \ldots\ldots\ldots\ldots\ldots\ldots\ldots [\mathrm{TE}_s^{x} \otimes \mathrm{TM}_b^{x}] \\ -\delta_{n_1n_2}\frac{2n}{\beta_b r_b\sqrt{\alpha_s^2 r_s^2-n^2}}\frac{J_n(\beta_b r_s)}{J_{n+1}(\beta_b r_b)} \ldots\ldots\ldots\ldots\ldots\ldots\ldots [\mathrm{TE}_s^{y} \otimes \mathrm{TM}_b^{y}] \end{cases}$$

$$P^{he} = 0$$

$$\text{where } \delta_{n_1n_2} = \begin{cases} 1 \ldots\ldots n_1 = n_2 = n \\ 0 \ldots\ldots\ldots\ldots n_1 \neq n_2 \end{cases}$$

r_s and α_s respectively represent the radius and cutoff wave number for the smaller waveguide while r_b and β_b represent the same for larger waveguide. (n_1m_1), (n_2m_2) represents the different modes at smaller and bigger surfaces. J_n, $\otimes$ stands for the first kind bessel function of n^{th} order and coupling between different modes, respectively. The reaction matrix coefficients P^{ee}, P^{eh} , P^{hh} and P^{he} represent the coupling between both side fields of TE (e) and TM (h) mode on both sides of the junction.

The calculation of **P** matrix for symmetric or asymmetric junction of rectangular waveguide is given below:

$$P^{ee}_{nm} = u(\tfrac{b}{c}m_1m_2(k_2y - k_1x)(t_2w + t_1z) + \tfrac{a}{d}n_1n_2(k_2y + k_1x)(t_2w - t_1z))$$

$$P^{eh}_{nm} = u(\tfrac{b}{d}m_1n_2(k_2y - k_1x)(t_2w + t_1z) - \tfrac{a}{c}m_2n_1(k_2y + k_1x)(t_2w - t_1z))$$

$$P^{eh}_{nm} = u(\tfrac{b}{c}m_1m_2(k_2y + k_1x)(t_2w - t_1z) - \tfrac{a}{d}n_1n_2(k_2y - k_1x)(t_2w + t_1z))$$

$$P^{he}_{nm} = 0$$

$$u = \sqrt{\frac{abcd}{(1+\delta_{0m_1})(1+\delta_{0n_1})(1+\delta_{0m_2})(1+\delta_{0n_2})(m_1^2b^2+n_1^2a^2)(m_2^2d^2+n_2^2c^2)}}$$

$$x = \mathrm{sinc}(\tfrac{cm_1+am_2}{2c})$$

$$y = \mathrm{sinc}(\tfrac{cm_1-am_2}{2c})$$

$$z = \mathrm{sinc}(\tfrac{dn_1+bn_2}{2d})$$

$$w = \mathrm{sinc}(\tfrac{dn_1-bn_2}{2d})$$

$k_1 = \cos((m_1 + m_2 + \frac{2z_x}{c})\frac{\pi}{2})$

$k_2 = \cos((m_1 - m_2 - \frac{2z_x}{c})\frac{\pi}{2})$

$t_1 = \cos((n_1 + n_2 + \frac{2z_y}{c})\frac{\pi}{2})$

$t_2 = \cos((n_1 - n_2 - \frac{2z_y}{c})\frac{\pi}{2})$

where $n,\ m$ represent the $(m_1 n_1)$ or $(m_2 n_2)$ rectangular modes and z_x, z_y are the offset center distance between two waveguides in X axis and Y axis and $a,\ b,\ c,\ d$ are dimensions of waveguide.

2.4 Formulation of GSP for cascaded junctions

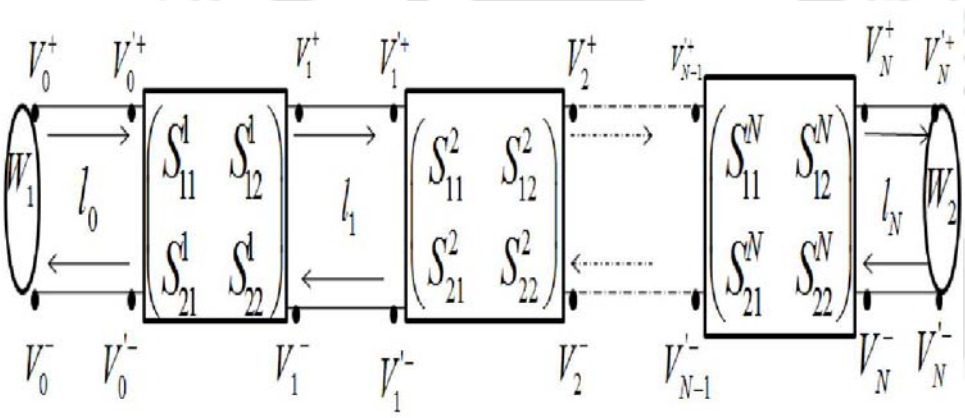

Figure 2.2: N number of junctions with forward wave in $'+'$ symbol, backward wave in $'-'$, W_1, W_2 are the wave port 1 and wave port 2.

Equivalent scattering matrix for the structure having N junctions as in Figure 2.2 is evaluated by successively combining the S-parameters of individual junctions. The details of such techniques are reported in this section. Figure 2.2 shows the $N+1$ number of transmission line segments and N number of junctions, where V_{k-1}^+, V_{k-1}^- are the forward and backward voltage coefficients and l_{k-1} is the length of the k^{th} transmission line. Scattering parameter can be written in equation (2.18) for i^{th} junction and the equations (2.19) and (2.20) represent the transmission line matrix for forward and backward voltage at the k^{th} transmission line. W_1 and W_2 are the wave ports which are ideal and assumed to be a perfect matching layer (PML) such that it will not reflect any wave.

$$\begin{pmatrix} V_{i-1}^{'-} \\ V_i^+ \end{pmatrix} = \begin{pmatrix} S_{11}^i & S_{12}^i \\ S_{21}^i & S_{22}^i \end{pmatrix} \begin{pmatrix} V_{i-1}^{'+} \\ V_i^- \end{pmatrix} \qquad i = 1, 2, ...N \tag{2.18}$$

$$\left(V_{k-1}^{'+}\right) = \left(S_{L_{k-1}}\right)\left(V_{k-1}^{+}\right) \qquad k = 1, 2, ...N+1 \tag{2.19}$$

$$\left(V_{k-1}^{-}\right) = \left(S_{L_{k-1}}\right)\left(V_{k-1}^{'-}\right) \tag{2.20}$$

where $\mathbf{S}_{L_{k-1}}$ is a diagonal matrix and its n^{th} diagonal element can be written as

$$S_{L_{k-1}}^{n} = \exp(-\gamma_{k-1}^{n} \mathrm{l}_{k-1}) \tag{2.21}$$

and the complex propagation constant γ_{k-1}^{n} for n^{th} mode can be written as

$$\gamma_{k-1}^{n} = \sqrt{(k_{c_{k-1}}^{n})^2 - k^2} = \sqrt{(k_{c_{k-1}}^{n})^2 - \omega^2 \mu_0 \varepsilon_0 \varepsilon_r (1 - j\tan\delta)}, \tag{2.22}$$

where $k_{c_{k-1}}^{n}$ is the cut off wave number of n^{th} mode and $\varepsilon_r(1-j\tan\delta)$ is the complex dielectric constant for dielectric material inside the wave guide.

Equivalent scattering matrix of this N number of junctions can be evaluated by successively combining the scattering matrices. Using the equations (2.18), (2.19), (2.20) and employing the formulas of inversion and multiplication of block matrix as given in Appendix 8.1. The equivalent scattering matrix for the combination of the first i^{th} junction can be easily constructed as given below:

$$\mathbf{S}_{11}^{\text{comb}_i} = \mathbf{S}_{11}^{\text{comb}_{i-1}} + \mathbf{S}_{12}^{\text{comb}_{i-1}} \mathbf{S}_{L_{i-1}} \mathbf{U}_1^i \mathbf{S}_{11}^i \mathbf{S}_{L_{i-1}} \mathbf{S}_{21}^{\text{comb}_{i-1}} \tag{2.23}$$

$$\mathbf{S}_{12}^{\text{comb}_i} = \mathbf{S}_{12}^{comb_{i-1}} \mathbf{S}_{L_{i-1}} \mathbf{U}_1^i \mathbf{S}_{12}^i \tag{2.24}$$

$$\mathbf{S}_{21}^{\text{comb}_i} = \mathbf{S}_{21}^i \mathbf{S}_{L_{i-1}} \mathbf{U}_2^i \mathbf{S}_{21}^{\text{comb}_{i-1}} \tag{2.25}$$

$$\mathbf{S}_{22}^{\text{comb}_i} = \mathbf{S}_{22}^i + \mathbf{S}_{21}^i \mathbf{S}_{L_{i-1}} \mathbf{U}_2^i \mathbf{S}_{22}^{\text{comb}_{i-1}} \mathbf{S}_{L_{i-1}} \mathbf{S}_{12}^i \tag{2.26}$$

where $\mathbf{U}_1^i = \left([I] - S_{11}^i S_{L_{i-1}} S_{22}^{\text{comb}_{i-1}} S_{L_{i-1}}\right)^{-1}$ and $\mathbf{U}_2^i = \left([I] - S_{22}^{\text{comb}_{i-1}} S_{L_{i-1}} S_{22}^i S_{L_{i-1}}\right)^{-1}$.

The N number of junctions can be combined using the equations (2.23), (2.24), (2.25) and (2.26) where the last step is to combine the effects for 1^{st} and $(N+1)^{th}$ transmission line. Finally, the resultant scattering parameter can be evaluated as:

$$\begin{pmatrix} S_{11} & S_{12} \\ S_{21} & S_{22} \end{pmatrix} = \begin{pmatrix} S_{L_0} S_{11}^{\text{comb}_N} S_{L_0} & S_{L_0} S_{12}^{\text{comb}_N} S_{L_N} \\ S_{L_N} S_{21}^{\text{comb}_N} S_{L_0} & S_{L_N} S_{22}^{\text{comb}_N} S_{L_N} \end{pmatrix}$$

2.5 Results

Two sets of codes have been implemented to study the scattering parameters of symmetric circular junctions and symmetric rectangular junctions and the performance of the codes have been verified with HFSS. Some of the comparisons are given as follows:

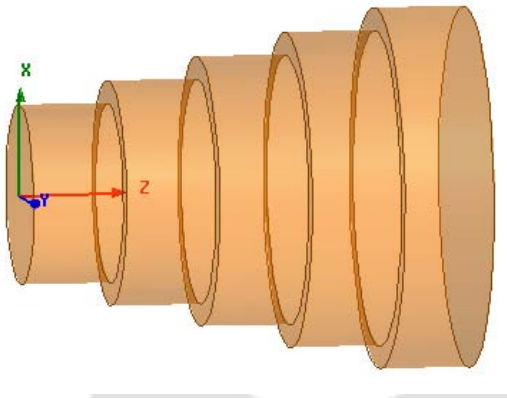

Figure 2.3: A stepped circular waveguide figure in HFSS.

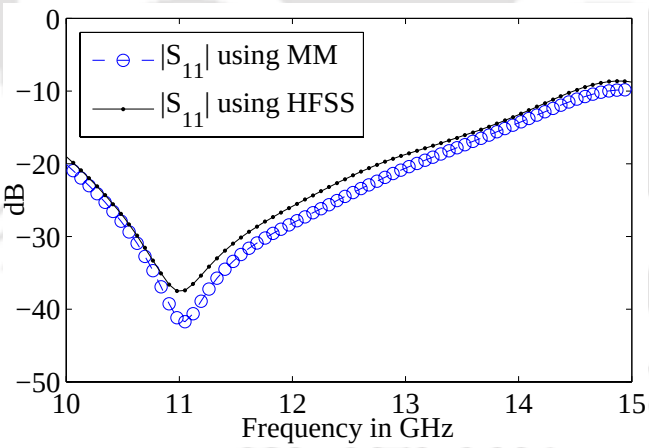

Figure 2.4: Scattering parameter of stepper junction for TE_{11} mode.

A four-stepped circular waveguide junction having radii of 10 mm, 12.5 mm, 15 mm, 17.5 mm, 20 mm and each step having a length of 10 mm, is shown in Figure 2.3. To verify the performance of the developed code, the computed results are compared with HFSS simulated results as given in Figure 2.4, 2.5.

The performance of a smooth-walled tapped circular waveguide as shown in Figure 2.6 having radii of 10 mm and 20 mm and length of 40 mm has been evaluated and the verified results are given in

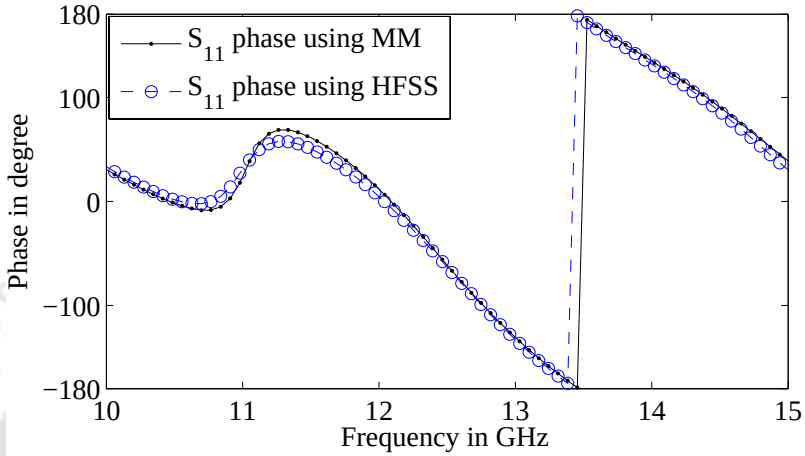

Figure 2.5: Stepped junction, phase of S_{11} for TE_{11} mode.

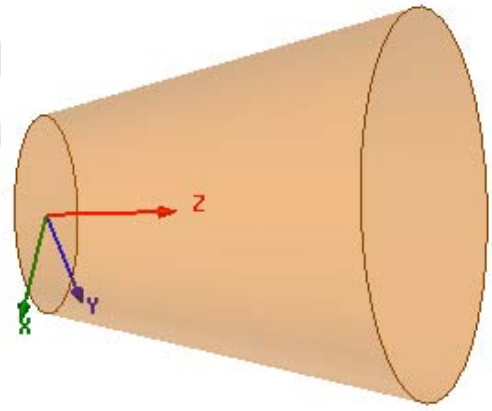

Figure 2.6: A smooth walled waveguide figure in HFSS.

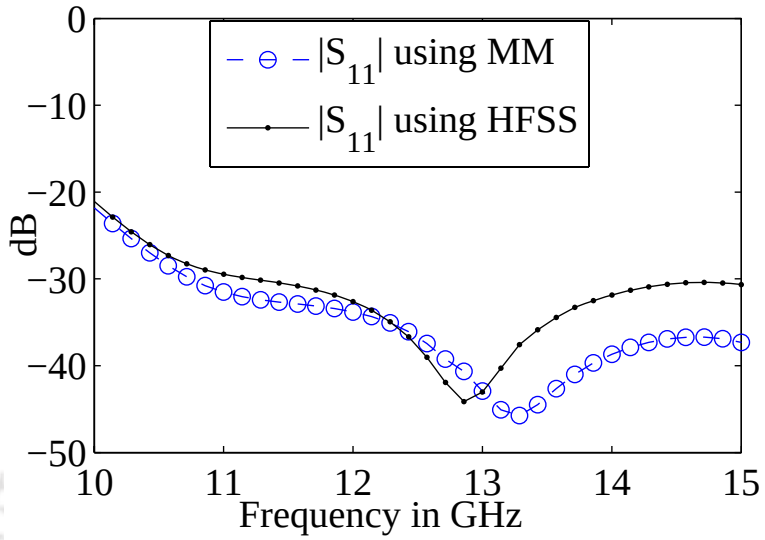

Figure 2.7: Scattering parameter of smooth walled waveguide for TE_{11} mode.

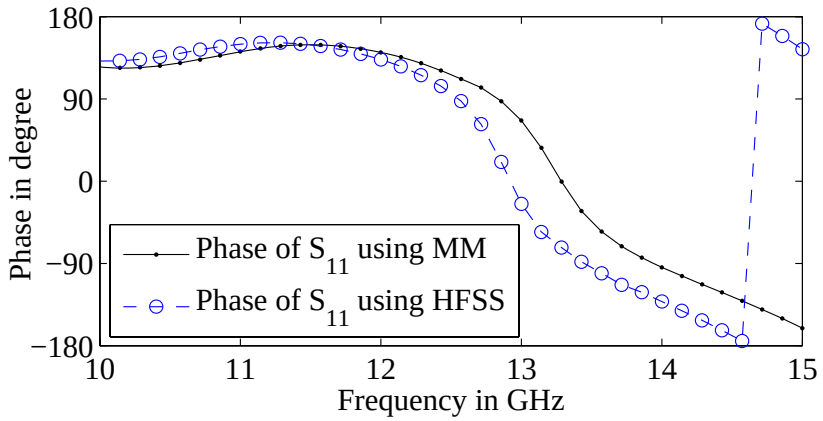

Figure 2.8: Smooth walled waveguide, phase of S_{11} for TE_{11} mode.

Figure 2.8 and 2.7.

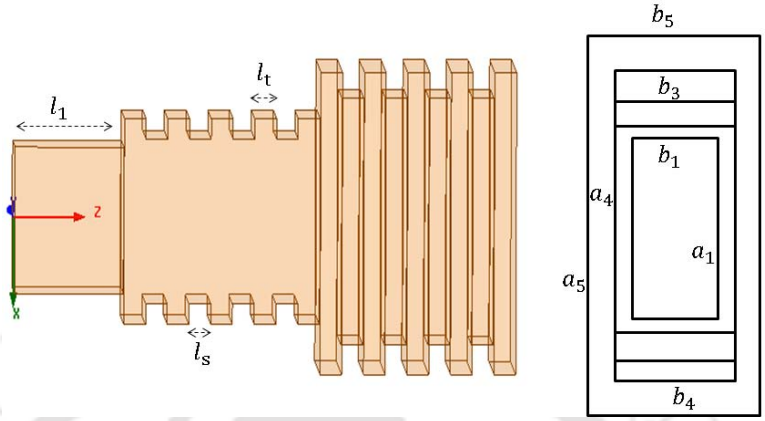

Figure 2.9: A corrugated rectangular waveguide filled with lossy dielectric in HFSS. Dimensions of our considered structure : $\{l_1,\ l_t,\ l_s,\ a_1,\ b_1,\ a_2,\ b_2,\ a_3,\ b_3,\ a_4,\ b_4,\ a_5,\ b_5\}$ = {10, 2, 2, 10.7, 5, 15, 7, 12, 7, 18, 7, 22, 10} mm.

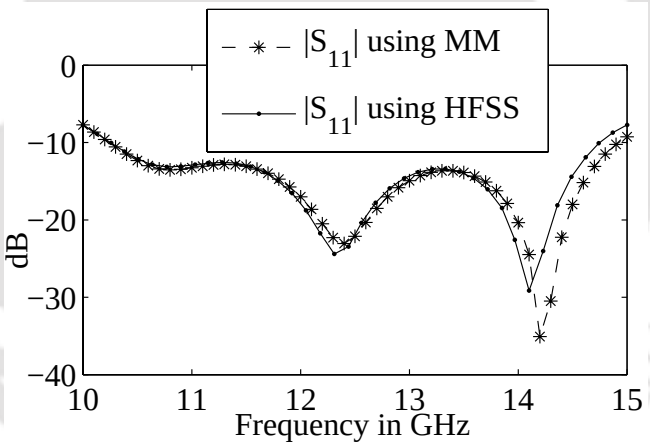

Figure 2.10: Scattering parameter S_{11} for TE_{10} mode.

The performance of a corrugated rectangular waveguide as shown in Figure 2.9 with lossy dielectric (relative dielectric constant= 2.1 and loss tangent= 0.002) has been evaluated using the formulated codes and results are given in Figure 2.10, 2.11, 2.12 and 2.13.

The choice of the number of modes, such as the unbalanced number of modes or equal number of modes for both sides of the junction, plays an important role for convergence in MM solution. However, the exact number of modes which leads to the convergence of the scattering parameters is generally not known. Our analysis deals with power in multiple modes at input and output. However, a single parameter can be used to describe the error performance if we compute RMS of $\mathbf{S}^t\mathbf{S}^* - \mathbf{I}/[0]$,

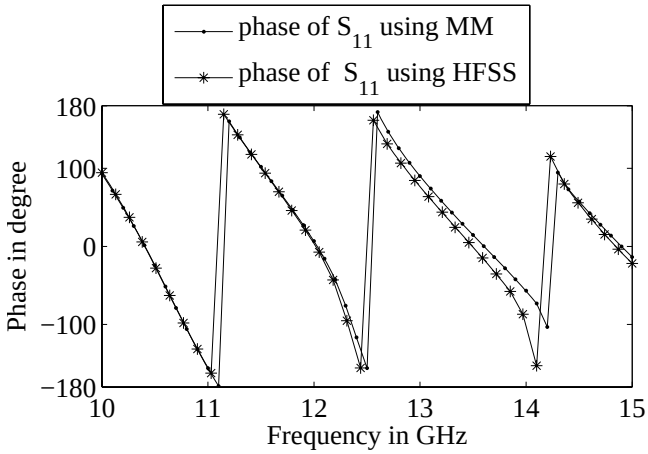

Figure 2.11: Phase of S_{11} for TE_{10} mode.

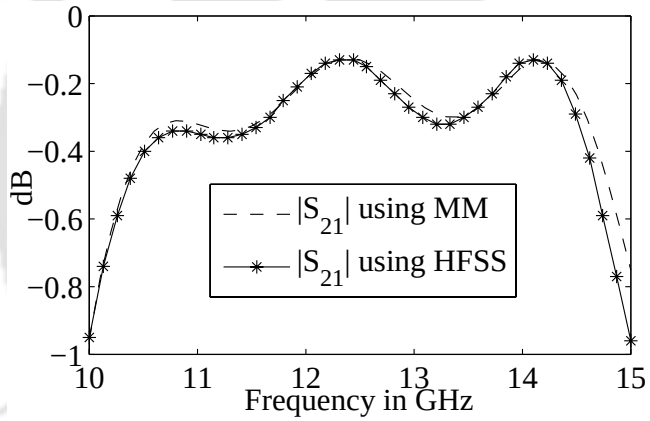

Figure 2.12: Scattering parameter S_{21} for TE_{10} mode.

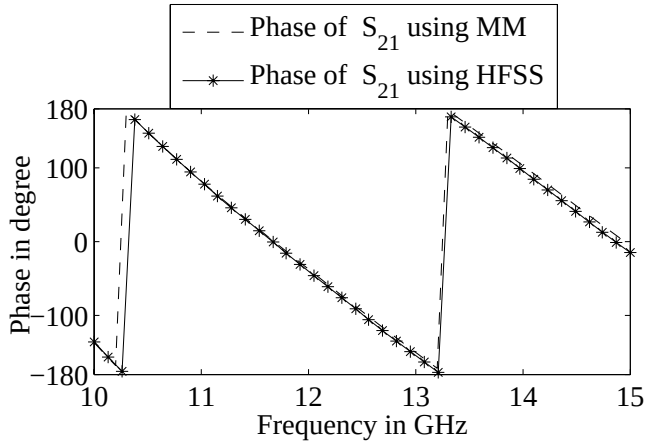

Figure 2.13: Phase of S_{21} for TE_{10} mode.

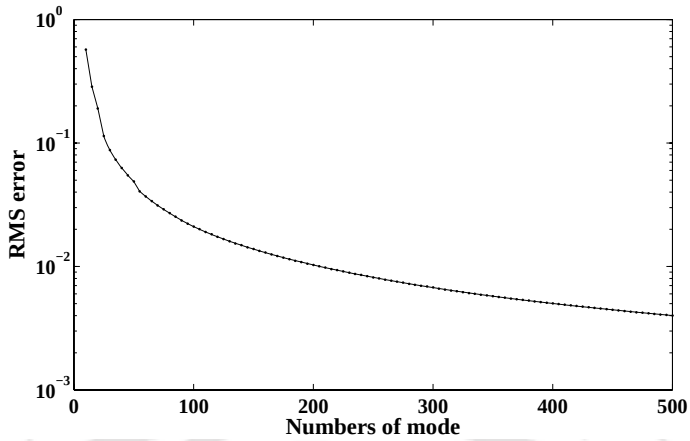

Figure 2.14: RMS error of MM technique with respect to choice of number of modes for single junction at 9 GHz.

where $\mathbf{S}$, t and $*$ are the scattering parameter, transpose and conjugate, respectively. It may be noted that in case of lossless junctions, for active modes $\mathbf{S}^t\mathbf{S}^* = \mathbf{I}$ ($\mathbf{I}$: unity matrix) and for inactive modes $\mathbf{S}^t\mathbf{S}^* = [0]$. In this context, we have evaluated the RMS error at 9 GHz of $\mathbf{S}^t\mathbf{S}^* - \mathbf{I}/[0]$ for a single junction of a circular waveguide having radii 18.5 mm and 23.5 mm and each having lengths 15 mm. The plot of RMS error with respect to number of modes is shown in Figure 2.14. It can be seen that the error reduces as the number of modes increases. However, beyond a certain number of modes, the increase in number of modes does not reduce the error any further.

2.6 Conclusion

In this chapter, we have presented some details of the mode-matching based technique for evaluating the performance of different types of waveguide junctions. For many practical designs, it is necessary to generate multiple waveguide modes and the waveguide junctions are often used for this purpose. Some closed form integration formulas for reaction matrix have been developed which help in implementing the codes for junction analysis in an efficient manner. Two set of codes have been implemented in MATLAB for analyzing different types of waveguide junctions. As can be seen from the results presented, close agreements are obtained with results computed for similar structures using HFSS. The choice of the number of modes, such as the unbalanced number of modes or equal number of modes for both sides of the junction, plays an important role for convergence in MM solution. However, the exact number of modes which leads to the convergence of the scattering parameters is

generally not known. In spite of the convergence problem, due to its low computational complexity, MM can be used as a tool for preliminary investigation of waveguide junctions.

3

A Hybrid MM/FE Technique to Analyze Horn having Discontinuities

Contents

This chapter presents the solution of Helmholtz equation using 2-D finite element method (FEM) to calculate the fields and their cutoff wave-numbers for non-regular surfaces. Delaunay triangulations are used to develop the FEM solution. The related theory for accurate prediction of eigenvalue and eigenvector for the solution of Helmholtz equation is discussed. The issues related to the calculation of reaction matrix for non-regular junction employing MM technique are elaborately discussed. The performance of this hybrid technique which is a combination of MM and 2-D FEM is evaluated in case of stepped cylindrical horn containing inner posts.

3.1 MM/2D-FEM technique to analyze the interior field

A multi-mode horn is often used as a low cross-polarized feed in an offset reflector antenna for space communication applications. Conventionally, posts or regular shaped obstacles are used inside the waveguide to generate the conjugate mode for reducing cross polarization [6–9]. Computation time and accuracy play important roles in feed design and synthesis. As per literature [18, 40–43], a combination of MM and 2-D FEM is suitable to reduce the computational complexity. At the same time, it does not compromise much on the accuracy. Other existing iterative solutions such as 3-D finite difference (FD) [44], 2-D FD/MM [45, 46] and 3-D FDTD [47], are less attractive due to large computation time and memory requirement.

In this chapter, the MM and 2-D FEM techniques are applied for a stepped cylindrical horn containing inner rectangular posts and computational results are verified with the simulated results obtained using HFSS-15. This chapter addresses the convergence issues in calculation of the reaction matrix considering the coupling of the TE and TM modes at the discontinuity surface of the inner waveguide. Proper numerical treatment is applied for accurately predicting the eigenvalues and eigenvectors in calculation of 2-D FEM solution. Although, several works in literature [17, 40, 48–52] have been reported for accurate calculation of reaction matrix, our approach is different from those works. Our approach is elaborated in the subsequent sections.

3.2 Helmholtz equation solution using 2-D FEM technique

In Section 2.1, we have discussed the application of separation of variable technique for solution of wave guide problem. But, such a technique can be applied for waveguides having regular geometry such

as circular, rectangular, elliptical etc. When we need to model waveguide having non-regular geometry or having discontinuity, numerical techniques become more useful. Several numerical techniques such as FDM, FEM, FDTD are available for analysis of such geometry. From literature [53,54], we find that FEM provides very good accuracy. FEM technique for solving the wave equation in guided structure are reported in this chapter.

The wave equation in a homogenous medium as mentioned in Section 2.1 is given by $\nabla^2\phi + k_c^2\phi = 0$. Here, ϕ is the scaler potential of longitudinal magnetic field for TE, longitudinal electric field for TM mode and electric field for TEM mode, respectively. Solution using variation method for ϕ can be obtained by optimizing the integral equation as given below:

$$F(\phi) = \frac{1}{2}\iint \left[|\nabla\phi|^2 - k_c^2\phi^2\right] dS \tag{3.1}$$

The natural boundary conditions i.e. Dirichlet or Neumann boundary conditions must be satisfied. Now, the total surface is split into small sized meshes like triangular, rectangular etc. This small sized mesh is called an element and every element has some nodal points. The scalar potential and nodal point potential for n^{th} element can be written as $\phi_e^n(x,y)$ and ϕ_{ei}^n, where i is the local node number of the n^{th} mesh element. Let the scalar potential in an element vary as:

$$\phi_e^n(x,y) = \overbrace{\underbrace{[1 \quad x \quad y}^{1^{\text{st}}\text{ order}} \quad x^2 \quad y^2 \quad xy \quad x^3 \quad y^3 \quad x^2y \quad xy^2}^{2^{\text{nd}}\text{ order}} \underbrace{.....]}_{3^{rd}\text{ order}} \underbrace{\begin{bmatrix} a_n & b_n & c_n & d_n..... \end{bmatrix}^T}_{\text{Constant}} \tag{3.2}$$

The choice of number of node points (n_p) depends upon the order p of the scalar potential function. The relation between number of node points and order of polynomial is $n_p = \frac{(p+1)(p+2)}{2}$. The constant values of scalar potential function can be evaluated using node points, as specified using cartesian

coordinate values for equation (3.2). The constant values using equation (3.2) can be written as:

$$\begin{bmatrix} a_n \\ b_n \\ c_n \\ \vdots \\ \vdots \end{bmatrix} = \begin{bmatrix} 1 & x_1 & y_1 & x_1^2 & y_1^2 & x_1y_1 & \cdots & \cdots \\ 1 & x_2 & y_2 & x_2^2 & y_2^2 & x_2y_2 & \cdots & \cdots \\ 1 & x_3 & y_3 & x_3^2 & y_3^2 & x_3y_3 & \cdots & \cdots \\ \cdots & \cdots & \cdots & \cdots & \cdots & \cdots & \cdots & \cdots \\ \cdots & \cdots & \cdots & \cdots & \cdots & \cdots & \cdots & \cdots \end{bmatrix}^{-1} \begin{bmatrix} \phi_{e1}^n \\ \phi_{e2}^n \\ \phi_{e3}^n \\ \vdots \\ \vdots \end{bmatrix} \tag{3.3}$$

Combining equations (3.2) and (3.3), the scalar potential function can be written as

$$\phi_e^n(x,y) = \begin{bmatrix} 1 & x & y & x^2 & y^2 & xy & \cdots & \cdots \end{bmatrix} \begin{bmatrix} 1 & x_1 & y_1 & x_1^2 & y_1^2 & x_1y_1 & \cdots & \cdots \\ 1 & x_2 & y_2 & x_2^2 & y_2^2 & x_2y_2 & \cdots & \cdots \\ 1 & x_3 & y_3 & x_3^2 & y_3^2 & x_3y_3 & \cdots & \cdots \\ \cdots & \cdots & \cdots & \cdots & \cdots & \cdots & \cdots & \cdots \\ \cdots & \cdots & \cdots & \cdots & \cdots & \cdots & \cdots & \cdots \end{bmatrix}^{-1} \begin{bmatrix} \phi_{e1}^n \\ \phi_{e2}^n \\ \phi_{e3}^n \\ \vdots \\ \vdots \end{bmatrix} \tag{3.4}$$

Equation (3.4) can also be written as

$$\phi_e^n(x,y) = \begin{bmatrix} \alpha_1 & \alpha_2 & \alpha_3 & \cdots & \cdots \end{bmatrix} \begin{bmatrix} \phi_{e1}^n & \phi_{e2}^n & \phi_{e3}^n & \cdots & \cdots \end{bmatrix}^T \tag{3.5}$$

where α is called the shape function. Substituting the equation (3.5) into equation (3.1), we obtain

$$\begin{aligned} F\left(\phi_e^n\right) = {} & \frac{1}{2}\begin{bmatrix} \phi_{e1}^n & \phi_{e2}^n & \cdots & \cdots \end{bmatrix} \begin{bmatrix} \iint \nabla\alpha_1 \cdot \nabla\alpha_1 ds & \iint \nabla\alpha_1 \cdot \nabla\alpha_2 ds & \cdots & \cdots \\ \iint \nabla\alpha_2 \cdot \nabla\alpha_1 ds & \iint \nabla\vec{\alpha}_2 \cdot \nabla\alpha_2 ds & \cdots & \cdots \\ \cdots & \cdots & \cdots & \cdots \\ \cdots & \cdots & \cdots & \cdots \end{bmatrix} \begin{bmatrix} \phi_{e1}^n \\ \phi_{e2}^n \\ \vdots \\ \vdots \end{bmatrix} \\ & -\frac{k_c^2}{2}\begin{bmatrix} \phi_{e1}^n & \phi_{e2}^n & \cdots & \cdots \end{bmatrix} \begin{bmatrix} \iint \alpha_1\alpha_1 ds & \iint \alpha_1\alpha_2 ds & \cdots & \cdots \\ \iint \alpha_2\alpha_1 ds & \iint \alpha_2\alpha_2 ds & \cdots & \cdots \\ \cdots & \cdots & \cdots & \cdots \\ \cdots & \cdots & \cdots & \cdots \end{bmatrix} \begin{bmatrix} \phi_{e1}^n \\ \phi_{e2}^n \\ \vdots \\ \vdots \end{bmatrix} \\ = {} & \frac{1}{2}[\phi_e^n]^T \left[C_e^{(n)}\right][\phi_e^n] - \frac{k_c^2}{2}[\phi_e^n]^T \left[T_e^{(n)}\right][\phi_e^n] \end{aligned} \tag{3.6}$$

Equation 3.6 is derived for a single element. Solution for the entire region is given by

$$F(\phi) = \sum_{n=1}^{N} F(\phi_e^n) \tag{3.7}$$

From the equations (3.6) and (3.7), $F(\phi)$ can be expressed in matrix from as

$$F(\phi) = \frac{1}{2}[\phi]^T [C] [\phi] - \frac{k_c^2}{2}[\phi]^T [T] [\phi] \tag{3.8}$$

where $\mathbf{C}$ and $\mathbf{T}$ are the global matrices consisting of local $\mathbf{C}_e^{(n)}$ and $\mathbf{T}_e^{(n)}$ matrices coefficients, respectively and $[\phi]$ represents the scalar value of all the node points over the global surface. N presents the total number of elements of entire surface.

3.2.1 Solution of TEM and TE modes

TEM and TE modes must satisfy the Neumann boundary condition. The solution of TEM and TE mode will be optimization of equation 3.8 with respect to $[\phi]$. So, $\frac{\partial F(\phi)}{\partial [\Phi]} = 0$.
$[C - k_c^2 T][\phi] = 0$ or

$$[T^{-1}C - k_c^2 I][\phi] = 0 \tag{3.9}$$

where $\mathbf{I}$ is the unit matrix. $\mathbf{k}_c^2$ is the eigenvalues of $\mathbf{T}^{-1}C$ matrix and it should be real quantity as $\mathbf{C}$ and $\mathbf{T}$ are symmetric matrices. In case of TEM mode, k_c is equal to zero and the solution of the eigenvector will be the scalar potential.

3.2.2 Solution of TM modes

In case of TM mode, the boundary condition should support the Dirichlet boundary condition. So, the scalar potential at the boundary nodes (ϕ_p) should be zero. From the equation (3.8), we can write for the prescribed nodes $[\phi_p]$ and the free nodes $[\phi_f]$ as:

$$F(\phi) = \frac{1}{2}\begin{bmatrix} \phi_f & \phi_p \end{bmatrix}\begin{bmatrix} C_{ff} & C_{fp} \\ C_{pf} & C_{pp} \end{bmatrix}\begin{bmatrix} \phi_f \\ \phi_p \end{bmatrix} - \frac{k_c^2}{2}\begin{bmatrix} \phi_f & \phi_p \end{bmatrix}\begin{bmatrix} T_{ff} & T_{fp} \\ T_{pf} & T_{pp} \end{bmatrix}\begin{bmatrix} \phi_f \\ \phi_p \end{bmatrix} \tag{3.10}$$

Here $\frac{\partial F(\phi)}{\partial [\Phi_f]} = 0$. So, TM mode solution should be $[T_{ff}^{-1}C_{ff} - k_c^2 I][\phi_f] = 0$.

3.2.3 Surface Meshing

Surface mesh plays an important role in performance of the numerical electromagnetic calculations. Several types of mesh such as triangular, rectangular, hexagonal or their mixed types are generally used for surface meshing. Mainly, triangular mesh having the ability to handle any arbitrary surface are widely used. One of the triangular mesh is Delaunay triangle. It is used for numerical electromagnetic calculation due to the availability of fast algorithm for Delaunay triangulation and in such schemes the absence of similar type of triangle improves the error performance in electromagnetic calculations done numerically [55]. To develop the FEM code, PDE Toolbox in MATLAB for Delaunay triangulation has been used. Some codes for graphics interface are developed to draw the desired surface in PDE Toolbox and collect the information as required. Basically, the information of triangulation are presented as position vector of node points (it specifies the node number and their position in cartesian coordinate) and a vector which contains nodes' number for every triangle and its sub-area information. To close the PDE tool box after it is used, a code has been developed. Any type of planer objects in PDE Toolbox can be drawn using circle, rectangular, elliptical, polygon and using the operations of substraction, intersection and union etc. Also, a MATLAB code is written to identify the boundary nodes and interior nodes of the surface. Specifically, interior nodes are used for TM mode solution and sometimes boundary nodes are also used for triangulation of 3D objects. The boundary edge size can be controlled using step size for triangulation. In Figure 3.1-(a), we represent the property of Delaunay triangular mesh in which the nodes of a triangle cannot be located inside the circum-circle. Also, different objects (rectangle R_1, R_2, R_3 and circle C_1) for triangulation using the operation of intersection, union and substraction, respectively are drawn in Figure 3.1-(b). The sub-area of its surfaces (1, 2, 3 and 4) are also presented in same Figure.

3.2.4 Evaluation of local coefficient matrix in closed form

2D-FEM code has been implemented based on scalar potential as a 1^{st} order polynomial using the Delaunay triangular mesh. Closed form matrix of local $C_e^{(n)}$ and $T_e^{(n)}$ are formulated on the basis of Appendix 8.2 as given below:

$$\mathbf{C}_e^{(n)} = \frac{1}{4A_n}[p_i p_j + q_i q_j]_{3\times 3} \qquad \text{where } i = 1,2,3 \;\&\; j = 1,2,3 \tag{3.11}$$

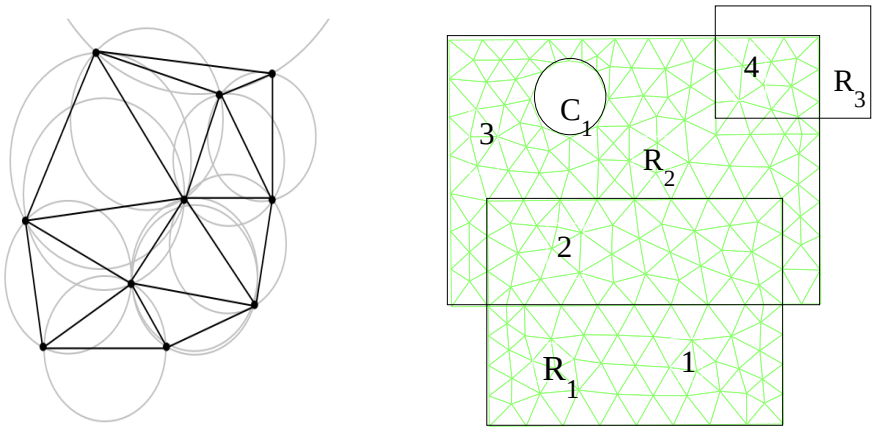

Figure−a Figure−b

Figure 3.1: Triangular mesh.

$$\mathbf{T}_e^{(n)} = \frac{A_n}{12}\begin{bmatrix} 2 & 1 & 1 \\ 1 & 2 & 1 \\ 1 & 1 & 2 \end{bmatrix} \tag{3.12}$$

where $p = [y_2 - y_3,\ y_3 - y_1,\ y_1 - y_2]$, $q = [x_3 - x_2,\ x_1 - x_3,\ x_2 - x_1]$ and A_n is the surface of the n^{th} element (triangle). The global coefficient matrices are assembled using the values of local $\mathbf{C}_e^{(n)}$ and $\mathbf{T}_e^{(n)}$ matrix for the FEM solution as specified in Appendix 8.3.

3.2.5 Eigenvalue and eigenvector calculation for mode solution

The eigenvalue and eigenvector of equation (3.8) are accurately solved using Lanczo's procedure by generating the tri-diagonal matrix to accelerate the convergence [40]. Gram-Schmidt-type re-orthogonalisation is exploited to ensure better orthogonality even for higher-order degenerate modes and in each Lanczo's iteration, the eigenvalue is evaluated by making a sparse matrix using the minimum degree algorithm of Cholesky decomposition.

3.3 Reaction matrix calculation of MM/2D-FEM technique

As mentioned in Section 2.2, reaction matrix will lead the solution of scattering parameter in MM technique. The calculation of reaction matrix for any type of junction is presented in this section.

In real scenario, there may be a junction where both side fields are analytically known but closed

Table 3.1: "s", "b", L_s and Ω_s represent the small, big waveguide, boundary and surface of small waveguide.

Calculation of Reaction matrix			
Matrix element	coupling	Surface-integral	Line-integral
$\langle e_s^e \cdot e_b^e \rangle$	TE-TE	$\iint\limits_{\Omega_s} \nabla_t \psi_s^e \cdot \nabla_t \psi_b^e \, d\Omega_s$ $k_s^2 \iint\limits_{\Omega_s} \psi_s^e \psi_b^e \, d\Omega_s$	$\frac{k_s^2}{k_s^2 - k_b^2} \oint\limits_{L_s} \psi_s^e \frac{d\psi_b^e}{dn} \, dL_s$ $-\frac{k_s}{2} \oint\limits_{L_s} \psi_s^e \frac{d^2 \psi_b^s}{dk_b dn} \, dL_s \quad k_s \simeq k_b$
$\langle e_s^h \cdot e_b^h \rangle$	TM-TM	$\iint\limits_{\Omega_s} \nabla_t \psi_s^h \cdot \nabla_t \psi_b^h \, d\Omega_s$ $k_b^2 \iint\limits_{\Omega_s} \psi_s^h \psi_b^h \, d\Omega_s$	$\frac{k_b^2}{k_b^2 - k_s^2} \oint\limits_{L_s} \frac{d\psi_s^h}{dn} \psi_b^h \, dL_s$ $\frac{k_b}{2} \oint\limits_{L_s} \frac{d\psi_s^h}{dn} \frac{d\psi_b^h}{dk_b} \, dL_s \quad k_s \simeq k_b$
$\langle e_s^e \cdot e_b^h \rangle$	TE-TM	$\iint\limits_{\Omega_s} \nabla_t \psi_s^e \times \nabla_t \psi_b^h \, d\Omega_s$	$\oint\limits_{L_s} \psi_s^e \frac{d\psi_b^h}{dL_s} \, dL_s$ $- \oint\limits_{L_s} \frac{d\psi_s^e}{dL_s} \psi_b^h \, dL_s$
$\langle e_s^h \cdot e_b^e \rangle$	TM-TE	0	0

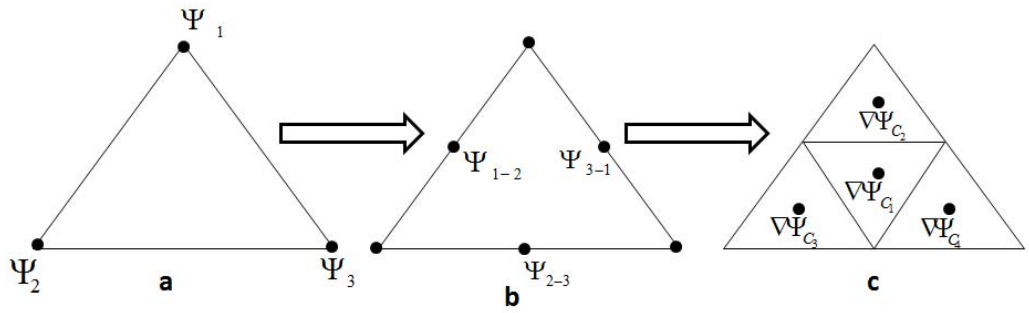

Figure 3.2: a : ψ_1, ψ_2, ψ_3 represent the known scalar potential after FEM solution. b : $\psi_{1\_2}, \psi_{2\_3}, \psi_{3\_1}$ are interpolated scalar potential at the middle edges using the cubic interpolation. c : $\nabla\psi_{C_1}, \nabla\psi_{C_2}, \nabla\psi_{C_3}, \nabla\psi_{C_4}$ are predicted gradient of scalar potential at barycenter points using 2^{nd} order polynomial function.

Table 3.2: Scaler potential calculation using Green's identity.

Normalized the scalar potential		
Mode	Surface-integral	Line-integral
TE	$\iint\limits_{\Omega} \nabla_t \psi^e \cdot \nabla_t \psi^e \, d\Omega$ $k_c^2 \iint\limits_{\Omega} \psi^e \psi^e \, d\Omega$	$-\frac{k_c}{2} \oint\limits_{L} \psi^e \frac{d^2 \psi^e}{dk_c dn} \, dL$
TM	$\iint\limits_{\Omega} \nabla_t \psi^h \cdot \nabla_t \psi^h \, d\Omega$ $k_c^2 \iint\limits_{\Omega} \psi^h \psi^h \, d\Omega$	$\frac{k_c}{2} \oint\limits_{L} \frac{d\psi^h}{dn} \frac{d\psi^h}{dk_c} \, dL$

from of reaction matrix is not available, or one side field is known but other side field needs to be calculated numerically or both side fields need to be calculated numerically. For all such cases, reaction matrix needs to be calculated using numerical integration. There are few cases where closed-from expressions of reaction matrix are available for regular faces, some of them are addressed in Section 2.3. The numerical calculation of reaction matrix and normalization of the eigenvector can be done using surface or line integral according to Table 3.1 and 3.2, which are reported in [17, 40, 49–52]. Use of line integral reduces the computational complexity. However, there is problem in convergence due to limited accuracy in prediction of eigenvalue and eigenvector solution for FEM. The error is high when both side fields are solved using numerical method and also it is required to give a special treatment for degenerated modes as in Table 3.1. For the general solution of the normalized eigenvector and reaction matrix, surface integral containing gradient terms is a better choice to avoid the convergence of line integrals. To implement the gradient based surface integral, cubic interpolation is used to predict the scalar potential at the middle of the edges of a triangle as shown in Figure 3.2. Gradients at four barycenter points as in Figure 3.2(c), are calculated by forming the second order polynomial making use of the scalar potentials at the six points on the edges of the triangle as shown in Figure 3.2(b).

3.4 Results

FEM code performance is verified for rectangular and circular waveguide by comparing with analytical results. In Figure 3.3, we plot the first 16 modes of a rectangular waveguide and their contour plot of scalar potential function and quiver plot for electric field distribution. We have compared the normalized scalar potential distribution with analytical solution for TE_{11} and TM_{11} mode of rectangu-

lar waveguide in Figure 3.4 and 3.5 using 278 node points and 502 number of triangles. It is observed, normalized field distribution obtained analytically match closely with the computed results obtained using FEM. In Figure 3.6, we plot the field distribution for circular wave guide using this numerical code.

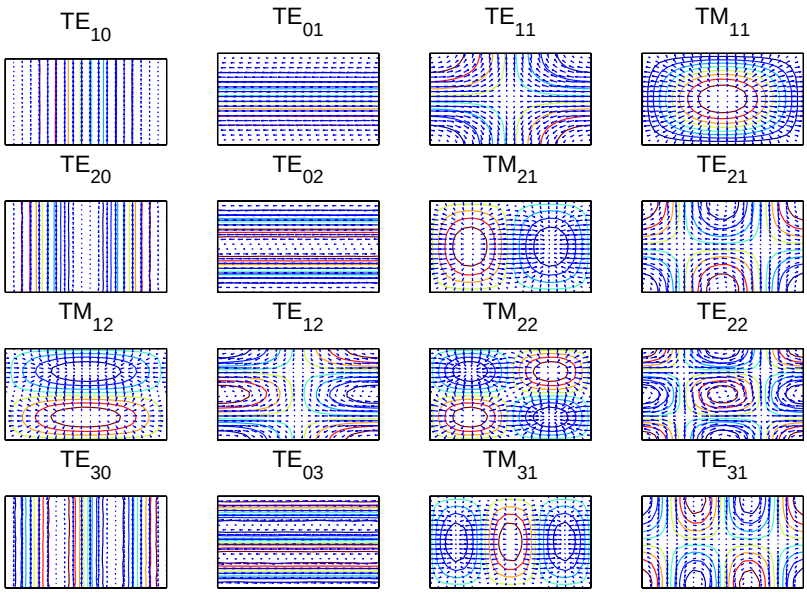

Figure 3.3: First 16 modes of rectangular waveguide: contour plot (solid: −) of scalar potential function and quiver plot (arrow: →) for electric field distribution.

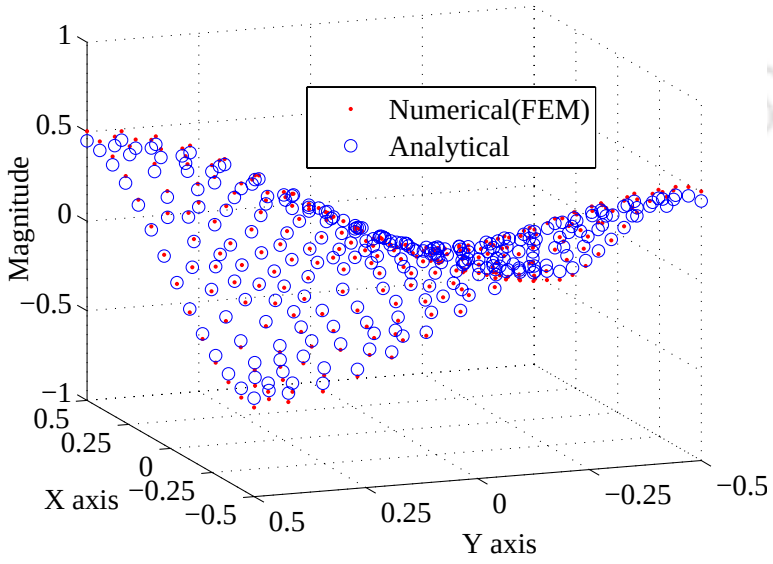

Figure 3.4: Normalized scalar potential value, comparison for rectangular TE_{11} mode with analytical and numerical (FEM).

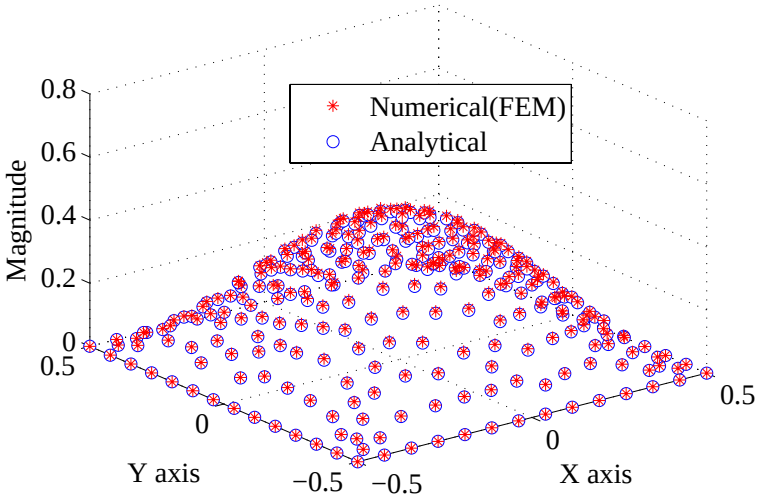

Figure 3.5: Normalized scalar potential value, comparison for rectangular TM_{11} mode with analytical and numerical (FEM).

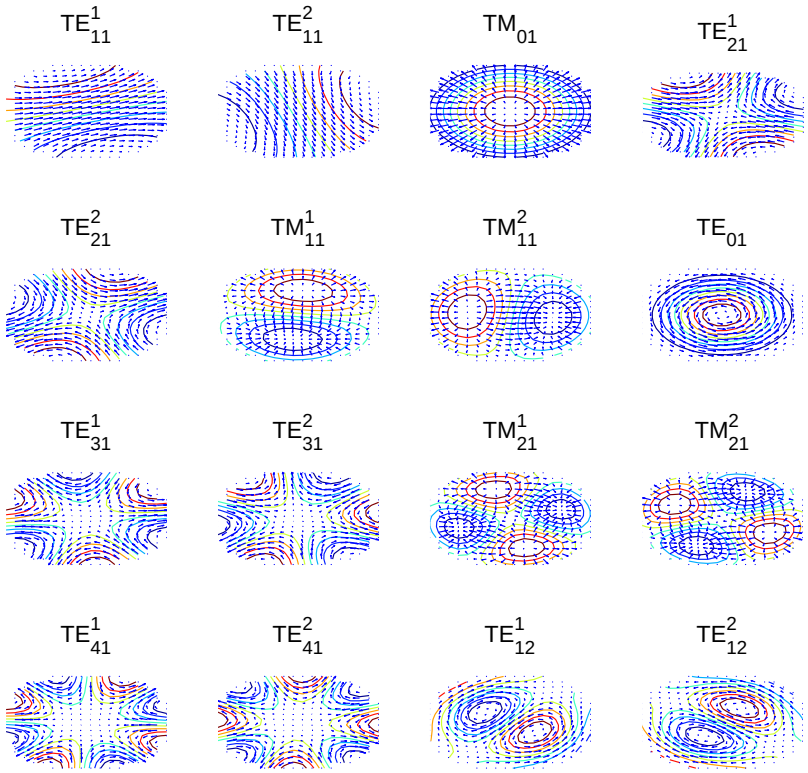

Figure 3.6: Field distribution of circular waveguide: their contour plot (solid: −) of scalar potential function and quiver plot (arrow: →) of electric field distribution.

In Table 3.3, the cutoff wavelengths (k_c) are compared for first 16 modes of rectangular and circular wave guide using the FEM and analytical techniques.

Table 3.3: Performance of developed FEM code

rectangular wave guide (dimension $a = 1, b = 1$)			circular wave guide (dimension radius $r = 1$)		
mode	k_c ($p = 278, t = 502$)		mode	k_c ($p = 373, t = 688$)	
	Analytical	Numerical (FEM)		Analytical	Numerical (FEM)
TE_{01}	3.1416	3.1468	TE_{11}^{1}	1.8412	1.8446
TE_{10}	3.1416	3.1468	TE_{11}^{2}	1.8412	1.8446
TE_{11}	4.4429	4.44567	TM_{01}	2.4048	2.41
TM_{11}	4.4429	4.44574	TE_{21}^{1}	3.0542	3.0653
TE_{02}	6.2832	6.3224	TE_{21}^{2}	3.0542	3.0654
TE_{20}	6.2832	6.3243	TE_{01}^{2}	3.8317	3.8522
TE_{12}	7.0248	7.0787	TM_{11}^{1}	3.8317	3.8524
TE_{21}	7.0248	7.0802	TM_{11}^{2}	3.8317	3.8559
TM_{12}	7.0248	7.0802	TE_{31}^{1}	4.2012	4.2280
TM_{21}	7.0248	7.0817	TE_{31}^{2}	4.2012	4.2286
TE_{22}	8.8858	8.9962	TM_{21}^{1}	5.1356	5.1841
TM_{22}	8.8858	9.0014	TM_{21}^{2}	5.1356	5.1850
TE_{03}	9.4248	9.5674	TE_{41}^{1}	5.3176	5.3713
TE_{30}	9.4248	9.5725	TE_{41}^{2}	5.3176	5.3720
TE_{13}	9.9346	10.0813	TE_{12}^{1}	5.3314	5.3908
TE_{31}	9.9346	10.0881	TE_{12}^{2}	5.3314	5.3914

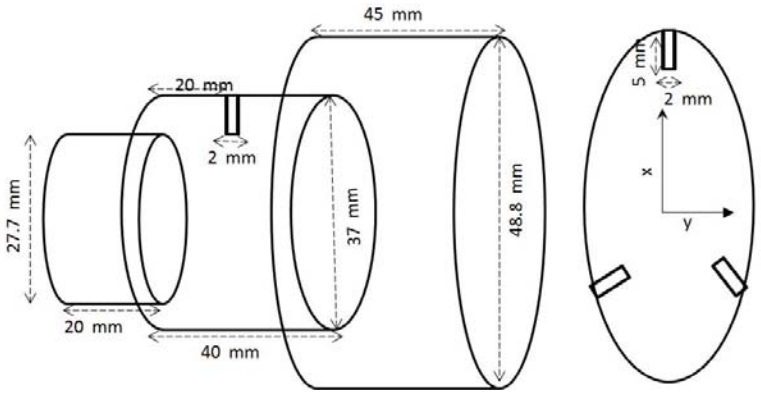

Figure 3.7: Horn structure to evaluate the hybrid numerical code performance.

A MATLAB code is developed to study the performance of this hybrid technique for a X-band tri-mode horn configuration shown in Figure 3.7. For performing FEM based computation for post area, 2914 number of triangles are generated and the 350 numbers of modes are considered for the MM solution at the junctions. The results obtained for MM/2D-FEM computation are compared with HFSS-15 results in Figure 3.8, 3.9. It can be seen that computed results are close to HFSS results.

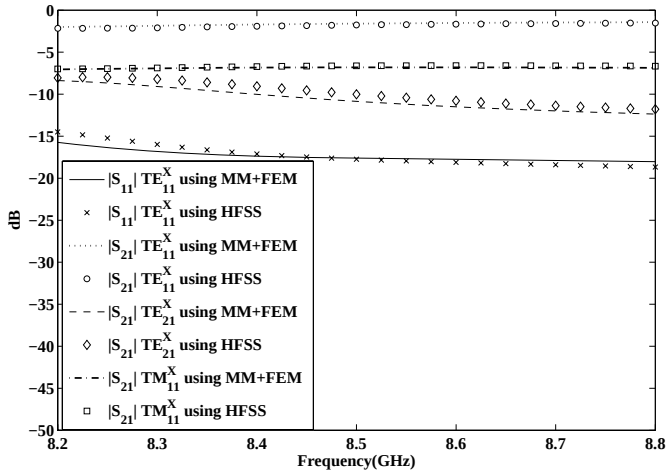

Figure 3.8: A comparison of scattering parameters' magnitude computed using HFSS and the hybrid technique.

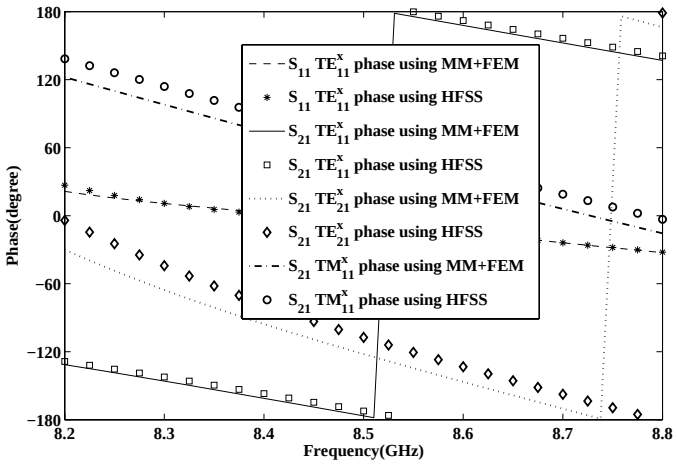

Figure 3.9: A comparison of scattering parameters' phase computed using HFSS and the hybrid technique.

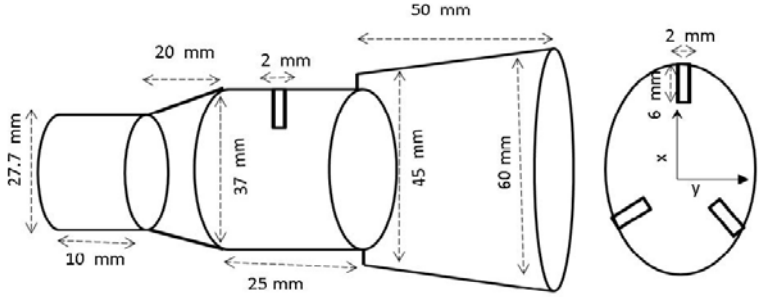

Figure 3.10: A tri-mode smooth wall horn structure to evaluate the hybrid numerical code performance.

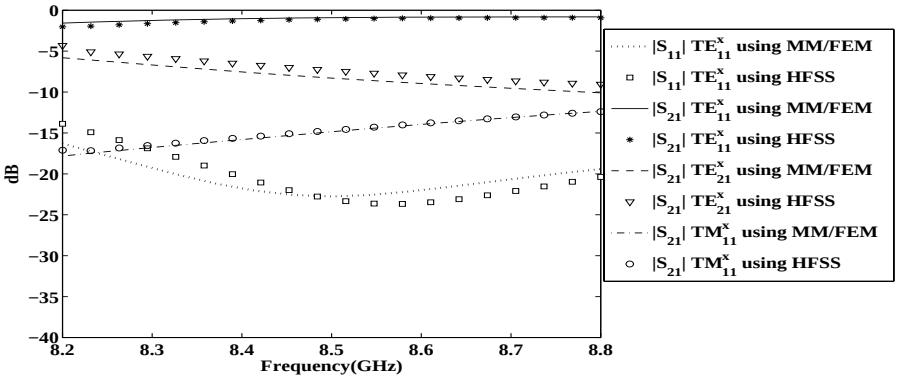

Figure 3.11: A comparison of scattering parameters' magnitude computed using HFSS and the hybrid technique.

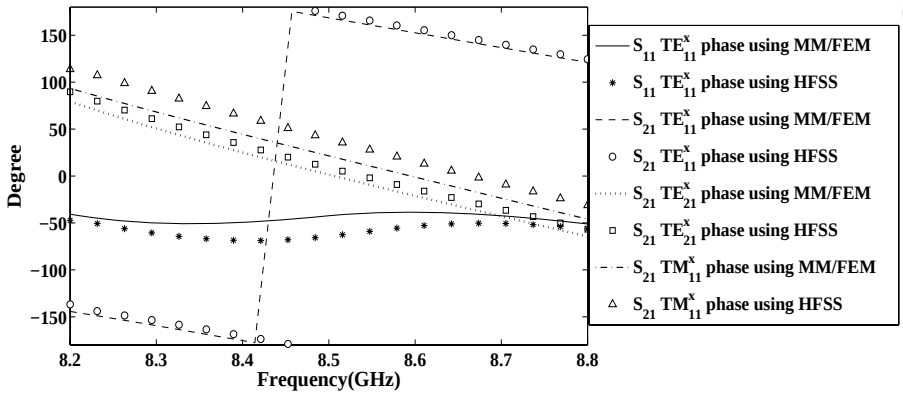

Figure 3.12: A comparison of scattering parameters' phase computed using HFSS and the hybrid technique.

Table 3.4: The performances of HFSS-15 for 0.0001 error specification and MM/2D-FEM for 350 modes in terms of computation time and required RAM are specified. The computation has been performed for 15 spot frequencies.

Parameters of performance	HFSS-15	MM/2D-FEM
Simulation time	1:2:10 hours	0:5:18 hours
Used memory (RAM)	2.43 GB	0.87 GB

A tri-mode smooth-walled horn structure containing tapered sections is also studied using this hybrid technique and the horn configurations are shown in the Figure 3.10. At the post area, 2054 number of triangles are used for the FEM computation and total 350 number of modes are considered for the MM solution. The computed and simulated results are compared in Figure 3.11, 3.12 and close match is obtained.

The performances of MM/2D-FEM and HFSS-15 are compared in Table 3.4 in terms of computation time and the required RAM for the first considered structure shown in Figure 3.7. The performance has been evaluated by running the codes on an Intel core-4 2400-CPU, 8 GB RAM desktop. The results in Table 3.4 demonstrates the effectiveness of the proposed method.

3.5 Conclusion

The performance of a hybrid technique employing MM/2D-FEM has been investigated for a tri-mode stepped circular waveguide structures containing rectangular posts. Such geometries are used in design of multi-mode horns and the hybrid technique is applied for interior field analysis. It has been found to be a reasonably accurate method for analyzing structures containing steps and discontinuity in the form of posts. In this study, a large number of modes have been used to study the tri-mode horn and the results have been found to be converging. It has been observed that for obtaining similar convergence, HFSS takes much longer computational time for the considered structures which are investigated using the MM/2D-FEM technique.

भारतीय प्रौद्योगिकी संस्थान गुवाहाटी
Indian Institute of Technology Guwahati

4

Analysis of Open Ended Waveguide using MoM Technique

Contents

This chapter discusses the theory based on which the aperture problem related to multi-mode horn is modeled using the method of moment (MOM). The Rao-Willton-Gillson function (RWG) and Delaunay triangulations are used for 2D MOM solution to model for cases of horn having finite and infinite ground plane. Kirchhoff-Huygen's principle has been applied to model the horn aperture on a finite ground plane. The singular problem of the solution of scattering electric and magnetic field equation (EFIE, MFIE) is also described in this modeling. The performance of several horn structures are investigated using those techniques and the results are also compared with the simulated results obtained using HFSS-15. The theory behind the calculation of approximate far field pattern of multi-mode feed using Chu's model (analytical model) is also elaborately explained.

4.1 Evaluation of open ended waveguide problem using MoM technique

In literature, open ended waveguide problem has been investigated using several techniques such as 3-D model using iterative solution like finite difference time domain (FDTD), finite difference method (FDM), boundary element method (BEM) [56–58], as well as 2-D MOM, Fourier transform method and using spherical wave functions. The parameters like computation time and accuracy for the solution of open ended waveguide problem play the important roles in developing the model of antenna array and the feed for reflector antenna. Use of spherical wave functions for open ended problem is a popular technique and it has similarity with the mode matching technique. However, some drawbacks are reported in literature such as convergence depends on the choice of number of modes [59]. The open ended wave guide problem has been investigated using computationally less intensive techniques such as analytical aperture distribution method [60], spectral domain method [61] and geometric optics (GO)-geometric theory of diffraction (GTD) [62]. The spectral domain method has a poor performance in predicting the back side scattered field. Analytical aperture distribution method can not predict accurately the scattering parameters and back-side scatter. The GO-GTD method has a drawback for the prediction of co-polarization and cross polarization and it cannot predict the scattering parameter [62]. To solve the scattering problem, 2D-MoM technique is generally preferable in terms of accuracy and amount of computation involved as suggested in literature [63–66]. Three types of 2D-MoM technique for the solution of open ended wage-guide problem are reported in literature: first method gives an approximate solution considering the aperture on an infinite

ground plane [63], second method applies Kirchhoff-Huygen's principle at outer region of horn [65] and the third method involves solution using hybrid field integral equation (HFIE) [64]. It is well known that the solution of MoM technique depends on the choice of orthogonal functions. For our problem, two kinds of orthogonal functions are quite efficient such as body of revolution function (BoR) and Rao, willton and Gilson function (RWG) [67]. Somehow, BoR function [68] has the ability to decrease the computation by the analytical conversion of scattering formula from two dimensional to one dimensional integration. But, it requires a considerable effort to deal with such analytical formulations. To avoid such effort, we mainly consider the RWG function to solve the open ended waveguide problem.

In this chapter the modeling of open ended waveguide problem is formulated based on the first and second methods employing 2D-MoM technique as discussed earlier. The following subsection provides the details.

4.2 MoM formulation for open ended waveguide having infinite ground plane

The entire structure of horn aperture, according to [69], is subdivided into two regions, region-I: inner region and region-II: outer region. The tangent magnetic field which is continuous at the common aperture, follows the equation

$$\vec{H}_{tan}^{inn} = \vec{H}_{tan}^{hs}. \tag{4.1}$$

where $\vec{H}_{tan}^{inn}$ and $\vec{H}_{tan}^{hs}$ represent the inner and outer magnetic field. Both regions are unattached by a perfect electric conductor at the common aperture (S_a) as shown in Figure 4.1.

4.2.1 Region-I

The MoM technique is applied for the solution of the equation (4.1) using the linearly independent testing functions. Magnetic surface current ($M_S(r)$) can be written in terms of basis functions as:

$$\vec{M}_S(r) = \eta \sum_{m=1}^{M} V_m \vec{M}_m(r) \qquad r \text{ on } S_a, \tag{4.2}$$

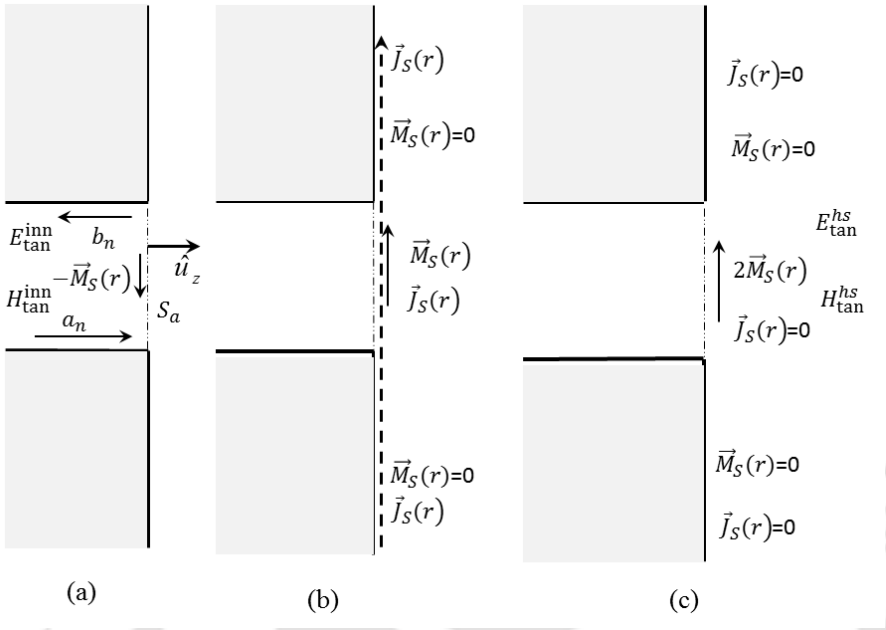

Figure 4.1: Equivalent half space scattering model of horn, (a)-region-I, (b)-region-II, (c)-equivalent model of region-II

where η, $\vec{M}_m(r)$, V_m and M respectively are the free space impedance, basis orthogonal function, the expansion coefficient and number of basis functions. Magnetic source current can be defined using the equivalent principle that

$$\vec{M}_S(r) = -\hat{u}_z \times \vec{E}_{tan}^{inn}|_{z=0} \tag{4.3}$$

If d_n, a_n, b_n, $\mathbf{e}_n$, $\mathbf{h}_n$, Y_n, γ_n and N are the electric field amplitude of the equivalent fictitious magnetic current, forward coefficient, backward coefficient, electric field, magnetic field, admittance, propagation constant of different modes and number of modes, respectively, the inner field equations can be written from [69] as:

$$\vec{E}_{\tan}^{inn} = \sum_{n=1}^{N} a_n \mathbf{e}_n e^{-\gamma_n z} + \sum_{n=1}^{N} b_n \mathbf{e}_n e^{\gamma_n z} = \sum_{n=1}^{N} a_n \mathbf{e}_n e^{-\gamma_n z} - \sum_{n=1}^{N} a_n \mathbf{e}_n e^{\gamma_n z} + \sum_{n=1}^{N} d_n \mathbf{e}_n e^{\gamma_n z} \tag{4.4}$$

and

$$\vec{H}_{\tan}^{inn} = \sum_{n=1}^{N} a_n \mathbf{h}_n Y_n e^{-\gamma_n z} - \sum_{n=1}^{N} b_n \mathbf{h}_n Y_n e^{\gamma_n z} = \sum_{n=1}^{N} a_n \mathbf{h}_n Y_n e^{-\gamma_n z} + \sum_{n=1}^{N} a_n \mathbf{h}_n Y_n e^{\gamma_n z} - \sum_{n=1}^{N} d_n \mathbf{h}_n Y_n e^{\gamma_n z} \tag{4.5}$$

where

$$[d_n] = [b_n] + [a_n]. \tag{4.6}$$

The fictitious magnetic source can be written at the common aperture for $z = 0$ from the equations (4.3) and (4.4) as

$$\vec{M}_S(r) = -\sum_{n=1}^{N} d_n \hat{u}_z \times \mathbf{e}_n = -\sum_{n=1}^{N} d_n \mathbf{h}_n \tag{4.7}$$

$[d_n]$ can be derived using the orthogonal property of different mode-fields from the equations (4.7) and (4.2) as

$$[d_n]_{N\times 1} = -\eta[\left\langle \mathbf{h}_n, \vec{M}_m(r) \right\rangle]_{N\times M}[V_m]_{M\times 1} = -\eta[A_{nm}]_{N\times M}[V_m]_{M\times 1} \tag{4.8}$$

The equation (4.1) which provides the solution of scattering parameter and unknown magnetic current coefficients, can be written using the testing function $w_p(r)$ as:

$$\left\langle \vec{w}_p(r), \vec{H}^{inn}_{\tan} \right\rangle = \left\langle \vec{w}_p(r), \vec{H}^{hs}_{\tan} \right\rangle. \tag{4.9}$$

The number of $\vec{w}_p(r)$ is equal to the number of unknown basis functions ($\vec{M}_m(r)$) used to evaluate the unknown magnetic current coefficients. The solution of the equation (4.9) for the inner field part can be written using the equation (4.5) as:

$$\left[\left\langle \vec{w}_p(r), \vec{H}^{inn}_{\tan} \right\rangle\right] = 2[B_{mn}]_{M\times N}[Y_{nn}]_{N\times N}[a_n]_{N\times 1} - [B_{mn}]_{M\times N}[Y_{nn}]_{N\times N}[d_n]_{N\times 1} \tag{4.10}$$

where $[B_{mn}]_{M\times N} = [\langle \vec{w}_p(r), \mathbf{h}_n \rangle]_{M\times N}$.

Substituting the value of $[d_n]$ from the equation (4.8) into equation (4.10) for the inner region, the following can be obtained:

$$[\left\langle \vec{w}_{p(r),} \vec{H}^{inn}_{\tan} \right\rangle] = \left[I^{inc}\right]_{M\times N}[a_n]_{N\times 1} - \left[Y^{inn}_{pm}\right]_{M\times M}[V_m]_{M\times 1}. \tag{4.11}$$

where incident current on the aperture can be written as $\left[I^{inc}\right]_{M\times N} = 2[B_{mn}]_{M\times N}[Y_{nn}]_{N\times N}$ and inner admittance matrix is defined as $[Y^{inn}_{pm}] = -\eta[B_{mn}]_{M\times N}[Y_{nn}]_{N\times N}[A_{nm}]_{N\times M}$.

4.2.2 Region-II

When region-II is separated from region-I, a flat plane PEC is imagined at the aperture and an infinite plane is assumed as shown in Figure 4.1. A nonzero electric current ($\vec{J}_S$) over the whole infinite surface and a magnetic current ($\vec{M}_S$) on the common aperture will be induced. By the image theory, the analogous current can be represented as a magnetic current having twice the strength ($2\vec{M}_S$) of the original magnetic current on the aperture. On the other hand, the electric current ($\vec{J}_S = 0$) is zero on the whole surface as shown in Figure 4.1.

At the outside region, the magnetic field is defined according to Kirchhoff-Huygen's principle as:

$$\vec{H}_{tan}^{hs} = -j\frac{2}{\eta k}\left[k^2 \iint_{s'} \vec{M}_S(r')G(r,r')d\vec{s}' + \nabla \iint_{S'} \nabla' \cdot \vec{M}_S(r')G(r,r')d\vec{s}'\right] \tag{4.12}$$

where $G(r,r) = \frac{e^{-jk|\mathbf{r}-\mathbf{r}'|}}{4\pi|\mathbf{r}-\mathbf{r}'|}$.

For the solution of the equation (4.9), using equation (4.12), we can write

$$\left[\left\langle \vec{w}_p(r), \vec{H}_{\tan}^{hs} \right\rangle\right] = \left[Y_{pm}^{hs}\right]_{M\times M}[V_m]_{M\times 1}, \tag{4.13}$$

where $\left[Y_{pm}^{hs}\right]$ is the admittance matrix of region-II which can be defined as:

$$\left[Y_{pm}^{hs}\right] = -j\frac{2}{\eta k^2}\left[\int_{S_p}\int_{S'_m}\left(k^2\vec{w}_p(r)\cdot\vec{M}_m(r') - \nabla\cdot\vec{w}_p(r)\nabla\cdot\vec{M}_m(r')\right)G(r,r')d\vec{S}'_m d\vec{S}_p\right]_{M\times M} \tag{4.14}$$

4.2.3 Implementation

To implement the MoM technique, Delaunay triangles are used for the triangulation of common aperture and RWG function is used as a basis and testing function.

4.2.3.1 Evaluation of the aperture scattering parameter

Once, the inner admittance matrix and outer admittance matrix are calculated, next step is to calculate the expansion coefficients of magnetic current for different modes. Using the equations (4.11), (4.13) and (4.9), the expansion coefficients of magnetic current for different ($[V_{mn}]$) modes can

be derived as:

$$[V_{mn}]_{M\times N} = \left[Y_{pm}^{inn} + Y_{pm}^{hs}\right]_{M\times M}^{-1} [I^{inc}]_{M\times N},$$

where

$$[V_m]_{M\times 1} = [V_{mn}]_{M\times N}[a_n]_{N\times 1} \tag{4.15}$$

and the ratio between backward and forward wave at the inner region can be calculated using the equations (4.6), (4.8) and (4.15) as:

$$[s_{ij}]_{N\times N} = -\eta[A_{nm}]_{N\times M}[V_{mn}]_{M\times N} - [I]_{N\times N},$$

Here, $[I]_{N\times N}$ is the unit matrix. The modal scattering parameter can be calculated as:

$$[S_{11}^A] = [Y_{nn}]_{N\times N}^{0.5} [s_{ij}]_{N\times N} [Y_{nn}]_{N\times N}^{-0.5} \tag{4.16}$$

4.2.3.2 Combined MoM and MM technique

Scattering parameter for the full structure (S_{11}^{ful}) can be evaluated by combining the interior junction scattering parameters and the aperture scattering parameter (S_{11}^A) using GSP technique as mentioned in Chapter 2. Once the calculation of the scattering parameters for the full structure is completed, next step is to calculate the radiation patterns. The surface magnetic current which is used to calculate the radiation patterns, is evaluated using the incident interior field coefficients at aperture (equation: (4.15)). To calculate the forward coefficient of the incident wave, we draw a signal flow graph as illustrated in Figure 4.2 and the solution of the forward coefficients at the aperture are given by equation (4.17). The unknown surface magnetic current coefficients can be evaluated using equation (4.15).

$$[a_n] = \left[\sqrt{Y_n}\right]^{-1} \left[I - S_{22}S_{11}^A\right]^{-1} [S_{21}] \left[V_0^+\right] \tag{4.17}$$

where $[V_A^+] = [\sqrt{Y_n}][a_n]$.

4.2.4 Choice of RWG function

There are two types of RWG function as reported in [67], type-I: function for which the divergence factor is constant and type-II: function for which the divergence factor is zero. In the solution of MoM

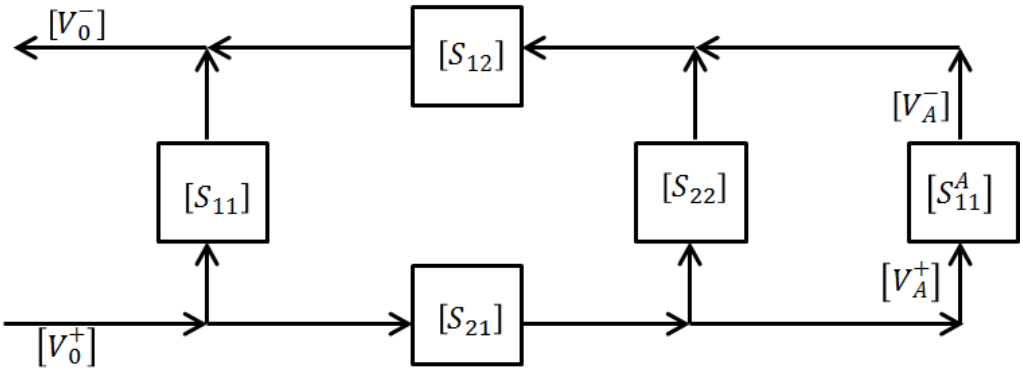

Figure 4.2: Equivalent signal flow graph for calculation of forward incident field coefficient at the aperture.

equation (4.13), testing and basis function would be type-I, otherwise the choice of type-II will lead to a solution which is similar to a pulse type basis function. In the subsequent equations, RWG functions are specified using the common edge between two neighboring triangles where one is positive and the other is negative as shown in Figure 4.3.

$$\vec{f}_n^1(r) = \begin{cases} \frac{l_n}{2A_n^+}(\mathbf{r} - \mathbf{r}_{f_n}^+) & \mathbf{r}\ in\ T_+^n \\ \frac{l_n}{2A_n^-}(\mathbf{r}_{f_n}^- - \mathbf{r}) & \mathbf{r}\ in\ T_-^n \end{cases} \qquad \nabla \cdot \vec{f}_n^1(r) = \begin{cases} \frac{l_n}{A_n^+} & \mathbf{r}\ in\ T_+^n \\ -\frac{l_n}{A_n^-} & \mathbf{r}\ in\ T_-^n \end{cases}$$

$$\vec{f}_n^2(r) = \begin{cases} \frac{l_n}{2A_n^+}\hat{n} \times (\mathbf{r} - \mathbf{r}_{f_n}^+) & \mathbf{r}\ in\ T_+^n \\ \frac{l_n}{2A_n^-}\hat{n} \times (\mathbf{r}_{f_n}^- - \mathbf{r}) & \mathbf{r}\ in\ T_-^n \end{cases} \qquad \nabla \cdot \vec{f}_n^2(r) = \begin{cases} 0 & \mathbf{r}\ in\ T_+^n \\ 0 & \mathbf{r}\ in\ T_-^n \end{cases}$$

Here, $A_n^{\pm}$ are respectively area of positive and negative triangle. $\mathbf{r}_{f_n}^+$, $\mathbf{r}_{f_n}^-$ and l_n are free vertex of positive triangle, negative triangle and the length of the common edge, respectively.

4.2.4.1 Evaluation of the MoM Integrals

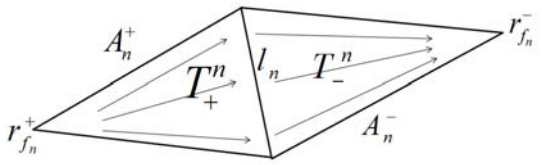

Figure 4.3: RWG basis function.

In order to strike a balance between computation and performance, the choice of appropriate numerical integration for the triangular surface plays an important role. Gaussian quadrature seven points integration for source point and Gaussian quadrature three points integration for observation point are chosen to solve the equation (4.14).

In the MoM solution, three types of singularities are obtained which are due to: (a) self triangle (b) common edge with other triangles and (c) common node with other triangles. Literature provides techniques to compute the singularities [70, 71]. However, inclusion of these singularities increase the computation time. In view of this, self coupling has been taken care of in our developed code. On the other hand, the effect of the other two singularities are less as compared to that of self coupling. The closed-form expression used to handle self singularity is given below:

$$\int_{T_s}\int_{T_{s'}} G(r,r')dT_s dT_{s'} = \underbrace{\int_{T_s}\int_{T_{s'}} [G(r,r') - \frac{1}{4\pi\left|\mathbf{r}-\mathbf{r'}\right|}]dT_s dT_{s'}}_{\text{Numerical}} + \underbrace{\int_{T_s}\int_{T_{s'}} \frac{1}{4\pi\left|\mathbf{r}-\mathbf{r'}\right|}dT_s dT_{s'}}_{\text{Analytical}}$$

$$\frac{1}{4A^2}\iint_{T_s}\iint_{T_{s'}} \frac{1}{|\mathbf{r}-\mathbf{r'}|}dT_s dT_{s'} = \frac{\log(\frac{(a-b+\sqrt{ad})(b+\sqrt{ac})}{(-b+\sqrt{ac})(-a+b+\sqrt{ad})})}{6\sqrt{a}} + \frac{\log(\frac{(-b+c+\sqrt{cd})(b+\sqrt{ac})}{(-b+\sqrt{ac})(b-c+\sqrt{cd})})}{6\sqrt{c}} + \frac{\log(\frac{(a-b+\sqrt{ad})(-b+c+\sqrt{cd})}{(-a+b+\sqrt{ad})(b-c+\sqrt{cd})})}{6\sqrt{d}} \tag{4.18}$$

where $a = (\mathbf{r}_3 - \mathbf{r}_1)\cdot(\mathbf{r}_3 - \mathbf{r}_1)$, $b = (\mathbf{r}_3 - \mathbf{r}_1)\cdot(\mathbf{r}_3 - \mathbf{r}_2)$, $c = (\mathbf{r}_3 - \mathbf{r}_2)\cdot(\mathbf{r}_3 - \mathbf{r}_2)$, $d = a - 2b + c$. It may be noted that $\mathbf{r}_1$, $\mathbf{r}_2$ and $\mathbf{r}_3$ are the node points of the triangle.

4.2.4.2 Radiation pattern calculation

Radiation pattern can be evaluated using the dipole model based on the solution of moment as available in [72]. For the sake of accuracy, a more attractive technique such as analytical method [68] is used to calculate the radiation pattern. The related mathematical details are given below.

Generally, far field pattern can be evaluated using the surface electric and magnetic currents as given below.

$$\vec{E}^{far} = \frac{-jk\eta e^{-jkr}}{4\pi r}\iint_{S'}\left[\vec{J}_S - \left(\vec{J}_S\cdot\hat{a}_r\right)\hat{a}_r + \frac{1}{\eta}\vec{M}_S\times\hat{a}_r\right]e^{jk\vec{r}'\cdot\hat{a}_r}\,d\vec{S}'$$

Here, $\vec{J}_S = 0$ and $\vec{M}_S$ is doubled. Thus, using equation 4.2 for RWG function, we can write:

$$\vec{E}^{far} = \frac{-jke^{-jkr}}{2\pi r}\iint_{S'}\left[\vec{M}_S\times\hat{a}_r\right]e^{jkr'\cdot\hat{a}_r}\,d\vec{S}' = \frac{jk\eta e^{-jkr}}{2\pi r}\sum_{m=1}^{M} V_m\hat{a}_r\times\iint_{T_m'^{\pm}}\vec{f}_m^{1}(r')e^{jk\vec{r}'\cdot\hat{a}_r}\,d\vec{A}_m'^{\pm} \tag{4.19}$$

Calculation of integration for T_+^n and T_-^n triangles are same. So, the integration part of T_+^n is considered

in this section. Let T_+^n triangle has the nodes $\mathbf{r}_1,\ \mathbf{r}_2$ and $\mathbf{r}_3$ and free vertex is $\mathbf{r}_1$ for n^{th} RWG function. Several variables are used for this calculation which are given as follows: $\mathbf{e}_1 = \mathbf{r}_2 - \mathbf{r}_1$, $\mathbf{e}_3 = \mathbf{r}_3 - \mathbf{r}_1$, $o_1 = k(\mathbf{r}_1 \cdot \hat{a}_r)$, $o_2 = k(\mathbf{e}_1 \cdot \hat{a}_r)$, $o_3 = k(\mathbf{e}_3 \cdot \hat{a}_r)$

$$I(o_1,o_2,o_3) = \iint_{T_m'^+} \vec{f}_m^1(r') e^{jk\vec{r}'\cdot\hat{a}_r}\, d\vec{A}_m'^+ = \frac{l_m}{2A_m^+} \iint_{T_m'^+} (\mathbf{r}' - \mathbf{r}_1) e^{jk\vec{r}'\cdot\hat{a}_r}\, d\vec{A}_m'^+$$
$$= l_m \int_0^1 \int_0^{1-\alpha} (\alpha\mathbf{e}_1 + \beta\mathbf{e}_3) e^{j(o_1+o_2\alpha+o_3\beta)} d\beta\ d\alpha$$

The solution for the above equation is given below:

(a) When $o_2 \neq 0$, $o_3 \neq 0$ and $o_2 \neq o_3$

$$I(o_1,o_2,o_3) = -\frac{jl_m e^{jo_1}}{o_3}[e^{jo_2}(\frac{1-o_2+o_3}{(o_2-o_3)^2)} + \frac{jo_2-1}{o_2^2}) - \frac{e^{jo_3}}{(o_2-o_3)^2} + \frac{1}{o_2^2}]\mathbf{e}_1$$
$$-\frac{jl_m e^{jo_1}}{o_2}[e^{jo_3}(\frac{1-o_3+o_2}{(o_3-o_2)^2)} + \frac{jo_3-1}{o_3^2}) - \frac{e^{jo_2}}{(o_3-o_2)^2} + \frac{1}{o_3^2}]\mathbf{e}_3$$

(b) When $\mathbf{e}_1$ is perpendicular to $\hat{a}_r$ ($o_2 = 0$).

$$I(o_1,o_2,o_3) = jl_m e^{jo_1}[\frac{-1-jo_3}{o_3^3} + \frac{1}{2o_3} + \frac{e^{jo_3}}{o_3^3}]\mathbf{e}_1 + jl_m e^{jo_1}[e^{jo_3}(\frac{jo_3-2}{o_3^3}) + \frac{2}{o_3^3} + \frac{j}{o_3^2}]\mathbf{e}_3$$

(c) When $\mathbf{e}_3$ is perpendicular to $\hat{a}_r$ ($o_3 = 0$).

$$I(o_1,o_2,o_3) = jl_m e^{jo_1}[e^{jo_2}(\frac{jo_2-2}{o_2^3}) + \frac{2}{o_2^3} + \frac{j}{o_2^2}]\mathbf{e}_1 + jl_m e^{jo_1}[\frac{-1-jo_2}{o_2^3} + \frac{1}{2o_2} + \frac{e^{jo_2}}{o_2^3}]\mathbf{e}_3$$

(d) When $\hat{a}_r$ is perpendicular to triangle ($o_2 = o_3 = 0$).

$$I(o_1,o_2,o_3) = \frac{l_m e^{jo_1}}{6}(\mathbf{e}_1 + \mathbf{e}_3)$$

(e) When ($o_2 = o_3 = o \neq 0$).

$$I(o_1,o_2,o_3) = jl_m e^{jo_1}[e^{jo}(\frac{1}{o^3} - \frac{1}{2o} - \frac{j}{o^2}) - \frac{1}{o^3}](\mathbf{e}_1 + \mathbf{e}_3)$$

It may be noted that the calculation of $I(o_1,o_2,o_3)$ value presented here is in rectangular coordinate system. The far field pattern can be evaluated using equation (4.19) after substituting $I(o_1,o_2,o_3)$

transformed to spherical coordinate system.

4.2.5 Results for infinite ground plane

The codes are developed in Matlab to investigate the radiation patterns and reflection coefficient of rectangular waveguide mounted on an infinite ground plane. A stepped symmetric rectangular waveguide is considered with X-axis dimensions [22.86, 29.86, 36.86, 43.86] mm, Y-axis dimensions [10.16, 17.16, 24.16, 31.16] mm and Z-axis dimensions [10, 10, 10, 20] mm respectively.

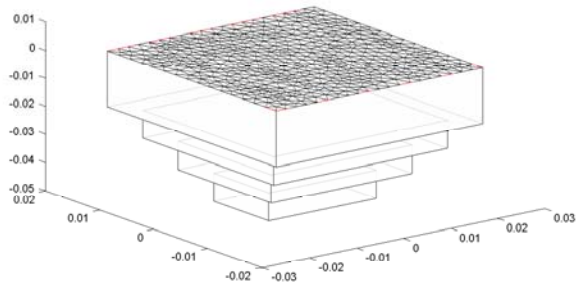

Figure 4.4: Horn structure with 2-D meshing on common aperture using matlab.

The TE_{10} dominant mode is applied at the feed terminal. The results of investigation are given in Figure 4.5, 4.6 and 4.7. In this investigation, total unknown basis functions and total number of triangles are 1372 and 938, respectively. Results are compared with HFSS-15 and close match is obtained. It may be noted that the computed H-plane pattern by MoM technique in Figure 4.6 shows a null for $\theta = \pm\frac{\pi}{2}$ and around these angles, the pattern differs from the patterns obtained using simulated HFSS. This is because, only the equivalent magnetic surface current has been considered at the aperture and for this reason, the far-field radiated electric field E_ϕ component varies as $\cos(\theta)$.

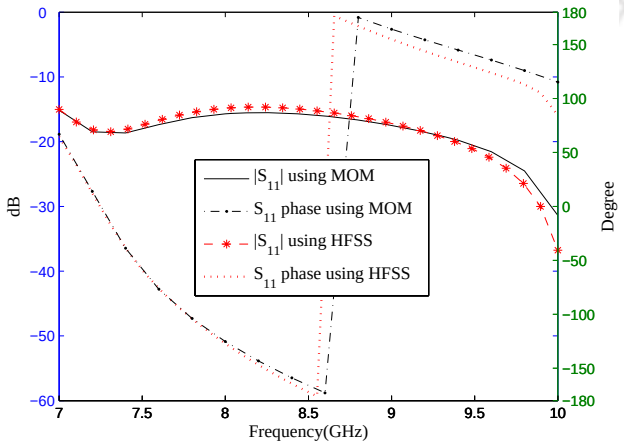

Figure 4.5: Reflection coefficient of horn with infinite ground.

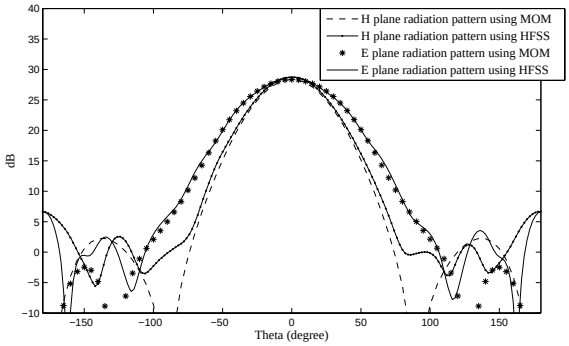

Figure 4.6: E and H plane radiation patterns of horn with infinite ground (8.4 GHz).

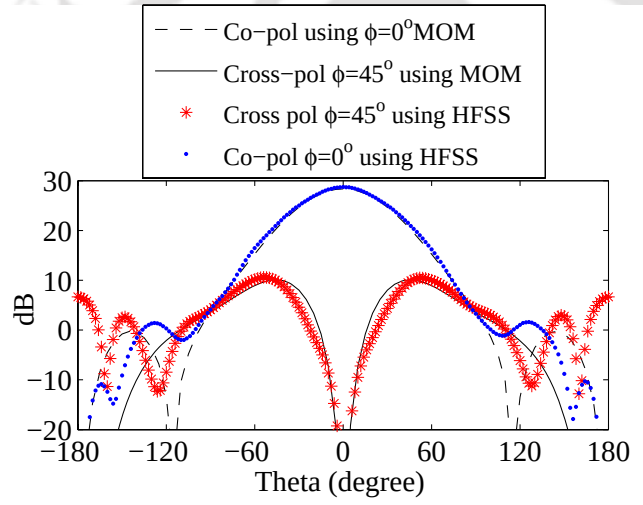

Figure 4.7: Co and Cross-polar patterns of horn with infinite ground (8.4 GHz).

4.3 Using the direct Kirchhoff-Huygen's principle for open-ended waveguide

The entire structure of horn is subdivided into two region viz. the outer region and inner region. Both regions are separated by a perfect conductor surface S_a as shown in Figure 4.8. $\vec{H}_a$ and $\vec{E}_a$ represent the inner magnetic and electric fields, respectively. $\vec{H}_b$ and $\vec{E}_b$ are the outer magnetic and electric fields. S_b is the outer surface.

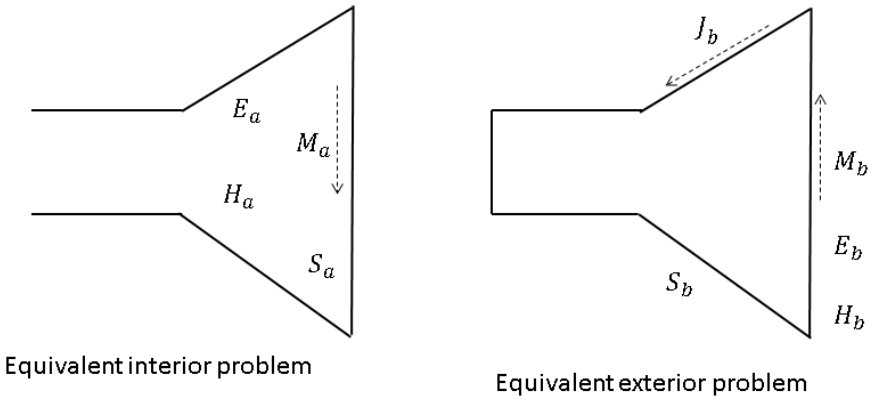

Figure 4.8: Equivalent source model of horn.

4.3.0.1 Inner region solution

The continuity of tangential magnetic field is enforced as:

$$\vec{H}_a = \vec{H}_b \qquad \text{at common aperture } S_a \tag{4.20}$$

and in case of magnetic current, we can write it as:

$$\vec{M}_b(r) = -\vec{M}_a(r) = -\{\vec{E}_a \times (-\hat{u}_z)\} = -\hat{u}_z \times \vec{E}_a\Big|_{z=0} \tag{4.21}$$

Unknown electric and magnetic current can be approximated on the outer surface of the horn as:

$$\vec{J}_b(r) = \sum_{s=1}^{S} I_s \vec{J}_s(r) \qquad \vec{M}_b(r) = \eta \sum_{m=1}^{M} V_m \vec{M}_m(r) \tag{4.22}$$

If a_n and b_n are the forward and backward mode coefficients of the interior field, we can represent the $\vec{E}_a$ and $\vec{H}_a$ as:

$$\vec{E}_a = \sum_{n=1}^{N} a_n e^{-\gamma_n z}\mathbf{e}_n + \sum_{n=1}^{N} b_n e^{\gamma_n z}\mathbf{e}_n = \sum_{n=1}^{N} a_n e^{-\gamma_n z}\mathbf{e}_n - \sum_{n=1}^{N} a_n e^{\gamma_n z}\mathbf{e}_n + \sum_{n=1}^{N} d_n e^{\gamma_n z}\mathbf{e}_n \tag{4.23}$$

$$\vec{H}_a = \sum_{n=1}^{N} a_n Y_n e^{-\gamma_n z}\mathbf{h}_n - \sum_{n=1}^{N} b_n Y_n e^{\gamma_n z}\mathbf{h}_n = \sum_{n=1}^{N} a_n Y_n e^{-\gamma_n z}\mathbf{h}_n + \sum_{n=1}^{N} a_n Y_n e^{\gamma_n z}\mathbf{h}_n - \sum_{n=1}^{N} d_n Y_n e^{\gamma_n z}\mathbf{h}_n \tag{4.24}$$

where

$$[d_n] = [b_n] + [a_n] \tag{4.25}$$

$[d_n]$ represents the equivalent fictitious magnetic source of $\vec{M}_b(r)$ for $z = 0$. From the equations (4.21), (4.23) and (4.25), we can write

$$\vec{M}_b(r) = -\sum_{n=1}^{N} d_n \mathbf{h}_n \tag{4.26}$$

By taking the inner product of h_n on both sides, we can formulate the equation as:

$$[d_n]_{N\times 1} = -\eta \Big\langle \mathbf{h}_n, \vec{M}_m(r) \Big\rangle_{N\times M} [V_m]_{M\times 1} = -\eta \mathbf{A}_{N\times M} [V_m]_{M\times 1} \tag{4.27}$$

If we represent the $\vec{H}_b(r)$ in source term from the equation (4.20), (4.24) and (4.22), we can write

$$2\sum_{n=1}^{N} a_n Y_n \mathbf{h}_n - \sum_{n=1}^{N} d_n Y_n \mathbf{h}_n = -\hat{n} \times \vec{J}_b(r) = -\sum_{s=1}^{S} I_s \hat{n} \times \vec{J}_s(r) \tag{4.28}$$

Equation (4.28) can be written by taking the inner product of considered testing function $\vec{w}_p(r)$ as

$$2\mathbf{B}_{M\times N} [Y_n]_{N\times N} [a_n]_{N\times 1} = \mathbf{B}_{M\times N} [Y_n]_{N\times N} [d_n]_{N\times 1} + \mathbf{C}_{M\times S} [I_s]_{S\times 1} \tag{4.29}$$

where value of $\mathbf{B}$ and $\mathbf{C}$ are

$$\mathbf{B} = \langle \vec{w}_p(r), \mathbf{h}_n \rangle_{M\times N} \qquad \mathbf{C} = \Big\langle \vec{w}_p(r), -\hat{n} \times \vec{J}_s(r) \Big\rangle_{M\times S} \tag{4.30}$$

Putting the value of $[d_n]$ from equation (4.27) into equation (4.30), we can write

$$2\mathbf{B}_{M\times N} [Y_n]_{N\times N} [a_n]_{N\times 1} = -\eta \mathbf{B}_{M\times N} [Y_n]_{N\times N} \mathbf{A}_{N\times M} [V_m]_{M\times 1} + \mathbf{C}_{M\times S} [I_s]_{S\times 1} \tag{4.31}$$

4.3.0.2 Outer region solution

The outer region model is based on Kirchhoff-Huygen's principle. Outer field and source can be written using EFIE and MFIE as

$$\vec{M}_b(r) = \begin{cases} -\hat{n} \times \vec{E}_b(r) & \text{on } S_a \\ 0 & \text{outside } S_a \end{cases} \tag{4.32}$$

$$\vec{J}_b(r) = \hat{n} \times \vec{H}_b(r) \qquad \text{on } S_a \text{ and } S_b$$

$$\vec{E}_b(r) = -j\frac{\eta}{k}\left[k^2 \iint_{S'} \vec{J}_b(r')G(r,r')d\vec{s}' + \nabla \iint_{S'} \nabla' \cdot \vec{J}_b(r')G(r,r')d\vec{s}'\right] - \nabla \times \iint_{S'} \vec{M}_b(r')G(r,r')d\vec{s}' \tag{4.33}$$

$$\vec{H}_b(r) = -j\frac{1}{\eta k}\left[k^2 \iint_{S'} \vec{M}_b(r')G(r,r')ds' + \nabla \iint_{S'} \nabla' \cdot \vec{M}_b(r')G(r,r')d\vec{s}'\right] + \nabla \times \iint_{S'} \vec{J}_b(r')G(r,r')d\vec{s}' \tag{4.34}$$

where the Green function is equal to $G(r,r') = \frac{e^{-jk|\mathbf{r}-\mathbf{r}'|}}{4\pi|\mathbf{r}-\mathbf{r}'|}$. The Cauchy principal value for EFIE and MFIE can be presented as

$$\nabla \times \iint_{S'} \vec{M}_b(r')G(r,r')d\vec{s}' = -\frac{1}{2}\hat{n} \times \vec{M}_b(r) - \iint_{S'} \vec{M}_b(r') \times \nabla G(r,r')d\vec{s}' \tag{4.35}$$

$$\nabla \times \iint_{S'} J_b(r')G(r,r')d\vec{s}' = -\frac{1}{2}\hat{n} \times \vec{J}_b(r) - \iint_{S'} \vec{J}_b(r') \times \nabla G(r,r')d\vec{s}' \tag{4.36}$$

where $\nabla G(r,r') = -\hat{R}\frac{1+j\beta R}{R^3}G(r,r')$ and $\hat{R} = r - r'$. Using (4.32), (4.33) and (4.35), EFIE equation can be constructed as:

$$\frac{1}{2}\hat{n}\times\vec{M}_b(r) = -j\frac{\eta}{\beta}\left[\beta^2 \iint_{S'} \vec{J}_b(r')G(r,r')d\vec{s}' + \nabla \iint_{S'} \nabla' \cdot \vec{J}_b(r')G(r,r')d\vec{s}'\right] + \iint_{S'} \vec{M}_b(r') \times \nabla G(r,r')d\vec{s}' \tag{4.37}$$

Similarly, MFIE equation can be written using (4.32), (4.34) and (4.36) as:

$$-\frac{1}{2}\hat{n}\times\vec{J}_b(r) = -j\frac{1}{\eta\beta}\left[\beta^2 \iint_{S'} \vec{M}_b(r')G(r,r')d\vec{s}' + \nabla \iint_{S'} \nabla' \cdot \vec{M}_b(r')G(r,r')d\vec{s}'\right] - \iint_{S'} \vec{J}_b(r') \times \nabla G(r,r')d\vec{s}' \tag{4.38}$$

The EFIE equation (4.37) is solved by taking the inner product using test function $\vec{f}_q(r)$ as given below:

$$[I_s]_{S\times 1} = \left[T^J_{S\times S}\right]^{-1}\left[D^M_{S\times M} - S^M_{S\times M}\right][V_m]_{M\times 1} \tag{4.39}$$

where

$$\mathbf{D}^M_{S\times M} = \frac{\eta}{2}\Big\langle \vec{f}_q(r), \hat{n}\times\vec{M}_m(r)\Big\rangle_{S\times M} \tag{4.40}$$

$$\mathbf{T}^J_{S\times S} = -j\frac{\eta}{\beta}\left[\beta^2 \iint\limits_s \vec{f}_q(r)\cdot \iint\limits_{S'} \vec{J}_s(r')G(r,r')ds'ds - \iint\limits_S \nabla\cdot\vec{f}_q(r)\iint\limits_{S'}\nabla'\cdot\vec{J}_s(r')G(r,r')d\vec{s}'d\vec{s}\right]_{S\times S}$$

$$\mathbf{S}^M_{S\times M} = \eta\left[\iint\limits_S \vec{f}_q(r)\cdot\iint\limits_{S'}\vec{M}_m(r')\times\nabla G(r,r')d\vec{s}'\right]_{S\times M} \tag{4.41}$$

Similarly, we can write for the MFIE equation using the testing function $\vec{f}_q(r)$ as:

$$[I_s]_{S\times 1} = \left[D^J_{S\times S} - S^J_{S\times S}\right]^{-1}[T^M_{S\times M}][V_m]_{M\times 1} \tag{4.42}$$

where

$$\mathbf{D}^J_{S\times S} = -\frac{1}{2}\Big\langle \vec{f}_q(r), \hat{n}\times\vec{J}_s(r)\Big\rangle_{S\times S} \tag{4.43}$$

$$\mathbf{T}^M_{S\times M} = -j\frac{1}{\beta}\left[\beta^2\iint\limits_s \vec{f}_q(r)\cdot\iint\limits_{S'}\vec{M}_j(r')G(r,r')d\vec{s}'d\vec{s} - \iint\limits_S\nabla\cdot\vec{f}_q(r)\iint\limits_{S'}\nabla'\cdot\vec{M}_j(r')G(r,r')d\vec{s}'d\vec{s}\right]_{S\times M}$$

$$\mathbf{S}^J_{S\times S} = -\left[\iint\limits_S \vec{f}_q(r)\cdot\iint\limits_{S'}\vec{J}_s(r')\times\nabla G(r,r')d\vec{s}'d\vec{s}\right]_{S\times S} \tag{4.44}$$

4.3.1 Calculation of scattering parameter and unknown coefficients (V_m, I_s) of electric and magnetic current at the aperture

Calculation of scattering parameter at horn aperture depends on the evaluated admittance values of inner ($\mathbf{Y}_{aa}$) and outer ($\mathbf{Y}_{bb}$). Using the equations (4.31), (4.39) and (4.42), we can easily derive the equation as:

$$[Y_{aa} + Y_{bb}]_{M\times M}[V_{mn}]_{M\times N} = I^{inc}_{M\times N} \tag{4.45}$$

where inner admittance Y_{aa} can be written as:

$$\mathbf{Y}_{aa} = -\eta \mathbf{B}_{M\times N} \left[Y_n\right]_{N\times N} \mathbf{A}_{N\times M} \tag{4.46}$$

For EFIE, the outer admittance Y_{bb} will be

$$\mathbf{Y}_{bb} = \mathbf{C}_{M\times S}\left[T^J_{S\times S}\right]^{-1}\left[D^M_{S\times M} - S^M_{S\times M}\right] \tag{4.47}$$

For MFIE, the outer admittance Y_{bb} will be

$$\mathbf{Y}_{bb} = \mathbf{C}_{M\times S}\left[D^J_{S\times S} - S^J_{S\times S}\right]^{-1}[T^M_{S\times M}] \tag{4.48}$$

and

$$\mathbf{I}^{inc}_{M\times N} = 2\mathbf{B}_{M\times N}\left[Y_n\right]_{N\times N} \tag{4.49}$$

Forward and backward coefficient ratios can be easily calculated from the equations (4.45), (4.25) and (4.27) as

$$[s^{11}_{ij}] = -\eta A_{N\times M}[V_{mn}]_{M\times N} - \mathbf{I}_{N\times N} \tag{4.50}$$

and modal scatter parameter (S^A_{11}) is evaluated by the equations (4.16) and (4.50).

After the evaluation of scattering parameter at the aperture, the equivalent scattering parameter using GSP technique is evaluated for the full system of horn using the model as specified in Section 4.2.3.2. The unknown coefficients of magnetic currents are estimated for the multi-mode or single mode excitation of horn using the equations (4.15) and (4.17). Once the magnetic current coefficients are known, electric current coefficients are calculated using equation (4.39) for EFIE and equation (4.42) for MFIE, respectively.

4.3.2 Implementation and choice of the set of orthogonal functions

Delaunay triangulation and two kinds of RWG function are used to model the finite ground plane horn. It may be noted that two orthogonal basis functions are used to approximate the currents ($\vec{J}_s(r),\ \vec{M}_s(r)$) and two orthogonal testing functions ($\vec{w}_p(r),\ \vec{f}_q(r)$) are required to model it. Proper choice of RWG functions for $\vec{J}_s(r),\ \vec{M}_m(r),\ \vec{w}_p(r)$ and $\vec{f}_q(r)$ lead to the solution for this model.

(a) Choice of orthogonal functions for EFIE solution:

- For the sake of accuracy of the solution of equation (4.37), the basis function of $\vec{J_s}(r)$ and testing function $\vec{f_q}(r)$ should be the type-I of RWG function as defined $\vec{f_n^1}(r)$. Otherwise, solution of equation (4.37) will behave similar to the solution obtained for the pulse type orthogonal function.
- To efficiently generate **A** and **B** matrix, we can make the relation as $\mathbf{A} = \mathbf{B}^T$ (T: transpose) by choosing the same kind of orthogonal function for $\vec{M}_m(r)$ and $\vec{w}_p(r)$. On the other hand, the choice of same kind of orthogonal function for $\vec{M}_m(r)$ and $\vec{w}_p(r)$ can also lead to any one type of inner product of RWG functions for generating the **C** and $\mathbf{D}^M_{S\times M}$ matrix. Specifically, such inner products will lead to self ($\langle \vec{f_n^1} \cdot \vec{f_n^1} \rangle$, $\langle \vec{f_n^2} \cdot \vec{f_n^2} \rangle$) or cross ($\langle \vec{f_n^1} \cdot \vec{f_n^2} \rangle$). $\vec{M}_m(r)$ and $\vec{w}_p(r)$ are taken as a type-II RWG function $\vec{f_n^2}(r)$ to develop the code.

(b) Choice of orthogonal functions for MFIE solution:

- Similar reason is also applicable for the solution of MFIE equation (4.42), $\vec{M}_m(r)$ and $\vec{f_q}(r)$ are to be $\vec{f_n^1}(r)$.
- It is observed through the study of developed code that $[D^J_{S\times S} - S^J_{S\times S}]^{-1}$ calculation suffers due to singularity for any kind of choice of RWG functions of $\vec{J_s}(r)$ and $\vec{w}_p(r)$.

4.3.2.1 Generation of matrices and radiation pattern calculation

As discussed earlier, only EFIE model is developed to observe the performance of horn having a finite ground plane. Several matrices such as **A**, **B**, **C**, $\mathbf{T}^J$, $\mathbf{D}^M$ and $\mathbf{S}^M$ are mainly used for this model.

- **A** and **B** matrices are generated using seven points Gaussian quadrature integration.
- Four points for observation and seven points for source using Gaussian quadrature integration are used to generate the $\mathbf{T}^J$ and $\mathbf{S}^M$ matrices.
- The treatment for singularity of self coupling of $\mathbf{T}^J$ matrix is taken care of as specified in Section 4.2.4.1.
- **C** and $\mathbf{D}_m$ matrixes are generated using analytical closed form expressions as given in equations (4.51) and (4.52).

Inner product for same RWG functions are given as:

$$\left\langle \vec{f}_n^1(r), \vec{f}_m^1(r) \right\rangle = \left\langle \vec{f}_n^2(r), \vec{f}_m^2(r) \right\rangle = \frac{S_n^{\pm} S_m^{\pm} l_n l_m}{4A_n^2} \iint\limits_{T_p} (\vec{r} - \vec{r}_{f_n}) \cdot (\vec{r} - \vec{r}_{f_m}) d\vec{s}$$
$$= \frac{S_n^{\pm} S_m^{\pm} l_n l_m}{4A_n} \left[\vec{r}_c \cdot \vec{r}_c + \frac{(a+c-b)}{18} - \vec{r}_c \cdot (\vec{r}_{f_n} + \vec{r}_{f_m}) + \vec{r}_{f_n} \cdot \vec{r}_{f_m} \right] \quad (4.51)$$

Cross product between dissimilar RWG functions are given as:

$$\left\langle \vec{f}_n^1(r), \vec{f}_m^2(r) \right\rangle = \frac{S_n^{\pm} S_m^{\pm} l_n l_m}{4{A_n}^2} \vec{n}_m \cdot [\vec{r}_c \times (\vec{r}_{f_m} - \vec{r}_{f_n}) + \vec{r}_{f_m} \times \vec{r}_{f_n}] \quad (4.52)$$

where A_n and $\vec{r}_c$ are area and center point of the triangle. $\{S_n^{\pm},\ S_m^{\pm}\},\ \{l_n,\ l_m\}and\{\vec{r}_{f_n},\ \vec{r}_{f_m}\}$ present the sign, common edge and free vertex of n^{th} and m^{th} RWG functions.

The far field pattern of horn is calculated using analytical method as mentioned in Section 4.2.4.2. According to our model, for the solution of EFIE as specified, $\vec{J}_s(r)$ and $\vec{M}_m(r)$ are type-I and type-II RWG orthogonal functions. Far field pattern is calculated based on the predicted values of I_s and V_m coefficients of electric and magnetic currents.

$$\vec{E}^{far} = \frac{jk\eta e^{-jkr}}{4\pi r} \iint_{S'} \left[\hat{a}_r \times \hat{a}_r \times \vec{J}_S + \frac{1}{\eta} \hat{a}_r \times \vec{M}_S \right] e^{jk\vec{r}' \cdot \hat{a}_r} \, d\vec{S}'$$

Using $J_s(r)$ and $M_m(r)$ in terms of expansion coefficient of RWG function, we can easily construct as

$$\vec{E}^{far} = \frac{jk\eta e^{-jkr}}{4\pi r} \left[\sum_{s=1}^{S} I_s \widehat{a}_r \times \widehat{a}_r \times \int\limits_{T_s^{\pm}} \vec{f}_s^1(r') e^{jk\vec{r}' \cdot \widehat{a}_r} d\vec{A}_s'^{\pm} + \sum_{m=1}^{M} V_m \widehat{a}_r \times \widehat{n} \times \int\limits_{T_m'^{\pm}} \vec{f}_m^1(r') e^{jk\vec{r}' \cdot \widehat{a}_r} d\vec{A}_m'^{\pm} \right]$$

Closed form expression for the integration $I(o, o_1, o_2) = \int\limits_{T_n'^{\pm}} \vec{f}_n^1(r') e^{jk\vec{r}' \cdot \widehat{a}_r} d\vec{A}_n'^{\pm}$ as already derived in Section 4.2.4.2, is used to calculate the far field pattern.

4.3.3 Results for finite ground

To investigate the performance of the developed code for aperture problem of horn having finite ground plane, the same structure as specified in Section 4.2.5 is considered and mesh structure generated using MATLAB is shown in Figure 4.9. 2168 no of triangles, 3168 no of basis functions for electric current and 489 no of basis functions for magnetic current are used for solution of the considered structure. The performance of this code is evaluated using the radiation pattern and reflection coefficient as in Figure 4.10, 4.11 and 4.12. Results are also compared with HFSS results and close matches are obtained in this study.

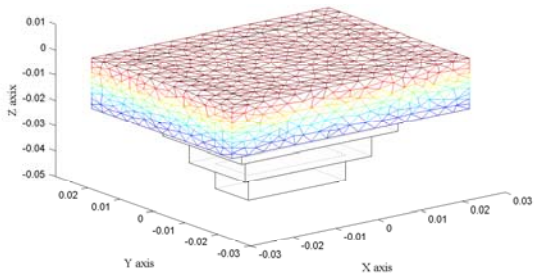

Figure 4.9: Horn structure with 2-D meshing using matlab.

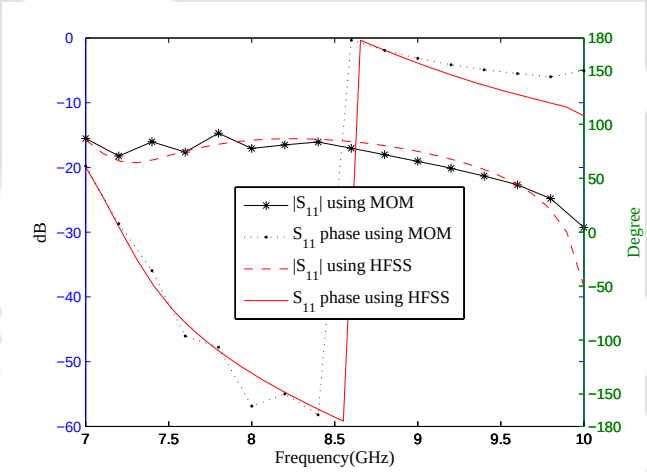

Figure 4.10: Reflection coefficient of horn with finite ground.

4.4 Analytical far field pattern calculation of multi-mode horn (Chu's model)

To derive the multi-mode feed pattern of open ended waveguide, we have considered the equivalent signal flow graph of the full feed structure which is shown in Figure 4.2. Exterior electric current (J_S) and magnetic current (M_S) are considered as linear combination orthogonal functions with unknown coefficients for every elements of the mesh as used in the solution for MoM technique as presented in

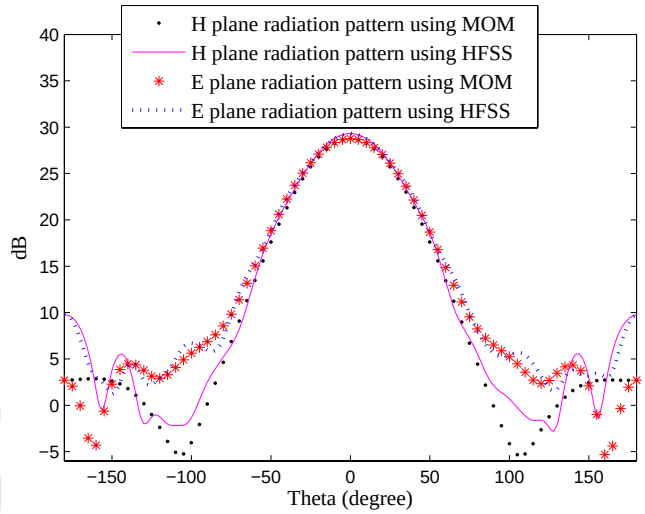

Figure 4.11: E and H plane radiation patterns of horn with finite ground (8.4 GHz).

Figure 4.8. $[S_{11}]$, $[S_{12}]$, $[S_{21}]$, $[S_{22}]$ are the equivalent scattering parameters of interior junction. $[S_{11}^A]$ is equivalent aperture scattering parameter of open ended waveguide. $[V_0^+]$ and $[V_0^-]$ represent the forward and backward mode coefficients at the excited port of the horn. $[V_A^+]$ and $[V_A^-]$ present the forward and backward mode coefficients at the aperture junction $Z = 0^-$.

In this context, using the signal flow graph of Figure 4.2, the solution of the forward mode coefficient at the aperture can be written as:

$$[V_A^+] = [I - S_{22}S_{11}^A]^{-1}[S_{21}][V_0^+] \tag{4.53}$$

and the backward coefficient at the aperture as:

$$[V_A^-] = [S_{11}^A][V_A^+]. \tag{4.54}$$

To simplify the model, we can replace of the exterior $\vec{J}_S$ and $\vec{M}_S$ in terms of equivalent interior electric and magnetic sources as $\vec{J}_{S_A}$ and $\vec{M}_{S_A}$ at the aperture $Z = 0^-$ which can be represented as equivalent radiation sources of horn. Here

$$\vec{M}_{S_A} = [V_A^+ + V_A^-][\sqrt{Z_A}][-\hat{n} \times \vec{E}_A] \tag{4.55}$$

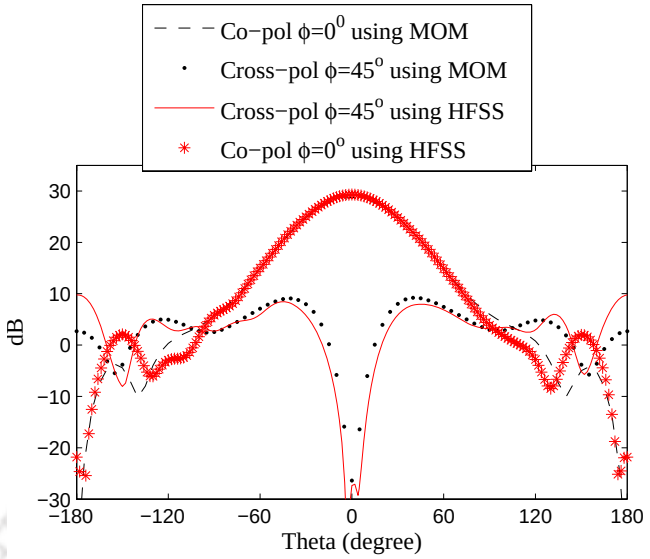

Figure 4.12: Co and Cross-polar patterns of horn with finite ground (8.4 GHz).

and

$$\vec{J}_{S_A} = [\mathrm{V}_A^+ - \mathrm{V}_A^-][\frac{1}{\sqrt{Z_A}}][\hat{n} \times \vec{H}_A]. \tag{4.56}$$

$[\mathrm{E}_A]$ and $[\mathrm{H}_A]$ represent the electric and magnetic fields solution of Helmholtz equation at interior of the aperture and $\hat{n}$ presents as outer normal of the aperture surface. Z_A represents the mode impedance.

It may be noted that $\vec{M}_S$, $\vec{M}_{S_A}$ and $\vec{S}_A$ present on the common aperture enclosed by PEC surface. But, in case of electric current (J_S) represents the entire exterior surface of the horn.

The far field pattern, which is defined in [60] in terms of $\vec{J}_{S_A}$ and $\vec{M}_{S_A}$, can be written using the equation (4.55) and (4.56) as

$$E_\theta = -\frac{jke^{-jKR}}{4\pi R}\sum_{i=1}^{n}((v_{A_i}^+ + v_{A_i}^-)\sqrt{z_{A_i}} + \cos\theta(v_{A_i}^+ - v_{A_i}^-)\frac{\eta}{\sqrt{z_{A_i}}})\iint\limits_{S'}(e_{A_i}^{x'}\cos\phi + e_{A_i}^{y'}\sin\phi)e^{jk\vec{r}'\cdot\hat{a}_r}\mathrm{d}\vec{S}' \tag{4.57}$$

$$E_\phi = \frac{jke^{-jkR}}{4\pi R}\sum_{i=1}^{n}(\cos\theta(v_{A_i}^+ + v_{A_i}^-)\sqrt{z_{A_i}} + (v_{A_i}^+ - v_{A_i}^-)\frac{\eta}{\sqrt{z_{A_i}}})\iint\limits_{S'}(e_{A_i}^{x'}\sin\phi - e_{A_i}^{y'}\cos\phi)e^{jk\vec{r}'\cdot\hat{a}_r}\mathrm{d}\vec{S}'. \tag{4.58}$$

where R, θ and ϕ are the coordinates of observation point of far field as mentioned earlier and r', $\hat{a}_r$, S', k and η are the position vector on the aperture, unit vector at the far field location, effective radiated surface of horn, wave number and free space wave impedance, respectively. Here, n represents the numbers of active mode and $e_{A_i}^{x'}$ and $e_{A_i}^{y'}$ represent x polarized and y polarized electric fields of

the i^{th} mode.

It is observed in the equations (4.57) and (4.58) that electric field and magnetic field coefficients $(v_{A_i}^+ + v_{A_i}^-, v_{A_i}^+ - v_{A_i}^-)$ have an affect on the far field. In order to simplify the equations (4.57) and (4.58), it is considered that the aperture is perfectly matched. It means, coupling and reflection of different modes are negligible at the aperture. From the equations (4.53) and (4.54), we can write $[\mathrm{V}_A^+] \simeq [\mathrm{S}_{21}][\mathrm{V}_0^+]$ and $[\mathrm{V}_A^-] \simeq [0]$. Consequently, knowledge of S_{21} is sufficient to estimate the far field pattern of multi-mode feed antenna. From our study it is observed that, large aperture horn supports such conditions, however it is different in case of small aperture horn. To normalize the power at the aperture, we can write as $\frac{1}{2}\iint\limits_{S'} Re\{\vec{J}_{S_A} \cdot \vec{M}_{S_A}^{\star}\}\mathrm{d}\vec{S'} = 1$. Also, individual modes are orthogonal to each other, so scaler potential (ψ_n) at the interior of the aperture can be written as $\frac{1}{2}k_c^2 \iint\limits_{S'} \psi_n^2 \mathrm{d}\vec{S'} = 1$, where k_c is cut-off wave number of different modes.

4.5 Conclusion

A hybrid technique using MM and MoM techniques has been presented for analysis of horn antennas assuming that the ground plane at the aperture is of infinite extent. Also, the study of horns having finite ground plane is performed. The performance of developed numerical techniques have been investigated and compared with the results obtained through HFSS-15. Close match has been obtained for return loss characteristics and front side radiation patterns. However, the prediction of backside radiation patterns does not match with the HFSS results. Since less amount of computation is involved in the proposed modeling, it provides faster solution. The developed methodology may be used in modeling the pattern of feed horns which illuminate a reflector.

भारतीय प्रौद्योगिकी संस्थान गुवाहाटी
Indian Institute of Technology Guwahati

5

An Analytical/Semi-analytical and Proposed Hybrid Technique for Reflector-Feed Model

Contents

In this chapter, the far field pattern calculation of an offset reflector antenna using physical optics (PO) is reported. A brief discussion on particle swarm optimization technique (PSO) is presented as PSO has been used as a tool for optimization. Matched feed design using this optimization technique along with analytical or semi-analytical model of feed and reflector is also presented. For the rest of this chapter, the performance of our proposed hybrid technique comprising of MM, FEM, MoM and PO is evaluated for a proposed new kind of circular matched feed structure. The matched feed design involves TE_{11}^1, TM_{11}^1 and TE_{21}^1 modes as the operating modes.

5.1 Reflector radiation pattern calculation using PO

As discussed in Section 1.2, reflector pattern is calculated using PO which is quite efficient. Usually the main difficulty in applying this method is the approximation of the current density over the surface of the scatterer. The foundation of PO is based on the assumption that the induced current on the reflector surface for a perfect conductor is given by

$$\vec{J}_{S_R} = \begin{cases} 2\hat{n}_R \times \vec{H}_{i_R}(\hat{i}_R,\ \hat{j}_R,\ \hat{k}_R) & \text{illuminated region} \\ 0 & \text{otherwise} \end{cases} \tag{5.1}$$

where $\hat{n}_R$ and $\vec{H}_{i_R}(\hat{i}_R,\ \hat{j}_R,\ \hat{k}_R)$ are the normal unit vector of the reflector surface and the incident magnetic field from the feed, respectively. Basically, $\vec{n}_R$ and $\vec{H}_{i_R}(\hat{i}_R,\ \hat{j}_R,\ \hat{k}_R)$ are calculated with respect to coordinate system used for calculation of the radiated field. The details of coordinate system are specified in Figure 1.1. It may be emphasized that the development of such PO based frame work itself is quite complicated due the involvement of different coordinate systems used for the feed radiation, reflector surface and reflector radiated field as well as associated transformation of field quantities which are properly addressed here. $\hat{n}_R$ can be calculated as

$$\hat{n}_R = -\frac{\nabla F_R}{|\nabla F_R|} = \frac{-(x_R + x_0)\hat{i}_R - y_R\hat{j}_R + 2F\hat{k}_R}{\sqrt{(x_R + x_0)^2 + y_R^2 + 4F^2}} \tag{5.2}$$

where F_R is calculated using the axis transformation from basic parabolic surface equation as $F_A = x_A^2 + y_A^2 - 4F(F - z_A)$ and $x_0 = H + \frac{D}{2}$. $F,\ D$ and H are the dimensions of offset reflector as specified in Chapter 1.6. $\vec{H}_{i_R}$ is evaluated from feed radiation pattern using proper transformation as

$$\vec{H}_{i_R}(\hat{i}_R,\ \hat{j}_R,\ \hat{k}_R) = \mathbf{R}_{\mathrm{Eu}}\mathbf{T}_{\mathrm{STR}}\vec{H}_{i_F}(\theta_F, \phi_F) \tag{5.3}$$

where $\mathbf{R}_{\mathrm{Eu}}$ is Euler transform matrix

$$\mathbf{R}_{\mathrm{Eu}} = \begin{pmatrix} \cos\alpha & 0 & \sin\alpha \\ 0 & -1 & 0 \\ \sin\alpha & 0 & -\cos\alpha \end{pmatrix} \tag{5.4}$$

and $\mathbf{T}_{\mathrm{STR}}$ is spherical to rectangular transform (STR) matrix

$$\mathbf{T}_{\mathrm{STR}} = \begin{pmatrix} \sin\theta_{_F}\cos\phi_{_F} & \cos\theta_{_F}\cos\phi_{_F} & -\sin\phi_{_F} \\ \sin\theta_{_F}\sin\phi_{_F} & \cos\theta_{_F}\sin\phi_{_F} & \cos\phi_{_F} \\ \cos\theta_{_F} & -\sin\theta_{_F} & 0 \end{pmatrix}. \tag{5.5}$$

It may be noted that the reflector is located at the far zone field of the feed. So, $\vec{H}_{i_{_F}}(\theta_{_F},\phi_{_F})$ is easily calculated from the feed radiation pattern as

$$\vec{H}_{i_F}(\theta_{_F},\phi_{_F}) = \frac{1}{\eta}\hat{a}_{_F} \times \vec{E}_{i_F}(\theta_{_F},\phi_{_F}) \tag{5.6}$$

The radiated $\vec{E}_{_R}(\theta_{_R},\phi_{_R})$ field can be constructed using Huygens scattering equation as

$$\begin{aligned} \vec{E}_{_R}(\theta_{_R},\phi_{_R}) &= -j\frac{k\eta}{4\pi r_{_R}}e^{-jkr_{_R}} \iint\limits_{S'} \left[\vec{J}_{S_{_R}} - \left(\hat{a}_{r_{_R}} \cdot \vec{J}_{S_{_R}}\right)\hat{a}_{r_{_R}}\right] e^{jk\vec{r}'_{_R}\cdot\hat{a}_{_R}} ds' \\ &= -j\frac{k\eta}{4\pi r_{_R}}e^{-jkr_{_R}} \int_0^{\frac{D}{2}}\int_0^{2\pi} \left[\vec{J}_{S_{_R}} - \left(\hat{a}_{r_{_R}} \cdot \vec{J}_{S_{_R}}\right)\hat{a}_{r_{_R}}\right] e^{jk\vec{r}'_{_R}\cdot\hat{a}_{r_R}} f(\rho',\phi')\rho'_{_R} d\phi'_{_R} d\rho'_{_R} \end{aligned} \tag{5.7}$$

where

$$f(\rho',\phi') = \sqrt{\left(\frac{\rho'^2_{_R} + 2\rho'_{_R}x_0\cos\phi'_{_R} + x_0^2}{4F^2} + 1\right)} \tag{5.8}$$

and

$$\vec{r}'_{_R} \cdot \hat{a}_{r_A} = \rho'_{_R}\sin\theta_{_R}\cos(\phi_{_R} - \phi'_{_R}) + z'_{_R}\cos\theta_{_R} \tag{5.9}$$

and

$$z'_{_R} = \frac{\rho'^2_{_R} + 2\rho'_{_R}x_0\cos\phi'_{_R} + x_0^2 - 4F^2}{4F} \tag{5.10}$$

Surface integration of equation (5.7) is carried out with respect to $\rho'_{_R}$ and $\phi'_{_R}$ by numerical technique. Required surface current for this integration is evaluated using equation (5.3) where $\theta'_{_F}$ and $\phi'_{_F}$ are

evaluated by proper transform as specified below:

$$\begin{bmatrix} r'_F \\ \theta'_F \\ \phi'_F \end{bmatrix} \underset{\text{RTS}}{\Leftarrow} \begin{bmatrix} x'_F \\ y'_F \\ z'_F \end{bmatrix} = \mathbf{R}_{\text{Eu}} \begin{bmatrix} x_0 + \rho'_R \cos\phi'_R \\ \rho'_R \cos\phi'_R \\ z'_R \end{bmatrix} \tag{5.11}$$

Here, RTS refers to rectangular to spherical transformation. According to Ludwig [73] co-pol and cross-pol components can be evaluated as:

$$\begin{bmatrix} E_p \\ E_q \end{bmatrix} = \begin{bmatrix} \cos\phi_R & -\sin\phi_R \\ \sin\phi_R & \cos\phi_R \end{bmatrix} \begin{bmatrix} E_{\theta_R}(\theta_R, \phi_R) \\ E_{\phi_R}(\theta_R, \phi_R) \end{bmatrix}. \tag{5.12}$$

5.1.1 Using numerical integration in PO technique

Most important issue in evaluation of equation (5.7) is to carry out the numerical integration with an efficient technique. A very effective technique as found in [74] is the use of Simson's 1/3 rule for the variation of azimuth plane and Gauss-Legendre quadrature method for ρ'_R variation. Empirical equations are used to decide the number of points for the integration as given below:

$$N'_\phi = 3 * \lfloor (2.18\pi \frac{D}{\lambda} \sin 2\theta_F + 3.33) \rceil + 1 \tag{5.13}$$

$$N'_\rho = \lfloor (\frac{N'_\phi}{2.4}) \rceil \tag{5.14}$$

where $\lfloor x \rceil = x - \text{mod}(x - \frac{1}{2}, 1) + \frac{1}{2}$. A MATLAB code is implemented based on the PO technique to evaluate the far-field pattern of the reflector. Using this code, the far field pattern is evaluated for several matched feed designs and the performance has been compared with the simulated results of HFSS.

5.2 Particle swarm optimization (PSO)

Particle swarm optimization technique is a robust probabilistic global optimization technique which belongs to social behavior of swarm's family in the nature. PSO is based on the principle of searching the perfect location to collect the food for flock of birds, swarm of bees and school of fishes. The PSO algorithm was first reported by Kennedy and Eberhart [75, 76] in 1995. The method was first

introduced in the electromagnetic problems [77] by the antenna community in 2004. After that, many variants of PSO has been used for the design of antennas [7, 78–81] and antenna arrays [82, 83]. The PSO can best be understood through an analogy of bee's honey collection in a field [77] and the same is described below for the sake of completeness.

- Imagine a swarm of bees in a field in search of honey. The ultimate goal is to find the location with the highest density of flowers.
- Without primary knowledge about the field, the bees go to random position with random velocity.
- Each bee has the memory to remember the location where it had with highest concentration of flowers and share this information with each other for better searching at the next wave of swarms.
- Being confused about whether to return to the location where it had personally found the maximum concentration of flowers, or to explore the location reported by others, the doubtful bee accelerates in both directions altering its trajectory to fly somewhere between the two points depending on either self influence or social influence whichever dominates.
- Along the way, a bee might get a location with a higher concentration of flowers than previously found. Then It will correct its own searching best location and share it with other bees.
- The search of new location will be stopped when every bee's own best position and the explored most flowers location reported by others are same. Thereafter every bee pulls down its velocity. In this way bees explore the field and achieve to find the location with the highest density of flowers.

In the context of developing the PSO algorithm, the analogous terms are defined like a swarm of bee as particles, own best as personal best ($P\text{best}_{\text{position}}$) and explored best location reported by other bees as global best position ($G\text{best}_{\text{position}}$). To implement the doubtful bee's acceleration, we have used self influence constant (C_1) and social influence constant (C_2) and for making the decision, uniform rand (rand(0,1)) is used in the algorithm. The algorithm developed for our purpose is presented below:

PSO algorithm

(i) **Initialization:-**

- specify

(a) swarm size= S

(b) no of variables= N

(c) minimum and maximum limits of variables =$[\mathbf{X}_{\min}, \mathbf{X}_{\max}]$

(d) inertia weight= W

(e) self influence constant= C_1

(f) social influence constant= C_2

- Termination condition

(g) maximum no of iteration =$I\text{teration}_{\max}$

(h) acceptable optimum fitness value =F_{opt}

(i) minimum standard deviation of particles =P_{sd}

- initialized some matrix given below:

(j) initial velocity of particles $\mathbf{V}_{\text{new}}$=zeros(S,N)

(k) initial particle swarm best value $\mathbf{P}\text{best}_{\text{value}} = \infty *$ ones(S,1)

(ii) **Generate the random particles:-** set up the random particles using the limits of variables

$$[\mathbf{X}_{\text{new}}]_{S\times N}=\mathbf{X}_{\min}+\text{rand}(0,1)_{S\times N}(\mathbf{X}_{\max}\text{-}\mathbf{X}_{\min})$$

(iii) **Particle swarm main algorithm:-**

- start the iteration: do

(a) calculate the fitness value of new particles

(b) check the termination condition for P_{sd}, F_{opt} and $I\text{teration}_{\max}$, if one of them satisfies on new particle position, fitness value ($\mathbf{F}$) and iteration, stop the iteration.

(c) compare the $\mathbf{P}\text{best}_{\text{value}}$ and $\mathbf{F}$, according to comparison result update the $\mathbf{P}\text{best}_{\text{position}}$ and $G\text{best}_{\text{position}}$ using new particle's position $\mathbf{X}_{\text{new}}$

(d) overwrite the old particle's position and the old velocity using the new particle's position vector and new velocity.

$$\mathbf{X}_{\text{old}} = \mathbf{X}_{\text{new}}$$
$$\mathbf{V}_{\text{old}} = \mathbf{V}_{\text{new}}$$

(e) update the particle's velocity using this relation

$$\mathbf{V}_{\text{new}} = W * \mathbf{V}_{\text{old}} + \text{rand}(0,1) * C_1(\mathbf{P}\text{best}_{\text{position}} - \mathbf{X}_{\text{old}}) + \text{rand}(0,1) * C_2(G\text{best}_{\text{position}} - \mathbf{X}_{\text{old}})$$

(f) generate the new particles using the new velocity

$$\mathbf{X}_{\text{new}} = \mathbf{X}_{\text{old}} + \mathbf{V}_{\text{new}}$$

(g) check the boundary condition of $\mathbf{X}_{\text{new}}$ and pull back the particles toward the allowed solution space $[\mathbf{X}_{\min}, \mathbf{X}_{\max}]$

- continue the iteration: until the condition of (b) satisfy

In engineering applications, it is desirable to limit the search within practical limits. At times in application of PSO, the new generated particles cross the boundary due to high acceleration of particles. To pull back the highly accelerated particles toward the allowed solution space, different types of boundaries are reported in literature [77], like absorbing boundary, reflection boundary and invisible boundary. Absorbing boundary absorbs the energy of highly accelerated particles and particles are forcibly kept at the boundary wall after absorbing their energy. In case of reflection boundary, particles are reflected back toward the solution space through the changing of sign of the velocity. Invisible boundary allows the particles outside the solution space, but these particles are taken care of at the time of evaluation of the fitness value by considering their poor performance. Resultant particles are forced to fly in the solution space. In our development of PSO, we have considered the boundary as a combination of absorbing and reflection boundary to restrict the particles within solution space. Basically, particles moving outside are pulled into the solution space using the random uniform data between the crossing wall and old particle location.

Termination condition of PSO can be implemented in different ways, which are reported in [77]. In our development, maximum no of iteration, acceptable optimum fitness value and minimum standard deviation of particles are used as terminating conditions and when at least one of them is satisfied, the code gets terminated.

In the development of the PSO algorithm, self influence constant, social influence constant, inertia weight and swarm size have important roles on the success of searching the global optimization value. The empirical values of those parameters are reported in literature [77, 84, 85]. From our experiment, we have considered $W = 0.76$, $C_1 = 1.46$, $C_2 = 1.46$ and swarm size equal to 20 to improve the performance.

5.2.1 Performance of developed PSO technique

Various test function as mentioned in [77, 85] are used to evaluate the performance of developed artificial optimization techniques. Some of them as given in Table 5.1 are considered to study the performance of our developed code. The performances are shown in Figures 5.1 and 5.2 respectively, for the sphere and Ackley's function and as expected, good performance is observed. It may be pointed out that different parameters have been used as specified in Section 5.2. Average, worst and best performances are observed from 1000 events to investigate the performance of PSO for studying both cases.

Table 5.1: Various test functions for optimization.

Function	Formula	Search domain	Minimum
Sphere function	$F(x) = \sum_{i=1}^{10} {x_i}^2$	$-100 \leq x_i \leq 100$	$f(0, 0, \ldots, 0) = 0$
Ackley's function	$F(x,y) = -20\exp(-0.2\sqrt{0.5(x^2+y^2)})$ $-\exp(0.5(\cos(2\pi x)+\cos(2\pi y)))$ $+\exp(1)+20$	$-5 \leq x, y \leq 5$	$f(0,0) = 0$

5.3 Analytical or semi-analytical study for matched feed design

Use of PO technique along with analytical or semi-analytical feed pattern of multi-mode horn provides valuable insights on the performance of the the reflector antenna system for various parameters such as feed aperture dimensions, reflector dimensions, contribution of higher order modes and effect of feed polarization [1, 6–10]. As mentioned in Section 1.2, multi-mode horn has the ability to elimi-

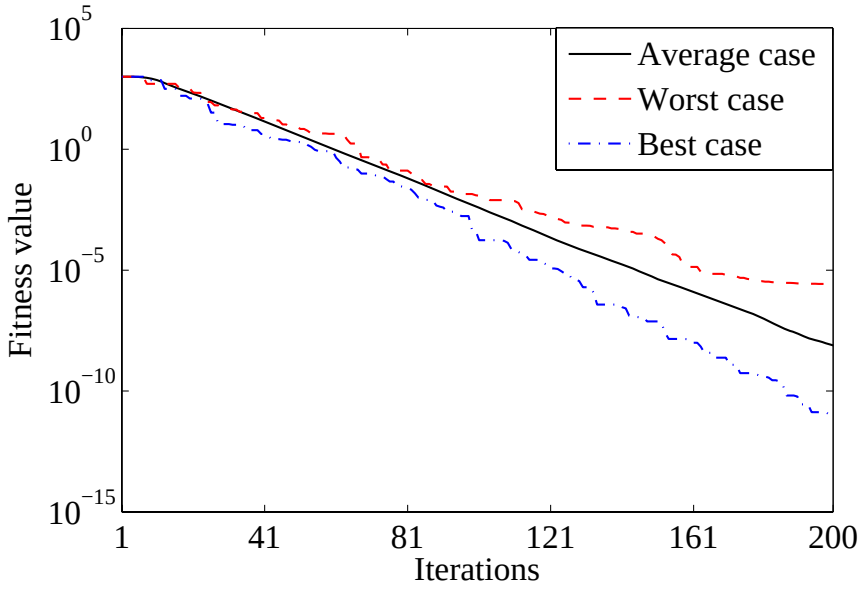

Figure 5.1: Performance of developed PSO for sphere function.

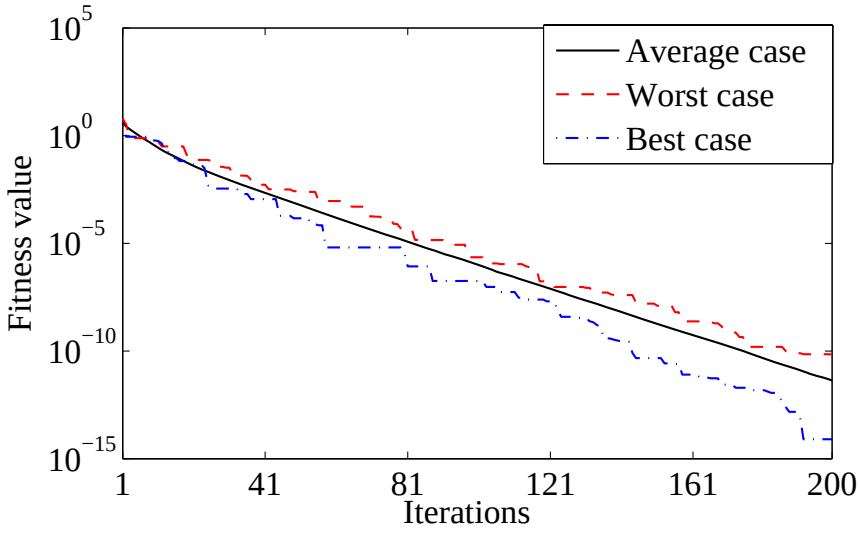

Figure 5.2: Performance of developed PSO for Ackley's function.

nate the depolarization effect of reflector by proper choice of higher order mode(s), its magnitude and phase relative to the main operating mode. PSO technique is used to estimate the required relative magnitude and phase of higher order mode(s) for realizing the desirable secondary pattern for linear polarized matched feed. Steps involved with such estimation are given below in detail:

- Analytical multi-mode power balance far-field pattern for considered feed aperture is calculated using Chu's model as mentioned in Section 4.4. Generally, this calculation is carried out when

the analytical solution of Helmholtz equation is available for the considered aperture.

- If analytical solution of Helmholtz equation is not available for the considered feed aperture, Helmholtz equation is solved by 2D-FEM technique as mentioned in Section 3.2. Multi-mode power balance far-field pattern is evaluated using equations (4.57) and (4.58) employing barycentric subdivision four points integration for same triangular mesh which is used for FEM solution.
- To investigate cross-polar level at the secondary pattern, PO is used. As mentioned, PO has the ability to accurately predict the main lobe pattern.
- During the investigation of cross-polar power at secondary pattern, total feed radiated power (sum of powers of main mode and higher order modes) is always kept as 1 Watt.
- PSO is used to estimate the required higher order mode coefficient and its phase to obtain the low cross-polar field at secondary pattern by using proper fitness function as $10\log_{10}(\frac{\text{Cross-polar power}}{\text{Co-polar power}})$.

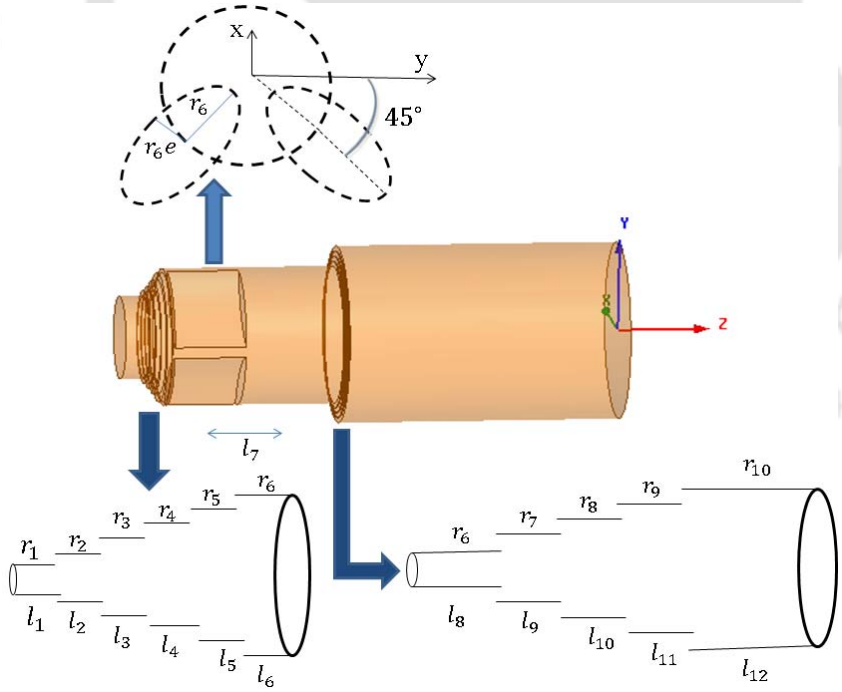

Figure 5.3: Our proposed matched feed and its dimensions : $\{r_1,\ r_2,\ r_3,\ r_4,\ r_5,\ r_6,\ r_7,\ r_8,\ r_9,\ r_{10},\ l_1,\ l_2,\ l_3,\ l_4,\ l_5,\ l_6,\ l_7,\ l_8,\ l_9,\ l_{10},\ l_{11},\ l_{12}\} = \{17,\ 19,\ 21,\ 23.5,\ 26.5,\ 28,\ 30,\ 32,\ 34,\ 36,\ 10,\ 2,\ 2,\ 2,\ 2,\ 1,\ 30,\ 41,\ 0.5,\ 0.5,\ 0.5,\ 118.2\}$ mm and $e = 2$.

5.4 A stepped circular matched feed design using TE^1_{11}, TE^1_{21} and TM^1_{11} modes

TE^1_{11}, TE^1_{21} and TM^1_{11} modes are often used in design of linerly polarized circular matched feed to remove the depolarization effect of an offset reflector antenna. Generally, TE^1_{21} mode is generated using three pins and a large step discontinuity is used to generate the TM^1_{11} mode as found in [7]. From our experience, it is observed that use of such kind of discontinuities affect the return loss. To improve the return loss and cross-polar bandwidth, a new kind of structure is proposed in this chapter as shown in Figure 5.3. A brief description of the design technique is presented below:

- The radius of open aperture r_{10} is chosen in such a way that it supports propagation of TE^1_{11}, TM^1_{11} and TE^1_{21} mode in the frequency band of interest.
- The value of r_6 is so chosen that it ensures the cutoff condition for TM_{11} mode in that waveguide section but supports the TE^1_{21} mode.
- To improve the impedance matching, the transition of waveguide radius from r_1 to r_6 is achieved using a stepped waveguide as shown in Figure 5.3
- Similarly, stepped waveguides having radii r_7, r_8, r_9 are placed between r_6 and r_{10} to generate the required amount TM^1_{11} mode.
- Two surfaces having elliptical cross sections and inclined at 45° with respect to x axis in the r_6 waveguide as shown in Figure 5.3, are used to generate the TE^1_{21} mode.
- Mainly, the lengths l_8 and l_{12} are used to control the relative phases of TE^1_{21} and TM^1_{11} with respect to TE^1_{11} mode.

Table 5.2: Estimated mode coefficients and relative phases at 6 GHz.

Mode	TE^1_{11}	$TM^1_{11} + TE^1_{21}$	Cross-polar power	
			45°	90°
Case 1:	$1\angle -$	-	−22.8 dB	−19.5 dB
Case 2:	$0.8409\angle 0°$	$0.4663\angle 0° + 0.2747\angle -89.3°$	−47.5 dB	−47.65 dB

Matched feed is designed for a given specification of an offset reflector antenna for which dimensions are $F = 0.8$ m, $D = 1.3$ m and $H = 0.2$ m. Generalized power balanced far field pattern of circular

horn is derived using Chu's model as specified in Section 4.4 for the case of an x polarized waveguide. The far field pattern of TE^1_{mn} mode is derived as

$$E_\theta^{TE^1_{mn}} = j^{m+1} V^+_{A_{TE_{mn}}} \sqrt{\frac{k\eta}{\beta_{mn}(1+\partial_{0m})\pi(x_{mn}^2 - m^2)}} \frac{2m}{R}(1 + \frac{\beta_{mn}}{k}\cos\theta)\frac{J_m(ka\sin\theta)}{\sin\theta}\sin m\phi e^{-jkR} \tag{5.15}$$

$$E_\phi^{TE^1_{mn}} = j^{m+1} V^+_{A_{TE_{mn}}} \sqrt{\frac{k\eta}{\beta_{mn}(1+\partial_{0m})\pi(x_{mn}^2 - m^2)}} \frac{2ak}{R}(\frac{\beta_{mn}}{k} + \cos\theta)\frac{J'_m(ka\sin\theta)}{1-(\frac{k\sin\theta}{k_c})^2}\cos m\phi e^{-jkR}. \tag{5.16}$$

where β_{mn}, k_c and η are the propagation constant, wave cutoff of mode and free space wave propagation, respectively. R, θ and ϕ are the coordinates of observation point of the far field. The far field pattern of TM^1_{mn} mode can be written as

$$E_\theta^{TM^1_{mn}} = -j^{m+1} V^+_{A_{TM_{mn}}} \sqrt{\frac{k\eta}{\beta_{mn}(1+\partial_{0m})\pi}} \frac{2}{R\sin\theta}(\frac{\beta_{mn}}{k} + \cos\theta)\frac{J_m(ka\sin\theta)}{1-(\frac{k_c}{k\sin\theta})^2}\sin m\phi e^{-jkR} \tag{5.17}$$

$$E_\phi^{TM^1_{mn}} = 0. \tag{5.18}$$

It may be noted that $V^+_{A_{TE_{mn}}}$ and $V^+_{A_{TM_{mn}}}$ are the mode coefficients of TE and TM mode, respectively. Figure 5.4 shows the computed cross-polar level at secondary pattern obtained using our developed code when the feed is excited with the TE^1_{11} mode. Same results are compared by the simulated HFSS results and close agreements are found. As specified in Section 5.3, an analytical technique is used to estimate the required mode ratio and relative phase of TE^1_{21} and TM^1_{11} mode to obtain the low cross-polar secondary pattern at the design frequency of 6 GHz. Detail studies are presented in Table 5.2.

5.5 Investigation on the performance of MM/2D-FEM/MOM/PO technique for proposed matched feed structure

As discussed in Chapter 2, Chapter 3 and Chapter 4, feed modeling is carried out using the combination of MM, 2D-FEM and MoM technique and PO as specified in Section 5.1 is used to obtain the reflector far-field pattern of our proposed technique. In this Section, the performance of our proposed technique is investigated for the considered matched feed structure.

The dimensions of matched feed are decided using HFSS through the adjustment of required mode

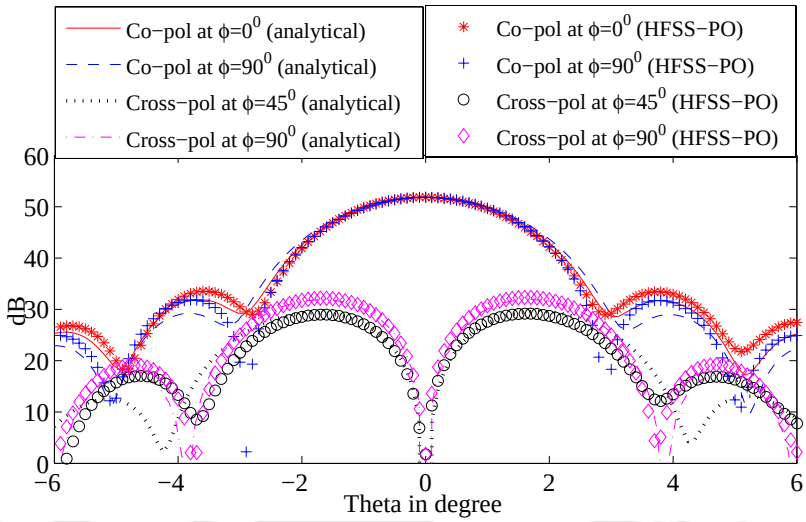

Figure 5.4: Cross-polar performance of TE_{11}^{1} mode at 6 GHz.

coefficient and its relative phases as specified in Table 5.2. The scattering parameters and relative phases are given in Figure 5.5, 5.6. The performance of developed hybrid technique (MM/2D-FEM) is evaluated and compared with simulated HFSS results for the proposed matched structure.

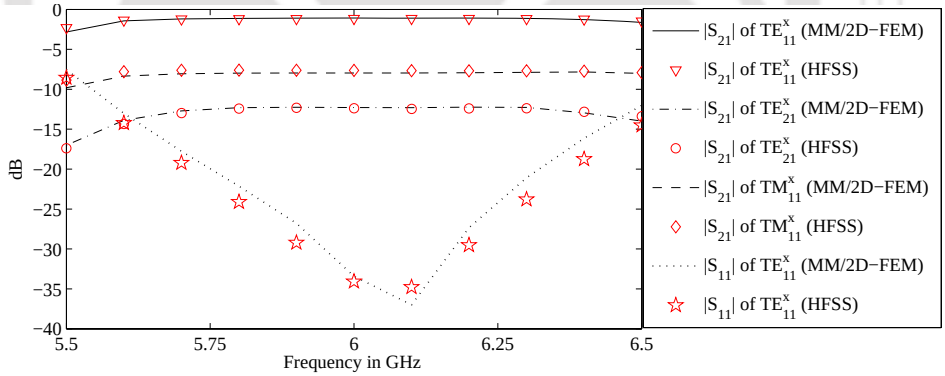

Figure 5.5: Scattering parameters of our proposed matched feed.

The performance of developed MM/2D FEM/MoM is also investigated for the proposed matched feed. Computed reflection coefficient and far-field pattern at 6 GHz are compared with simulated HFSS results, and these are plotted in Figure 5.7 and 5.8. Close agreements are found for these comparisons.

The cross-polar performance at secondary pattern is investigated using MM/2D FEM/MoM/PO technique and also compared with HFSS results as shown in Figure 5.9. It may be noted that 3D FEM technique for feed and PO for reflector are used to simulate in HFSS. Also, the analytical secondary

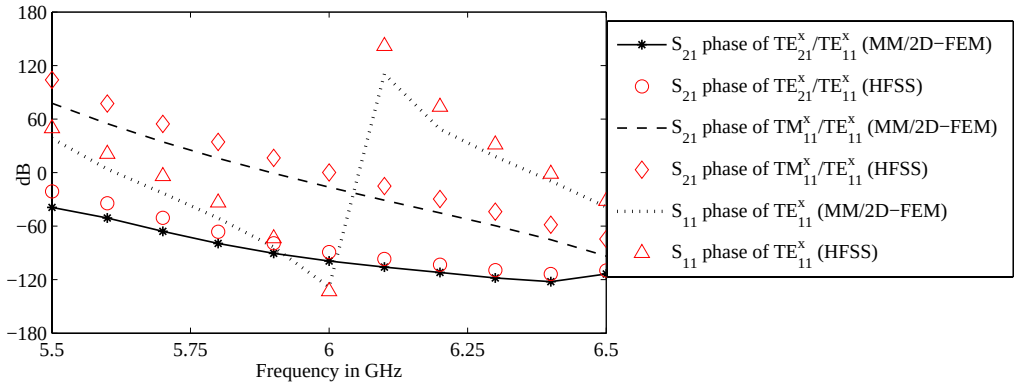

Figure 5.6: Relative phase of scattering parameters of our proposed matched feed.

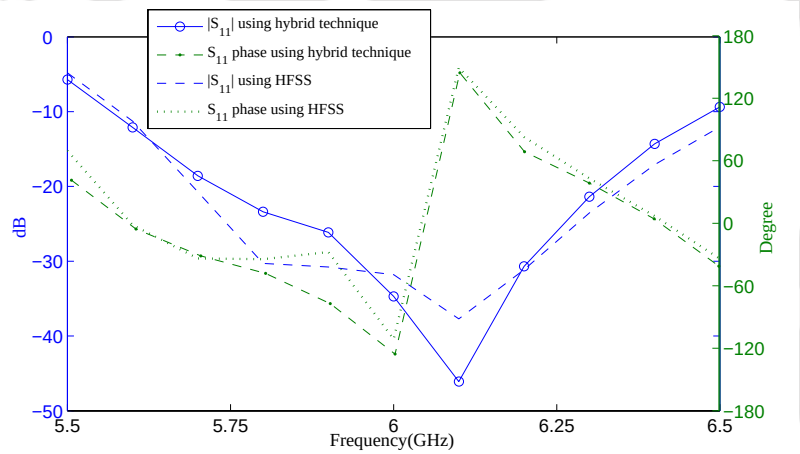

Figure 5.7: Reflection coefficient of our proposed feed.

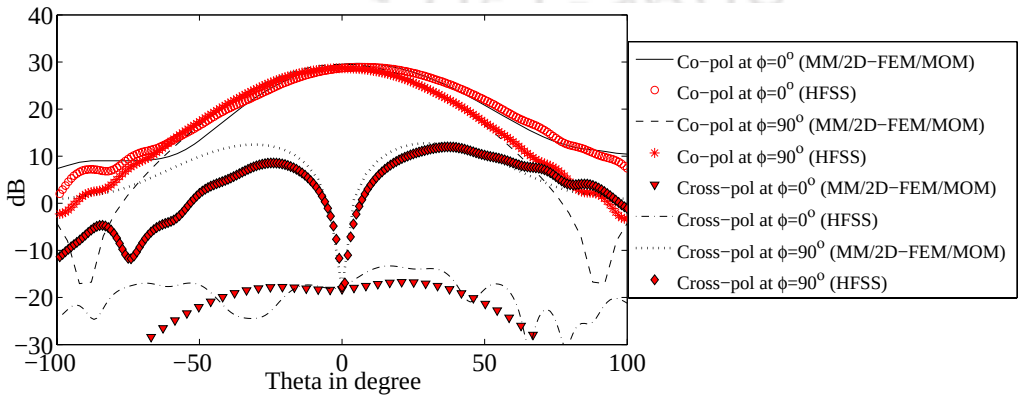

Figure 5.8: Feed radiation pattern at 6 GHz.

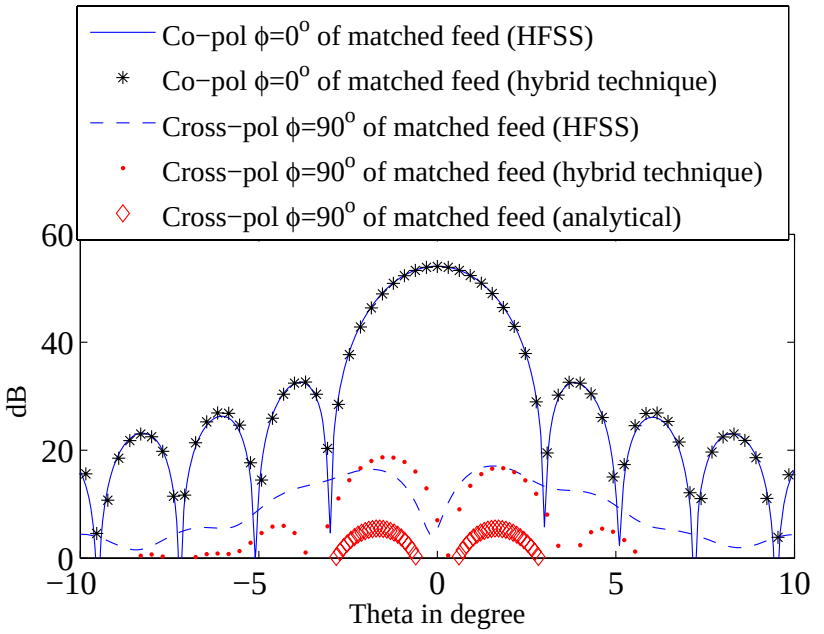

Figure 5.9: Secondary cross-polar performance of proposed matched feed at 6 GHz.

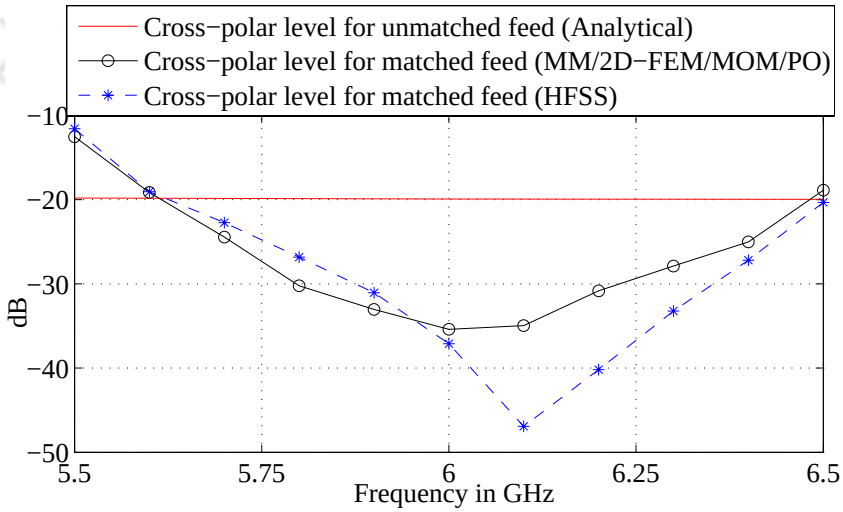

Figure 5.10: Cross-polar performance of proposed matched feed.

pattern for the estimated mode coefficient and the relative phases (as specified in Table 5.2) is plotted in Figure 5.9. The cross-polar bandwidth is investigated using HFSS as well as using our developed hybrid technique as shown in Figure 5.10.

5.6 Conclusion

A new kind of matched feed structure has been proposed using TE_{11}^1, TE_{21}^1 and TM_{11}^1 modes. In this design, appropriate junctions to generate the higher order modes have been used to achieve the wideband performance. Moreover, its performances have been investigated using our developed hybrid technique MM/2D FEM/MoM/PO. A brief theory on matched feed design technique using analytical and semi-analytical method have been explained in connection with analysis of the feed and the reflector. Also, discussions on PSO has been presented to explain how it has been incorporated along with the analytical and semi-analytical method to obtain low cross-polar secondary pattern.

6

Design of Novel Matched Feed Structures

Contents

In this chapter, several matched feed structures are designed using PSO optimization technique along with analytical or semi-analytical model of feed and reflector. The first design is a rectangular matched feed based on TE_{01} and TM_{11} operating modes. In the next design, a non-regular type of matched feed structure for wide-band application is presented in this chapter. This is followed by a wide-band diagonal matched feed which is introduced to suppress the cross-polar power of the asymmetric-plane of an offset reflector antenna. A feed structure utilizing the conjugate field radiated from a rectangular choke excited by two slots on a diagonal horn to suppress the wide-band cross-polar power of an offset reflector antenna is also proposed. Design techniques for all the horn structures are explained in details.

6.1 A novel rectangular matched feed

Based on the analytical studies, Rudge and Adatia reported that a rectangular matched feed combining dominant TE_{01} and proper amount of TE_{11} or TM_{11} mode suppresses the cross-polar level of an offset reflector antenna [1]. However, practical realization of smooth walled rectangular matched feeds that are reported in literature [1,6] use a combination of TE_{01} and TE_{11} modes only. It is observed through analytical study that combination of TE_{01} and TM_{11} modes provides better performance as compared to $TE_{01} + TE_{11}$ and $TE_{01} + TE_{11} + TM_{11}$ cases. To the best of our knowledge, the design of rectangular matched feed using TE_{01} and TM_{11} mode is not adequately addressed in literature. A shifted waveguide junction based design is introduced here for a matched feed that uses TE_{01} and TM_{11} mode combination. It is observed in this study that due to use of such shifted waveguide structure, return loss performance is not affected much whereas in pin based matched feed design, return loss gets affected [6, 86]. In this section, the design of shifted waveguide based rectangular matched feed is dealt in detail.

6.1.1 Analytical study to reduce the cross-polarization level

In this study the same approach as described earlier is used; a contour plot of reflector cross-polar power is generated corresponding to TE_{11}/TM_{11} mode coefficients and relative phase of analytical dual mode feed pattern. Also, a PSO technique has been used to estimate the required mode coefficients and relative phases of analytical tri-mode ($TE_{01} + TE_{11} + TM_{11}$) feed pattern to obtain the low cross-polarization pattern of the reflector as specified in 5.3.

Generalized power balanced far field radiation patterns of multi-mode rectangular horn have been derived using the concept of Chu's model [21] and detail theory as discussed in Section 4.4 is employed to derive it. The electric field components of the far field pattern due to TE_{mn} mode can be written as

$$E_{\theta}^{TE_{mn}} = j^{m+n} V_{TE_{mn}} (1 + \frac{\beta_{mn}}{k} \cos\theta) \sin\theta [(mb \sin\phi)^2 - (na \cos\phi)^2] \psi_{mn} \frac{e^{-jkR}}{R}$$

$$E_{\phi}^{TE_{mn}} = j^{m+n} V_{TE_{mn}} (\cos\theta + \frac{\beta_{mn}}{k}) \sin\theta \sin\phi \cos\phi [(mb)^2 + (na)^2] \psi_{mn} \frac{e^{-jkR}}{R}.$$

Similarly, electric field components of the far field pattern of TM_{mn} mode are

$$E_{\theta}^{TM_{mn}} = j^{m+n} V_{TM_{mn}} (\cos\theta + \frac{\beta_{mn}}{k}) \sin\theta \frac{mn}{ab} \psi_{mn} \frac{e^{-jkR}}{R},$$

$$E_{\phi}^{TM_{mn}} = 0,$$

where R, θ and ϕ are the coordinates of the observation point of far field and β_{mn}, k and η represent the different modes' propagation constant, free space wave number and free space wave impedance, respectively. a and b represent the horn aperture dimensions and $V_{TE_{mn}}$, and $V_{TM_{mn}}$ are the mode coefficients. ψ_{mn} is defined as

$$\psi_{mn} = \left(\frac{k^{\frac{5}{2}} \sqrt{\eta ab}}{\sqrt{2\beta_{mn}(1+\delta_{0m})(1+\delta_{0n})((mb)^2 + (na)^2)}}\right)\left(\frac{\mathrm{sinc}(\frac{ka \sin\theta \cos\phi + m\pi}{2})}{(ka \sin\theta \cos\phi - m\pi)} \frac{\mathrm{sinc}(\frac{kb \sin\theta \sin\phi + n\pi}{2})}{(kb \sin\theta \sin\phi - n\pi)}\right)$$

where $\delta_{ij} = \begin{cases} 1, & i = j \\ 0, & i \neq j \end{cases}$

The feed design has been carried out for the following offset reflector and horn aperture dimensions: $F = 1$ m, $D = 1.3$ m, offset height $H = 0.12$ m, $\alpha = 38.8^{\circ}$ and $a \times b = 0.088 \times 0.124$ m^2. For an optimal design of the matched feed, the performance of dominant mode (TE_{01}) in suppressing the cross polar level of secondary pattern using the proper combination of TE_{11} and or TM_{11} mode have been studied and appropriate mode coefficients and relative phases have been evaluated. As mentioned earlier, in this analytical study, the power balance concept for total radiated power has been used. Analytically,

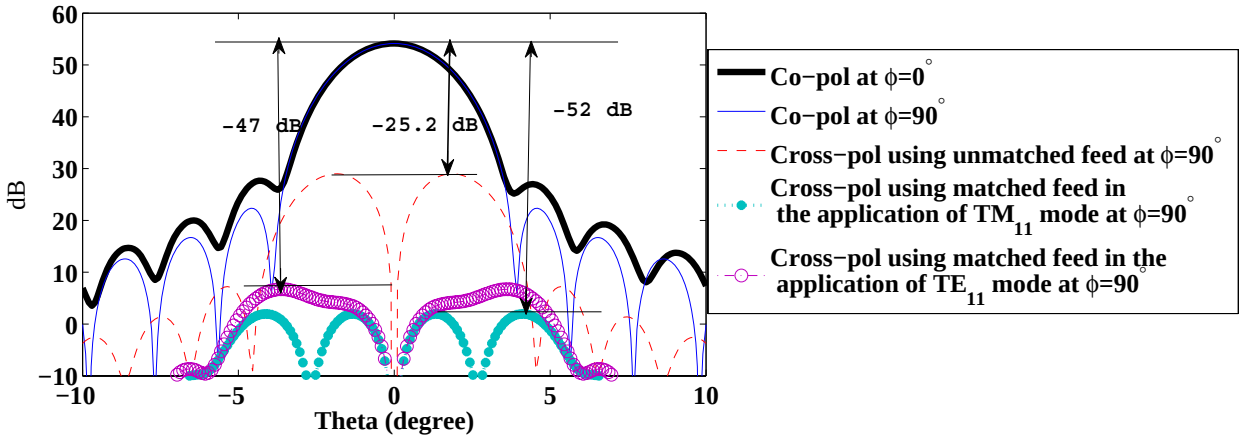

Figure 6.1: Analytical secondary radiation pattern for unmatched and matched feed at 6 GHz, computed using MATLAB.

effective far field radiation pattern of feed can be written as

$$E = \begin{pmatrix} E_{TE_{01}} \\ E_{TE_{11}} \\ E_{TM_{11}} \end{pmatrix}^T \begin{pmatrix} \sqrt{1 - |V_{TE_{11}}|^2 - |V_{TM_{11}}|^2} \\ V_{TE_{11}} \\ V_{TM_{11}} \end{pmatrix} \tag{6.1}$$

where $V_{TE_{11}}$ and $V_{TM_{11}}$ are the complex mode coefficients of TE_{11} and TM_{11} mode. Cross polar performance of the reflector is studied for different combinations of mode(s) of the feed and the same is presented below:

- **Case 1:-**The reflector cross-polar performance of TE_{01} mode excitation is shown in Figure 6.1 for the specified antenna system parameters. A high cross-polar power, close to -25.2 dB, is observed for this unmatched feed.

- **Case 2:-**To estimate the required mode coefficient and relative phase of TM_{11} mode for $TE_{01} + TM_{11}$ combination, a contour plot of cross-polar level of secondary pattern has been generated with respect to TM_{11} mode coefficient, and relative phase and the contour plot obtained is shown in Figure 6.2. The estimated values of desired mode coefficients and relative phases for the design of matched feed are shown in the Table 6.1. With the values of the mode coefficients and relative phase given in Table 6.1, cross-polar level in the secondary radiation for the analytical feed pattern reduces to -52 dB (as compared to -25.2 dB for the unmatched case) and the same is also shown in Figure 6.1.

- **Case 3:-** A contour plot of cross-polar level with respect to coefficient and relative phase of TE_{11} mode is plotted in Figure 6.3. The required mode coefficient and phase for suppressing the cross-polarization are shown in Table 6.1 and also the cross-polarization pattern has been shown in Figure 6.1. It is observed as compared to $TE_{01} + TM_{11}$ mode combination, improvement of cross-polar level is less for $TE_{01} + TE_{11}$ mode combination, -47 dB cross-polar level has been achieved.

- **Case 4:-** Performance of a tri-mode combination consisting of TE_{01}, TE_{11} and TM_{11} is also studied analytically. In this study, the unknown variables $V_{TE_{11}}$ and $V_{TM_{11}}$ are complex coefficients. To solve this problem, a PSO based technique has been used. The estimated mode coefficients and phases are enlisted in the Table 6.1. It is observed in this study that coefficient value of TM_{11} plays a more significant role in suppressing the cross-polar level. We have studied some special cases for the tri-mode combination which are described below:

  - **Special Case 4.1**:- In this scenario, we have considered that both complex coefficients of $V_{TE_{11}}$ and $V_{TM_{11}}$ are equal and a contour plot of cross-polar magnitude in dB has been shown in Figure 6.4. The optimum coefficients and relative phases value are enlisted in Table 6.1.

  - **Special Case 4.2**:- We have investigated another special case where $V_{TE_{11}}$ and $V_{TM_{11}}$ magnitudes are equal but their relative phases are different. Using PSO technique, we have estimated the optimum coefficient and phases for suppressing the cross polar level in secondary pattern and those values are presented in Table 6.1. It shows an interesting evidence that combination of different relative phases of TE_{11} and TM_{11} are sufficient to generate the conjugate of the cross-pol field.

From the results of analytical study presented in Table 6.1, it is observed, the performance of $TE_{01} + TM_{11}$ mode combination is better compared to other cases. However, the majority of the reported structures on rectangular matched feed have been found to use $TE_{01} + TE_{11}$ mode [1, 6]. In the next section, we propose a new structure of a smooth walled rectangular matched feed involving TE_{01} of TM_{11} modes.

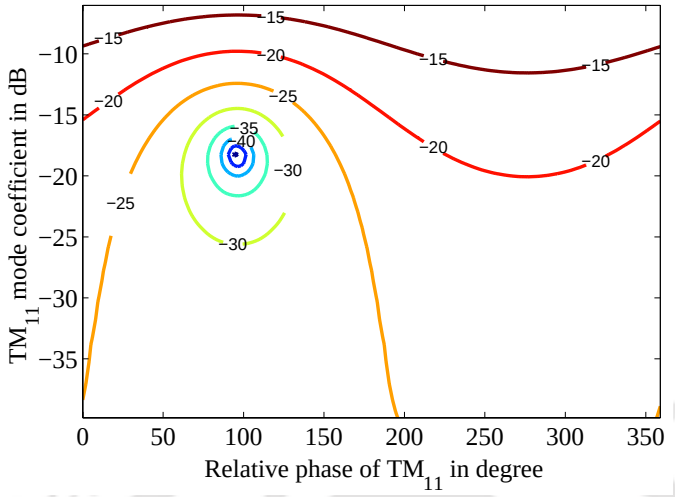

Figure 6.2: Contour plot of cross-polar power with respect to coefficient and relative phase of TM_{11} mode at 6 GHz.

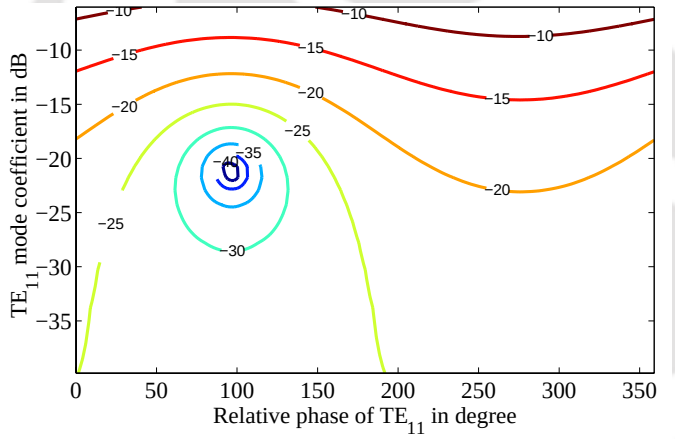

Figure 6.3: Contour plot of cross-polar power with respect to coefficient and relative phase of TE_{11} mode at 6 GHz.

6.1.2 Feed Design and Results

The proposed structure of matched feed with specified dimensions is shown in the Figure 6.5. Higher order modes are generated using a junction consisting of a shifted waveguide. The matched feed design is carried out based on the parametric study of some specific dimensions in HFSS. The matched feed is excited using a standard waveguide WR-137. Since TE_{11} and TM_{11} are degenerate modes having the same cutoff frequency, retainment of TM_{11} mode and suppression of TE_{11} mode is a challenging task in this design. However, it is observed that the choice of the rectangular dimensions $(a_1 \times b_1)$ plays an important role to generate the equal or unequal power level of TM_{11} and TE_{11}

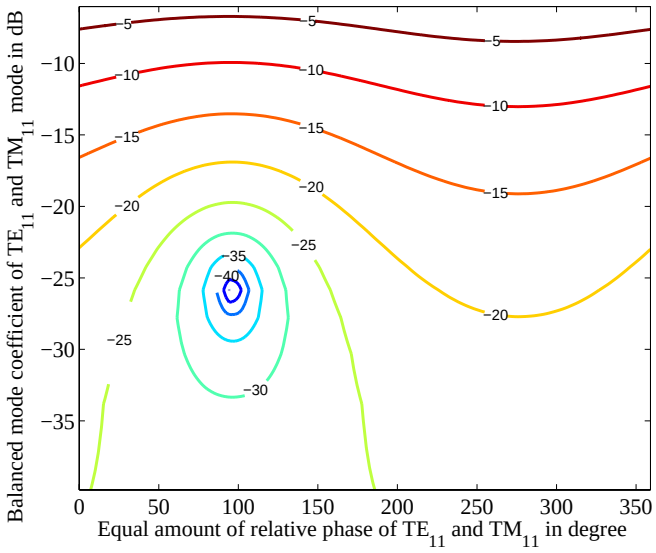

Figure 6.4: Contour plot of cross-polar power with respect to balanced coefficient and same amount of relative phase of TE_{11} and TM_{11} mode at 6 GHz.

Table 6.1: Estimated the mode coefficients and relative phases using analytical technique for the matched feed design at 6 GHz.

Mode	TE_{01}	TE_{11}	TM_{11}	Cross-polar level
Case 1:	0 dB ∠−	-	-	−25.2 dB
Case 2:	−0.061 dB ∠0°	-	−18.644 dB ∠95.3°	−52 dB
Case 3:	−0.0368 dB ∠0°	−20.739 dB ∠94.26°	-	−47 dB
Case 4:	−0.061 dB ∠0°	−63 dB ∠175°	−18.639 dB ∠95.3°	−51.98 dB
Special Case4.1:	−0.02271 dB ∠0°	−25.85 dB ∠94.27°	−25.85 dB ∠94.27°	−50.1 dB
Special Case4.2:	−0.1031 dB ∠0°	−19.2924 dB ∠50.5750°	−19.2924 dB ∠−179.8572°	−50.18 dB

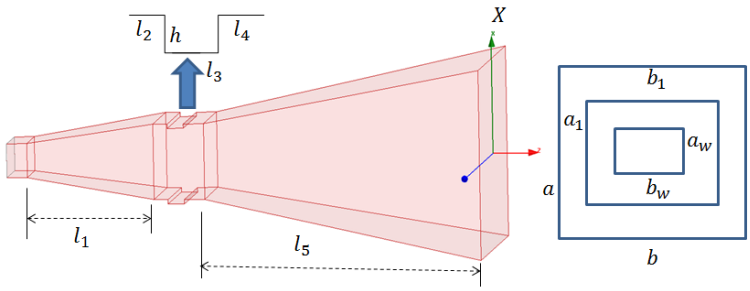

Figure 6.5: The proposed matched feed structure including all the dimensions are $a_w \times b_w = 15.8 \times 34.85$ mm^2, $a_1 \times b_1 = 35 \times 60$ mm^2, $a \times b = 88 \times 124$ mm^2, and $\{l_1, l_2, l_3, l_4, l_5, h\} = \{64, 7, 8, 10, 124, 2\}$ mm.

Table 6.2: Adjusted mode coefficients and relative phases of matched feed at 6 GHz.

Mode	TE_{01}	TM_{11}	TE_{11}
Coefficient	-0.087 dB	-19.03 dB	-32.69 dB
Relative phase	0°	97.6°	126.91°

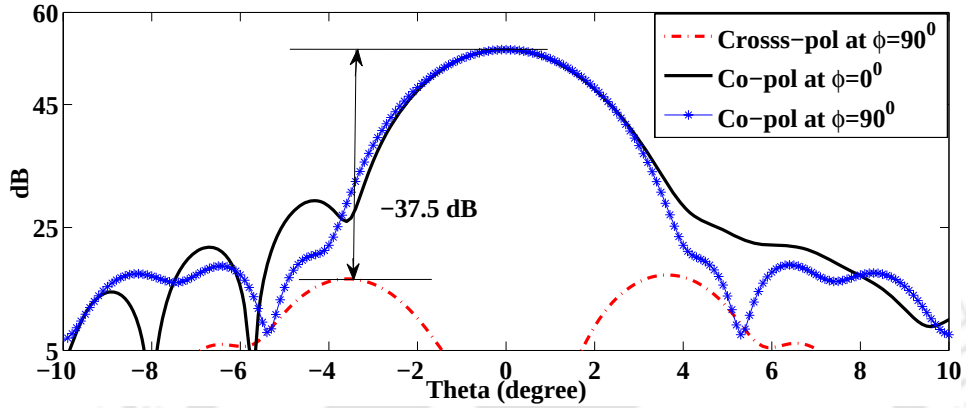

Figure 6.6: Simulated cross-polar performance of secondary pattern in HFSS at 6 GHz when matched feed is linear polarized.

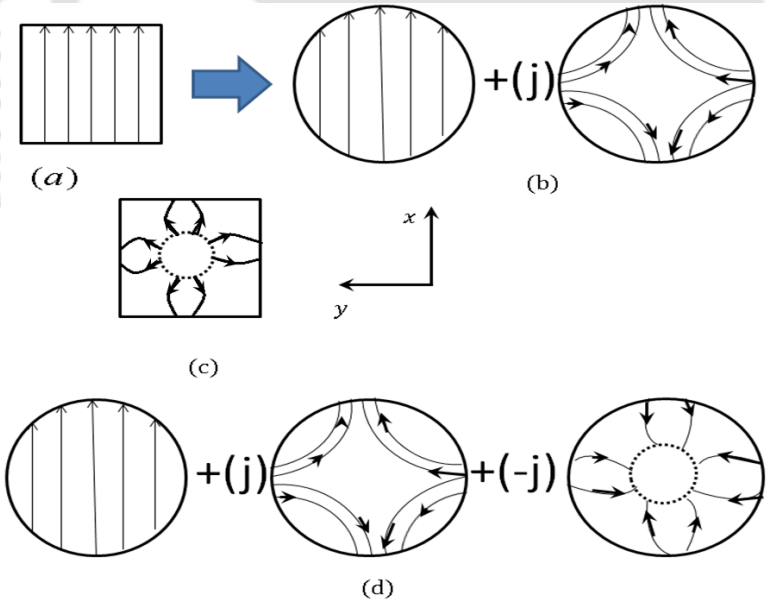

Figure 6.7: Cross-polarization suppression technique of an offset reflector antenna using TE_{01} and TM_{11} mode. (a):-Feed aperture pattern of TE_{01} mode (b):-Field configurations of symmetric and asymmetric components at focal plane of reflector (c):- Field pattern of TM_{11} mode (d):-The conjugate matching in the application of TM_{11} mode, it cancels the y component of symmetric pattern.

modes, when any kind of discontinuity is kept inside the rectangular waveguide. The shifted waveguide junction has been designed appropriately through the parametric study in HFSS for proper choice of rectangular dimensions ($a_1 \times b_1$). This allows the generation of very highly unbalanced power levels

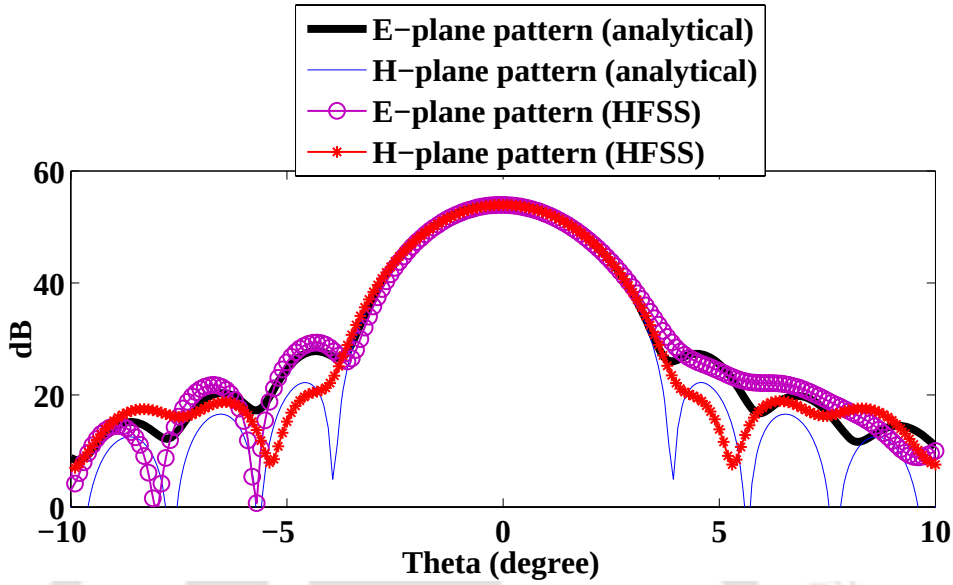

Figure 6.8: Analytical (computed using MATLAB) and Simulated (HFSS) reflector patterns at 6 GHz for matched feed excitation.

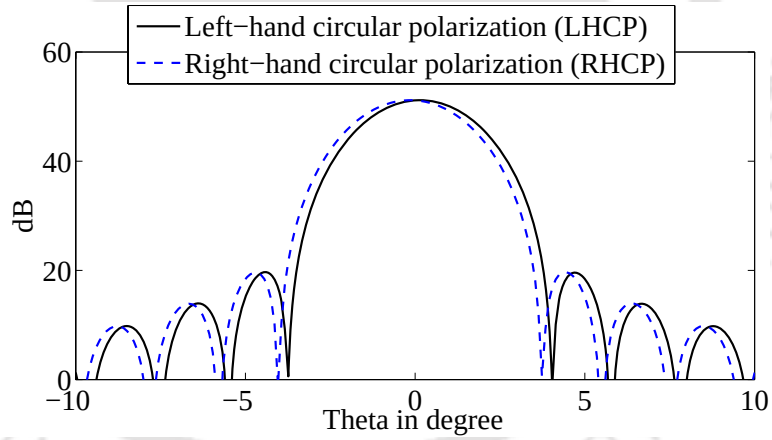

Figure 6.9: Computed beam squinting of secondary pattern at 6 GHz for the unmatched feed.

between TM_{11} and TE_{11} modes, and hence higher TM_{11} power level as compared to TE_{11} could be achieved in our design. Offset height (h) of shifted waveguide is used to control the magnitude of TM_{11} mode and l_5, and l_4 lengths are used to adjust the required relative phase. Length l_1 is used for the improvement of impedance bandwidth. The adjusted mode coefficients and relative phases are given in the Table 6.2. The simulated cross-polar performance is given in Figure 6.6. As seen in the Figure, -37.5 dB cross-polar power level has been achieved when the entire antenna system is simulated in HFSS V15. It may be pointed out here the PO package of HFSS V15 has been used for computation of the secondary pattern. The cross polar suppressing technique with the application of TM_{11} mode

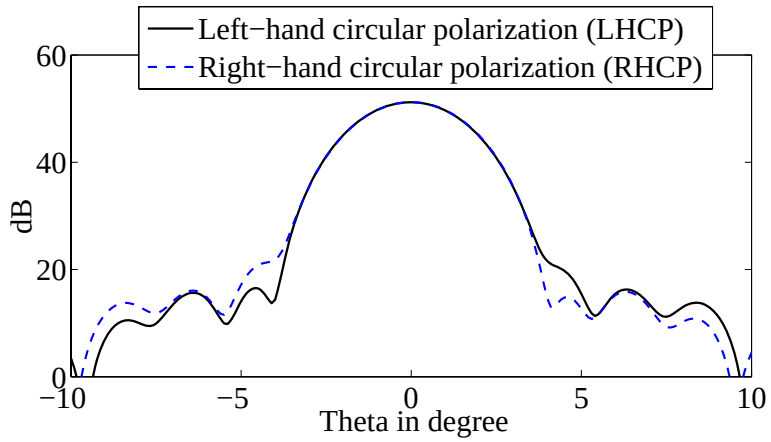

Figure 6.10: HFSS simulated beam squinting performance of secondary pattern at 6 GHz when the feed is matched.

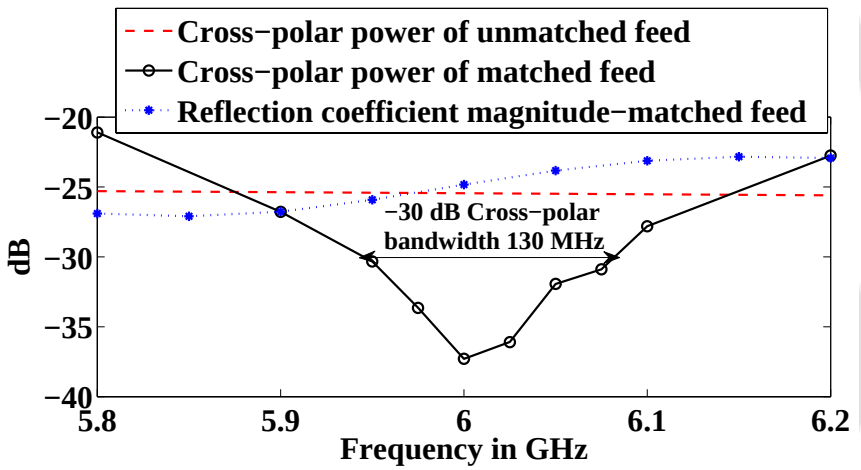

Figure 6.11: Simulated HFSS results of impedance and cross-polar bandwidth of the proposed dual-mode matched feed for specified reflector antenna.

is shown in Figure 6.7. A small deviation of side lobe region of the secondary pattern is observed in HFSS simulated results as compared to analytical pattern and the same can be seen in the field patterns shown in Figure 6.8. A possible reason for this dieviation is due to the contribution of the remaining x component field component after suppressing the cross-polar component (y component of symmetric pattern) in the application of TM_{11} mode as shown in Figure 6.7. Figure 6.9 and Figure 6.10 show the performance in terms of beam squinting at 6 GHz for the unmatched and matched feed, respectively. The cross polarization and impedance bandwidth are presented in Figure 6.11 and it is observed that a bandwidth of 130 MHz is achieved for -30 dB cross-polar level. It is found that in our design, impedance bandwidth can be easily maintained for wide band of frequencies. However, return

loss gets effected in traditional pin based rectangular matched feed design as mentioned in [6, 86].

6.2 A novel non-regular matched feed structure

In order to generate higher order modes that are to be used for conjugate matching, obstacles such as post or septum are generally kept inside the waveguide at appropriate locations. Usually, such junctions provide constant relative phase difference of the higher order mode with respect to main operating mode in their vicinity. However, it becomes a challenging task to maintain the required relative phase difference of the higher order mode at feed aperture for a wide range of frequencies, as needed in case of wideband conjugate matching. Individual modes propagate with different propagation constant within the waveguide and also they further combine with reflected waves which ultimately change the relative phase difference at feed aperture. However, efforts have been made in recent works to achieve the wideband conjugate matching using circular waveguide. The cross-polar and impedance bandwidth could be enhanced by keeping the two posts in front of aperture and using the quarter wave length matching in case of TE_{21}^1 mode as reported in [5]. A ring choke excited compact dual-mode circular waveguide feed using a slot is introduced in [10] and such design could provide a higher degree of freedom in choosing the dimensions for the wideband operation.

For designing a wideband feed, a possible solution may be to use a proper feed aperture for which cutoff wave numbers of main operating mode and desired higher order mode (used for cross-polar suppression) are very close. In order to achieve the same, a new kind of aperture is proposed that consists of intersection of a rectangular and circular geometry. The shape of the aperture is decided on a trial and error basis using a 2-D FEM for finding the modal solution. For the proposed dual mode feed, the two modes used have close cutoff wave numbers, and the main operating mode has a pattern which is close to TE_{11}^1 mode of circular waveguide, while the other mode pattern is close to a mix of TM_{11} mode of rectangular and TM_{01} mode of circular waveguide. The required mode coefficients and relative phase difference are estimated using PSO for considered system specification. PO is used to calculate the reflector radiation pattern illuminated with the proposed feed configuration. Far field pattern of the feed is evaluated using a semi-analytical technique. The performance of the cross-polar and impedance bandwidth are investigated using HFSS simulator.

The details of the feed configuration and associated modes are presented in the following subsection.

6.2.1 A semi-analytical technique to evaluate the multi-mode radiation pattern of our considered feed aperture

Conventionally, rectangular, circular or elliptical multi-mode horns (both smooth walled and corrugated) are used as the primary feeds for an offset reflector antenna. Such kind of feeds and their design techniques have been dealt extensively in the literature [6, 7]. The estimation and calculation of required multi-mode coefficients and relative phases for such feed aperture to achieve low cross-polarized pattern of offset reflector is generally not difficult due to the availability of analytical solution of Helmholtz equation. However, when an aperture contains a non-regular geometry or a regular geometry for which analytical solution of Helmholtz equation is not available, numerical techniques are required for obtaining the solutions. Several methods such as FEM, MOM, FDM, Rayleigh-Ritz variation method etc can be used. In this study, a 2-D FEM technique is used for the solution of the cutoff wave numbers and scalar potentials for the waveguide geometry used in the design of the multi-mode feed horn under consideration. Detail descriptions on the solution of 2-D Helmholtz equation and calculation of field patterns and cutoff wave numbers of non-regular shape is presented in the Section 3.2. Calculated 2-D FEM based solution of field patterns and cutoff wave numbers are carried out for the evaluation of multi-mode horn radiation patterns, only some important points are added below for this process.

- Axis alignment of the mode solution strictly depends on the meshing and associated geometry. For the geometry considered in our work, any special treatment has not been applied due to the absence of axis non-alignment mode solution.

- The multi-mode power balance radiation pattern of feed with respect to complex coefficient of individual modes has been evaluated using the barycentric subdivision of four-point integration applying into equation (4.57) and (4.58) employing the normalized mode field pattern and their mode impedance.

Table 6.3: First four modes and their cutoff values (k_{c_0}) of our proposed aperture

SLNO.	Mode	Cutoff k_{c_0} $(a = 1\text{m}, \xi = 45^0)$
1	TE_1	1.7188
2	TE_2	2.3413
3	TM_1	2.7691
4	TE_3	3.0866

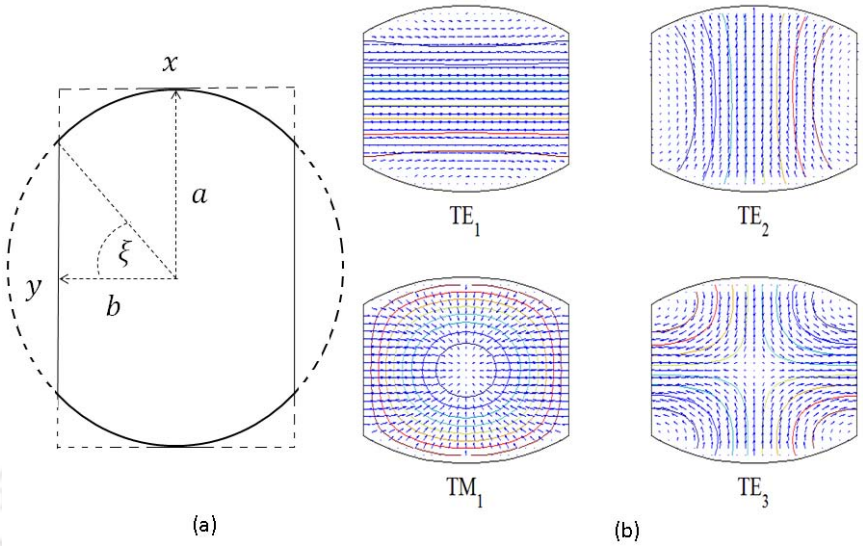

Figure 6.12: (a) Proposed aperture and its dimensions ($b = a\cos\xi$) (b) First four modes field distribution of our proposed feed aperture.

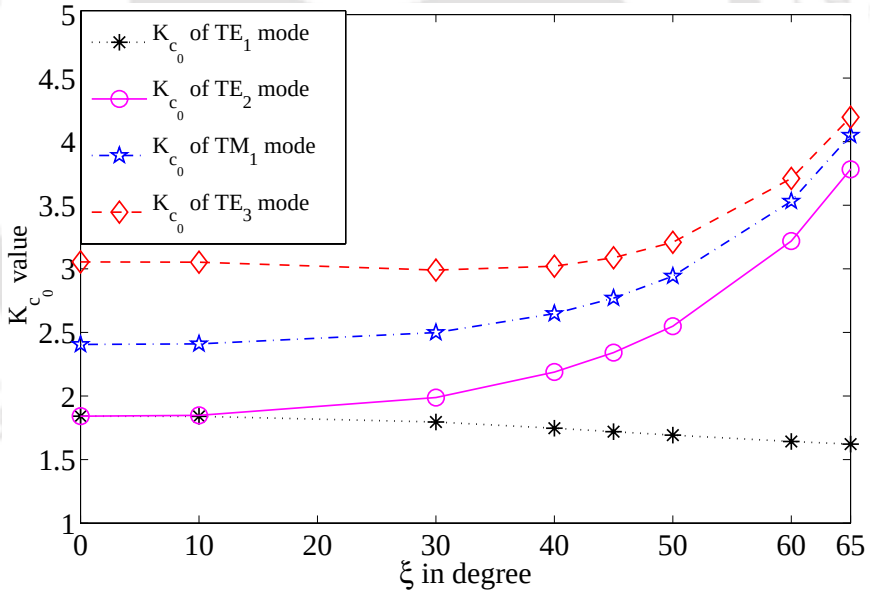

Figure 6.13: Variation of cutoff values (k_{c_0}) of individual modes plotted with respect to ξ for $a = 1$ m.

Our proposed feed aperture which is an intersection of rectangular and a circular geometry, is shown in Figure 6.12 (a). The radius of the circle is a and the rectangle has dimensions $2a \times 2b$; the parameters a and b are related as $b = a\cos\xi$, $0 \leq \xi < \pi/2$. Field patterns computed using 2-D FEM solution of Helmholtz equation are presented in Figure 6.12 (b) for the case $\xi = 45^0$. It can be seen that mode field distributions are of mixed type, TE_1 field distribution is closer to rectangular waveguide TE_{10} mode. TE_2 mode is closer to circular waveguide TE^1_{11} mode. TM_1 is of mixed type,

approximates a combination of rectangular TM_{11} and Circular TM_{01} mode. TE_3 is close to rectangular TE_{11} or circular TE_{21}^1 mode. Similar field distributions are found when a is kept fixed (here a = 1-m) and ξ is varied; only their cutoff values become different, plot of which are shown in Figure 6.13. Choosing a small value of ξ leads to a solution of TM_1 mode which is similar to circular TM_{01} mode. Such mode is not useful in suppressing the cross-polar power of an offset reflector when combined with the main operating TE_2 mode. On the other hand, if we consider larger values of ξ, aperture produces the mismatched far field patterns at E and H plane for TE_2 mode; but TM_1 mode for larger value of ξ behaves as TM_{11} rectangular mode and can suppress the power of the cross-polar field produced by TE_2 mode. Therefore, the value of ξ needs to be chosen appropriately. The computed cutoff value of individual modes of our proposed aperture ($a = 1, \xi = 45^0$) is shown in Table 6.3. The propagation constant of individual modes in case of our considered geometry can be evaluated using the specified k_c values (Table 6.3) employing as $\beta = \sqrt{k_0^2 - {k_c}^2}$, where k_0 is the free space wave number and k_c is the cutoff wave number corresponding to a given radius a and related to k_{c_0} as $k_c = \frac{k_{c0}}{a}$.

6.2.2 A semi-Analytical technique to reduce the cross-polar level in secondary pattern

Feed radiation pattern is found using the earlier mentioned technique and PO is used to study the reflector pattern to obtain the low cross-polar secondary pattern by adding appropriate amount of desired higher order mode. For the proposed feed configuration, TE_2 mode is the main operating mode and TM_1 or TE_3 mode is used for conjugate matching to suppress the cross polarization level. The feed aperture dimension a is chosen in such a way that it supports propagation of those higher order modes at the design frequency (6 GHz). The determination of cutoff values and propagation constants for this modes are already discussed in Section 6.2.1. The feed design has been carried out for the following offset reflector and horn aperture dimension: F = 1 m, D = 1.3 m, offset height H = 0.12 m, $\alpha = 38.8^\circ$ and a = 0.025 m.

It may be pointed out that using semi-analytical technique, the secondary patterns are evaluated for $\phi = [0^0, 5^0, 10^0, ..., 175^0]$. From our study, it is found that maximum cross-polar level occurs at $\phi = 90^0$ and $\phi = 45^0$ respectively, for unmatched and matched feed. Therefore, plots of cross-polar power at 45^0 and 90^0 planes are presented here. The radiation pattern of offset reflector antenna is evaluated for the main operating TE_2 mode at the design frequency (6 GHz) and the performance

Table 6.4: Estimated mode coefficients and relative phases at 6 GHz for the matched feed design and relative performance of different combinations.

Mode	TE_2	TM_1/TE_3	Cross-polar power	
			45°	90°
Case 1:	$1\angle -$	-	−25.6 dB	−23 dB
Case 2:	$0.9495\angle 0°$	$0.3137\angle -87.3°$ (TM_1)	−41.6 dB	−50.5 dB
Case 3:	$0.9253\angle 0°$	$0.3793\angle -85.52°$ (TE_3)	−41.9 dB	−48.3 dB

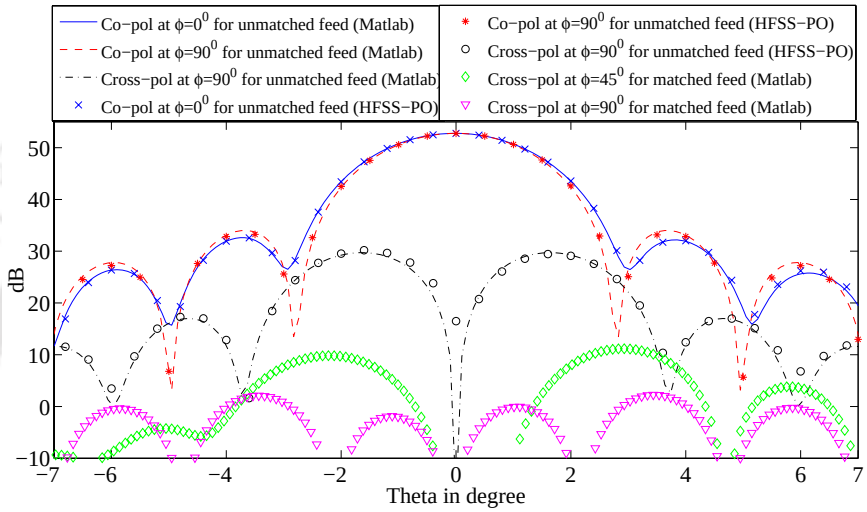

Figure 6.14: Secondary radiation pattern using semi-analytical technique for the unmatched and matched feed at 6 GHz, computed in MATLAB and semi-analytical unmatched feed pattern verified using HFSS.

is shown in Figure 6.14. A high cross-polar power is observed for this unmatched feed and its value is shown in Table 6.4. The performance of cross-polar power using the semi-analytical technique is compared with simulated HFSS result and a close match is obtained as shown in Figure 6.14. It may be noted that the comparison is done for a radiated power of 1 W.

To estimate the mode coefficient and relative phase of TM_1 mode for the $TE_2 + TM_1$ combination used to achieve low cross polarized reflector pattern, a PSO based technique is used. The algorithm of PSO is developed in MATLAB using the techniques already described earlier. It may be noted that PSO uses a fitness function which is directly related to cross-polar level of secondary pattern. TM_1 mode coefficient and relative phase are evaluated using the radiated power balance concept employing PSO technique and those values are enlisted in Table 6.4. The cross-polar level in the secondary pattern reduces to −50.5 dB at $\phi = 90^0$ (as compared to −23 dB for the unmatched case) which is presented in Table 6.4 and the same is also shown in Figure 6.14.

Also, we have investigated the lowering of cross-polar level in secondary pattern for the combination

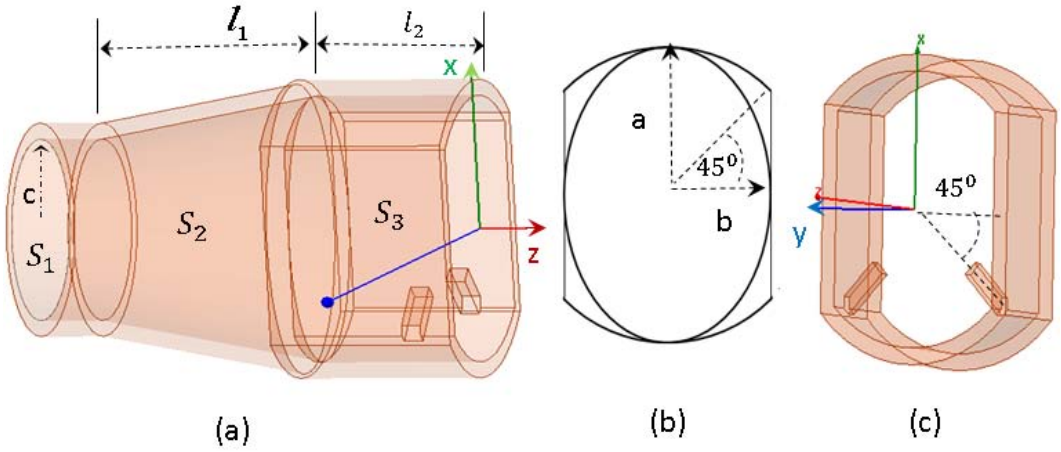

Figure 6.15: (a) Our proposed feed structure: consists of three sections; S_1 is a standard circular waveguide; S_2 is a circular to elliptical transition; S_3 is the proposed waveguide section. All the dimensions $\{a, b, c, l_1, l_2\} = \{25, 17.68, 17, 35, 26\}$ are in mm and the posts are of length × width × height = $3 \times 3 \times 10.3$ mm^3. The posts are located 7 mm behind the aperture. (b) Junction between S_2 and S_3 (c) Section S_3 with Radiating aperture and pins.

of $TE_2 + TE_3$ employing approach similar to $TE_2 + TM_1$ combination. The desired mode coefficients and relative phases are enlisted in Table 6.2. It is observed that the performance of cross-polar level is close to $TE_2 + TM_1$ combination.

6.2.3 Design and Results

Studies using the semi-analytical technique mentioned in Sections 6.2.1 and 6.2.2 leads to design of the proposed matched feed structure. It is observed that the cross-polar performance for TM_1 and TE_3 modes are almost similar. However, use of TM_1 mode provides some advantages in the practical design, as it is suitable to maintain the cross-polar and impedance bandwidth for a wide range of frequencies. Difference between cutoff wave number of TM_1 and TE_2 mode is less. As a result, it is possible to maintain the constant relative phase difference $(-\frac{\pi}{2})$ between TM_1 and TE_2 modes at the aperture. This helps in cross-polar suppression over a wide range of frequencies. The generation of TE_3 mode using a single post is very popular technique [6]. Our proposed technique uses two posts behind the aperture to generate the TM_1 mode and their configurations are shown in Figure 6.15 (c). It may be pointed out that wideband impedance match is difficult when single post is used to generate TE_3 mode.

The proposed structure including all the dimensions is shown in Figure 6.15 (a). The matched feed is realized based on the parametric study performed on some specific dimensions. The proposed

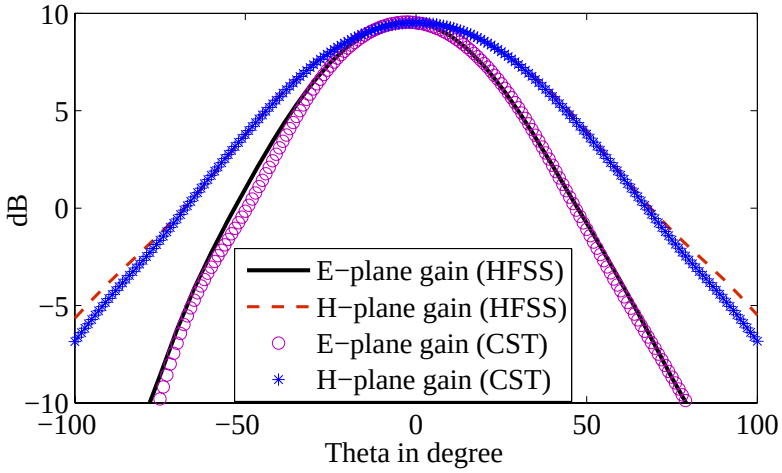

Figure 6.16: Simulated E and H-plane patterns of matched feed at 6 GHz.

matched feed structure consists of three waveguide sections. The first section (S_1) is a standard circular waveguide of radius c. The second section (S_2) is circular to elliptical transition of length l_1. Specifically, the flare surface of this section can be represented by the equation $\frac{x^2}{[c+\frac{z}{l_1}(a-c)]^2} + \frac{y^2}{[c+\frac{z}{l_1}(b-c)]^2} = 1$. The cross-section at $z = 0$ is a circle of radius (c) while at $z = l_1$, the cross section is an ellipse with major and minor axis dimensions $2a$ and $2b$, respectively. The third section (S_3) has a length of l_2 and its cross section is the intersection of circular and rectangular geometries. One end of this section forms a junction with the elliptical waveguide and the other end is the radiating aperture. As mentioned, the higher order TM_1 mode is generated using the two posts which are placed behind the aperture, 135^0 and 225^0 inclined with respect to the x-axis. It may be noted that the back scattered field of TM_1 mode reflects into section S_3 from the junction formed by sections S_3 and S_2 as TM_1 mode is not supported in the S_2 section. On the other hand, such junction easily translates the elliptical TE^x_{11} mode of S_2 to TE_2 mode in S_3 without mismatch of mode impedance. The choice of l_1 effects the impedance bandwidth and length l_2 is chosen close to a quarter wavelength of TM_1 mode at the design frequency. Basically, l_1 maintains impedance matching during the transition of TE^1_{11} circular mode to elliptical TE^1_{11} mode at the end of section S_2. Through a parametric study, height, width, length and position of the posts have been decided to adjust the mode coefficients according to Table 6.4.

E and H-plane patterns of matched feed are simulated in HFSS and CST and the same are shown in Figure 6.16. A close match can be observed between them. The simulated cross-polar performance

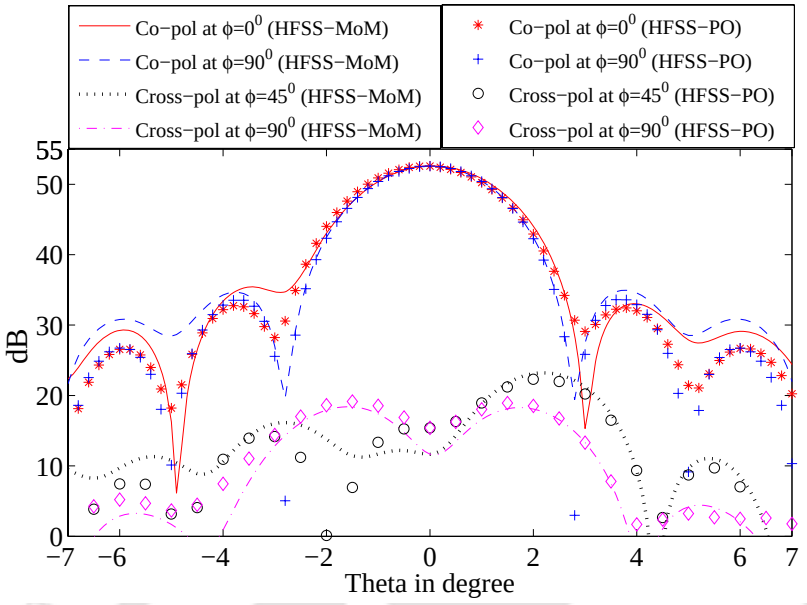

Figure 6.17: Simulated cross-polar performance of secondary pattern in HFSS at 6 GHz for proposed matched feed.

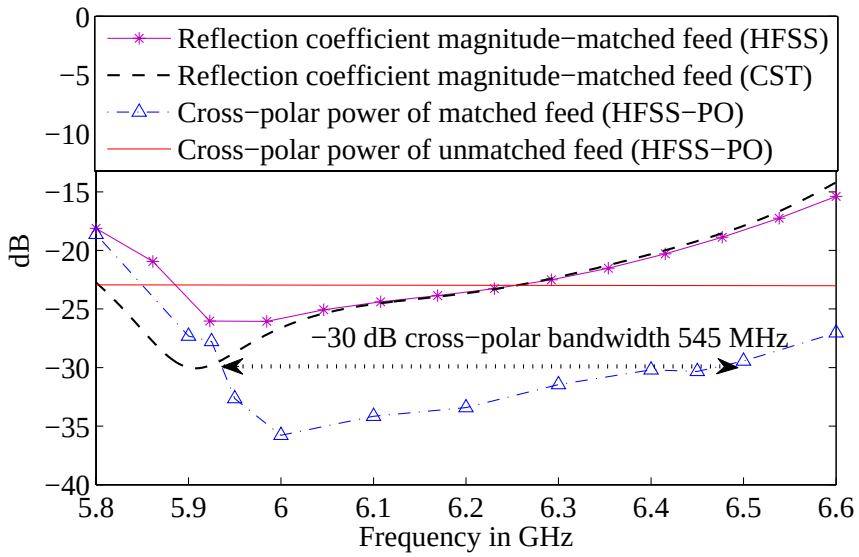

Figure 6.18: Cross-polar and impedance bandwidth of our proposed matched feed structure for the specified reflector dimensions.

in HFSS v15 is shown in Figure 6.17. The cross-polar level is found to be −36 dB, which is close to result obtained through our computed semi-analytical technique. It may be noted that different solvers of HFSS have been used in this study. 3-D FEM module is used for feed modeling and both PO and IE Solver (EFIE-electric field integral equation) are used separately for computation of reflector pattern. Both methods give similar result as shown in Figure 6.17. The cross-polar and impedance

bandwidth are shown in Figure 6.18. A bandwidth of 545 MHz is achieved for −30 dB cross-polar power level and the magnitude of reflection coefficient within this band is below -18.5 dB (using both CAD tools, HFSS and CST).

6.3 A novel dual-mode diagonal matched feed to achieve wide cross-polar bandwidth

For the various matched feed structures reported in literature, in majority of the cases [5–8,10], the depolarization effect is dealt only with x-polarized main operating mode of matched feed or cross-polar suppression of the symmetric plane of an offset reflector antenna (polarization defined with respect to Figure 1.2). It is found in the literature [5–8, 10] that the required conjugate matching mode for an x polarized matched feed can be easily generated from the main operating mode through the use of appropriate choice of junction(s).

While cross-polar suppression of feeds operating with x-polarized main mode is dealt quite exhaustively, both analytically as well as in terms of practical implementation, cross-polar suppression of feeds having y-polarized main mode has been dealt mainly analytically [1]. Feeds supporting both x and y polarized main modes will be useful for frequency reuse and in MIMO systems. Realization of y-polarized matched feed is quite challenging because of the difficulty arises in generating using simple junctions/obstacles the required conjugate matching modes i.e. TE_{02} for rectangular, TE_{21}^2 for circular and HE_{21}^2 for corrugated circular waveguide based feeds and maintaining their magnitudes and phases relative to the main operating modes. Dual polarized feed reported in [11] uses external source to generate conjugating matching modes and uses six SMA connectors to feed power to generate TE_{11}^1/TE_{11}^2 and TE_{21}^1/TE_{21}^2 modes within a circular waveguide. Such arrangements make the system complex and an extra controller unit is needed to feed power.

Wide-band conjugate matched feed is always preferable for mono-pulse radar. For such feeds, the relative phase difference of $-\frac{\pi}{2}$ for the conjugate mode and appropriate mode ratio are required to be maintained over a wide-band of frequencies. Meeting these requirements for wide-band system is often quite challenging. It depends on the choice of junction(s), cut-off of operating modes, selection of aperture, its dimensions as well as on the adopted design methodology. Some of the design methodologies of different matched feed structures to achieve the wide-band conjugate matching can be found in [5, 10, 11].

Diagonal feed, a variant of rectangular waveguide, is introduced as a matched feed in this section. As mentioned earlier, in general, TE_{11}/TM_{11} and TE_{02} modes are used as conjugate modes respectively, for x polarized and y polarized rectangular matched feed. However, the scenario becomes quite different in case of a diagonal feed. It is observed through analytical study that TE_{11}^{D} (same as rectangular TE_{11}) mode can eliminate the depolarization effect of an offset reflector antenna when y polarized TE_{H}^{D} (a linear combination of rectangular TE_{01} and TE_{10}) mode illuminates it as a primary source of excitation. On the other hand, TM_{11}^{D} (same as rectangular TM_{11}) diagonal mode can suppress the cross-polar level when offset reflector is excited with x polarized TE_{V}^{D} (another linear combination of rectangular TE_{01} and TE_{10}) mode. Analytical study is carried out using analytical far-field patterns of operating modes of diagonal feed, PO is used to evaluate the secondary pattern, and PSO to estimate the required mode ratio and relative phase of conjugate matched mode for optimum cross-polar level. Closed form expressions of far-field patterns of diagonal waveguide for TE_{H}^{D}, TE_{V}^{D}, TE_{11}^{D} and TM_{11}^{D} modes are formulated for this purpose. A simple diagonal matched feed is designed to operate with TE_{H}^{D} and TE_{11}^{D} modes. TE_{11}^{D} mode is generated using a rectangular post. Feed design is carried out to meet the objective of wide-band conjugate matching. The performances of cross-polar and impedance bandwidth of our proposed matched feed are investigated using HFSS.

To the best of our knowledge, such diagonal matched feed and its associated modes presented here have not been studied in any earlier literature. Further, the feed geometry is kept very simple, and it can be fabricated easily.

6.3.1 Analytical study to suppress the cross power

As mentioned in Section 5.3, the feed design is carried out through formulation of an analytical model, where PO is used to evaluate the far-field pattern of the offset reflector when it is illuminated by analytical far-field pattern of the feed and PSO is used to estimate the required mode ratio and relative phase of the conjugate matching mode so that the cross-polarization is minimized for the reflector pattern.

Associated modes and cutoff wave numbers of diagonal feed are the analogous of rectangular waveguide modes. Three groups of degenerated modes are found considering the first six modes ($\{TE_{01}, TE_{10}\}$, $\{TE_{11}, TM_{11}\}$, $\{TE_{02}, TE_{02}\}$) when a rectangular waveguide having the same sides ($a \times a$) is used. The calculated values of cutoff wave number of those degenerated modes are $\frac{\pi}{a}$, $\frac{\pi\sqrt{2}}{a}$

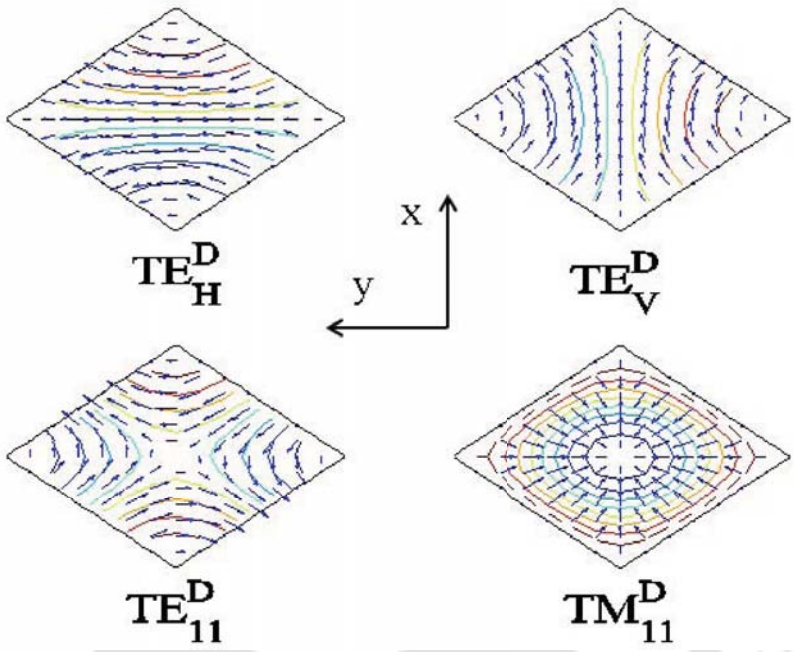

Figure 6.19: First four mode patterns of diagonal waveguide

and $\frac{2\pi}{a}$. Only a few of the mode patterns are found as linear combination of rectangular degenerated modes. The first four mode patterns of diagonal waveguide are shown in Figure 6.19. As observed the patterns of $\{\mathrm{TE}^{\mathrm{D}}_{\mathrm{H}}, \mathrm{TE}^{\mathrm{D}}_{\mathrm{V}}\}$ are linear combination of $\{\mathrm{TE}_{01}, \mathrm{TE}_{10}\}$ rectangular modes, $\{\mathrm{TE}^{\mathrm{D}}_{11}, \mathrm{TM}^{\mathrm{D}}_{11}\}$ are similar to that of $\{\mathrm{TE}_{11}, \mathrm{TM}_{11}\}$ modes, and also next two modes can be found as linear combination of $\{\mathrm{TE}_{02}, \mathrm{TE}_{20}\}$ modes which are not presented here.

$\mathrm{TE}^{\mathrm{D}}_{11}$ diagonal mode has the similar field of asymmetric cross-polar pattern [1] found at focal plane of an offset reflector antenna induced by a linear y polarized field and $\mathrm{TE}^{\mathrm{D}}_{\mathrm{H}}$ field is close to linear y polarized pattern. On this basis, those modes are chosen for the y polarized matched feed. Based on similar kind of reasoning, $\mathrm{TE}^{\mathrm{D}}_{\mathrm{V}}$ and $\mathrm{TM}^{\mathrm{D}}_{11}$ modes can be used for x-polarized diagonal matched feed design.

The closed form expressions of power balanced far-field radiation pattern of multi-mode rectangular horn is found in Section 6.1.1, based on Chu's model. Similarly, the power balanced far-field patterns for $\mathrm{TE}^{\mathrm{D}}_{\mathrm{H}}$, $\mathrm{TE}^{\mathrm{D}}_{\mathrm{V}}$, $\mathrm{TE}^{\mathrm{D}}_{11}$ and $\mathrm{TM}^{\mathrm{D}}_{11}$ modes are formulated based on the concept of linear combination of degenerated modes, considering $\frac{\pi}{4}$ geometrical azimuth angle difference between rectangular and diagonal waveguide and using the far-field expressions as specified of associated modes for rectangular

waveguide. The far-field patterns as considered for different modes are calculated as

$$E_{\theta}^{TE_H^D} = j\frac{V_{TE_H^D}}{\sqrt{\beta_H}}\left(1+\frac{\beta_H}{k}\cos\theta\right)\left(\psi_{10}\sin^2\phi' - \psi_{01}\cos^2\phi'\right)$$

$$E_{\phi}^{TE_H^D} = j\frac{V_{TE_H^D}}{2\sqrt{\beta_H}}\left(\cos\theta+\frac{\beta_H}{k}\right)(\psi_{10}+\psi_{01})\sin 2\phi'$$

$$E_{\theta}^{TE_V^D} = j\frac{V_{TE_V^D}}{\sqrt{\beta_V}}\left(1+\frac{\beta_V}{k}\cos\theta\right)\left(-\psi_{10}\sin^2\phi' - \psi_{01}\cos^2\phi'\right)$$

$$E_{\phi}^{TE_V^D} = j\frac{V_{TE_V^D}}{2\sqrt{\beta_V}}\left(\cos\theta+\frac{\beta_V}{k}\right)(-\psi_{10}+\psi_{01})\sin 2\phi'$$

$$E_{\theta}^{TE_{11}^D} = \frac{\sqrt{2}V_{TE_{11}^D}}{\sqrt{\beta_{11}^E}}\left(1+\frac{\beta_{11}^E}{k}\cos\theta\right)\psi_{11}\cos 2\phi'$$

$$E_{\phi}^{TE_{11}^D} = -\frac{\sqrt{2}V_{TE_{11}^D}}{\sqrt{\beta_{11}^E}}\left(\cos\theta+\frac{\beta_{11}^E}{k}\right)\psi_{11}\sin 2\phi'$$

$$E_{\theta}^{TM_{11}^D} = -\frac{\sqrt{2}V_{TM_{11}^D}}{a^4\sqrt{\beta_{11}^M}}\left(\cos\theta+\frac{\beta_{11}^M}{k}\right)\psi_{11}$$

$$E_{\phi}^{TM_{11}^D} = 0$$

where $\psi_{mn} = G\frac{\sin c\left(\frac{ka\sin\theta\cos\phi'+m\pi}{2}\right)\sin c\left(\frac{ka\sin\theta\sin\phi'+n\pi}{2}\right)}{(ka\sin\theta\cos\phi'-m\pi)(ka\sin\theta\sin\phi'-n\pi)}$, $G = \frac{a^2k^2e^{-jkR}}{2R}\sqrt{\frac{k\eta}{2}}\sin\theta$ and $\phi' = \phi - \frac{\pi}{4}$. Here, R, θ and ϕ are the observation point of far-field. $V_{TE_H}^D$, $V_{TE_V}^D$, $V_{TE_{11}}^D$ and $V_{TM_{11}}^D$ are respectively, complex mode coefficient of $\mathrm{TE_H^D}$, $\mathrm{TE_V^D}$, $\mathrm{TE_{11}^D}$ and $\mathrm{TM_{11}^D}$ modes. β_H, β_V, β_{11}^E and β_{11}^M represent propagation constant of $\mathrm{TE_H^D}$, $\mathrm{TE_V^D}$, $\mathrm{TE_{11}^D}$ and $\mathrm{TM_{11}^D}$ modes. k is free space wave number and (a) represents the edge length of diagonal feed as mentioned.

The design of diagonal matched feed is carried out for the **C**-band ($5.85 - 8.2$ GHz). Edge length a of diagonal feed is decided based on the cutoff value ($\frac{\pi}{a}$, $\frac{\pi\sqrt{2}}{a}$, $\frac{2\pi}{a}$) of $\mathrm{TE_H^D}$, $\mathrm{TE_{11}^D}$ and next higher diagonal modes. It is found that $a = 37$ mm is sufficient for propagation of $\mathrm{TE_H^D}$, $\mathrm{TE_{11}^D}$ modes and to stop propagation of next higher diagonal modes within **C**-band. So, $a = 37$ mm is used for the analytical study and simulating of matched feed performances.

The matched feed design is carried out for an offset reflector configuration having dimensions as follows: focal length $(F) = 1$ m, diameter $(D) = 1.3$ m, tilt angle $(\alpha) = 38.8^{\circ}$ and offset height $(H) = 0.12$ m. The cross-polar performance of this considered reflector for $\mathrm{TE_H^D}$ as main operating mode is evaluated using the developed analytical technique for a radiated power of 1 W, which is shown in Figure 6.20 and its cross-polar level is also mentioned in Table 6.5. The performance of our

developed analytical technique is evaluated by comparing analytical results with simulated result of HFSS as shown in Figure 6.20 and a close match is observed.

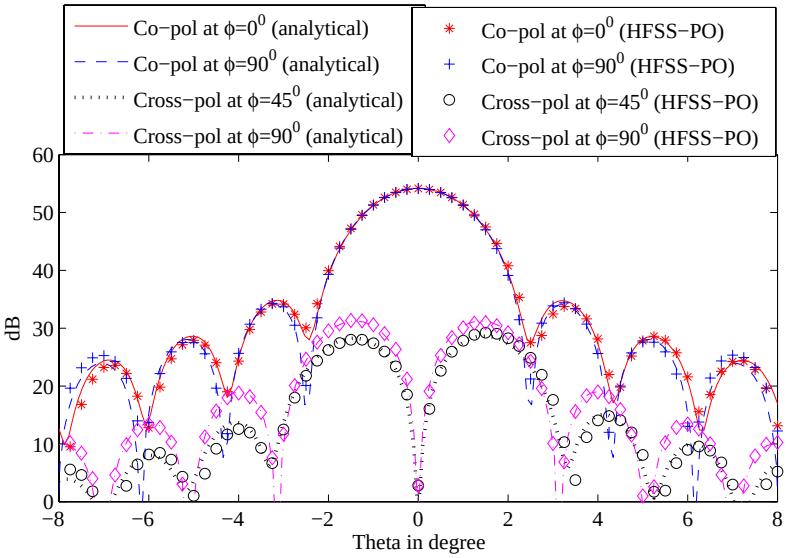

Figure 6.20: The study of TE_H^D mode performance for considered offset reflector in 7 GHz using analytical technique and HFSS (3D-FEM+PO)

Table 6.5: Cross-polar performance of y polarized unmatched and matched feed and its mode coefficients at 7 GHz.

Mode	TE_H^D	TE_{11}^D	Cross-polar power	
			45°	90°
Case 1:	$1\angle -$	-	−24.7 dB	−22.9 dB
Case 2:	$0.9584\angle 0°$	$0.2853\angle -89.9°$	−35 dB	−47 dB

Table 6.6: Cross polar performance of x polarized unmatched and matched feed and its mode coefficients at 7 GHz.

Mode	TE_V^D	TM_{11}^D	Cross-polar power	
			45°	90°
Case 3:	$1\angle -$	-	−26.2 dB	−23.4 dB
Case 4:	$0.9604\angle 0°$	$0.2785\angle -88.2°$	−35.1 dB	−54 dB

To suppress the cross-polar power induced by TE_H^D mode for the considered offset reflector, a PSO based optimization technique [77] is used to estimate the required mode coefficient and relative phase of conjugate matched TE_{11}^D mode. Evaluated mode coefficient and relative phase of conjugate matched mode are given in Table 6.6 and its performance is shown in Figure 6.21.

Similarly, the performance in case of TE_V^D as main operating mode is also investigated using the

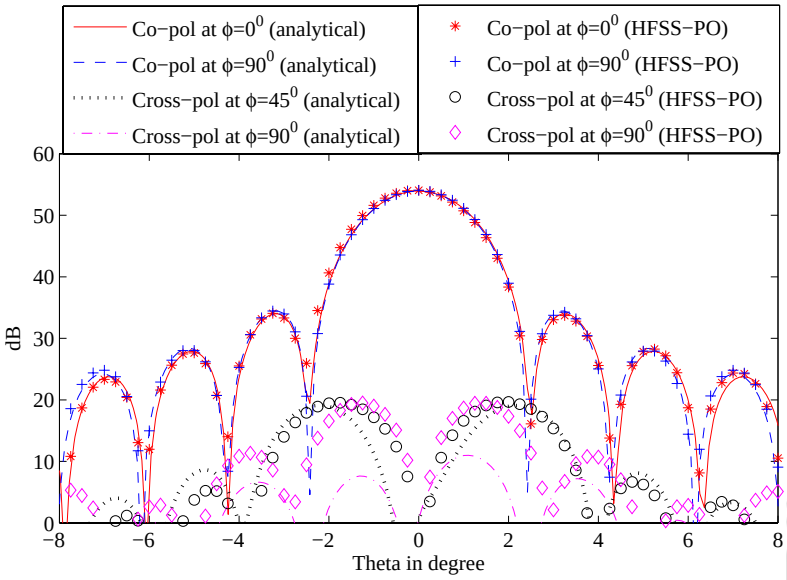

Figure 6.21: Optimum cross-polar level of ideal matched feed (analytical) and our proposed structure (HFSS) at 7 GHz.

specified technique and its cross-polar level is given in Table 6.5. Required mode coefficient and relative phase of TM_{11}^{D} conjugate mode is estimated for optimum cross-polar level of our considered reflector system using PSO technique and values are specified in Table 6.6.

It may be pointed out that in our study, cross-polar pattern is evaluated for $\phi = [0^0, 5^0, 10^0, ..., 175^0]$ and it is found that maximum cross-polar power is located at angles $\phi = \{45^0, 90^0\}$ for matched and unmatched feed, respectively. So, in this Section, the cross-polar performances are only presented for $\phi = \{45^0, 90^0\}$. Further, it may be noted that in the analysis of feed and reflector using HFSS, 3D-FEM is used for feed and PO is used for reflector.

6.3.2 Feed Design and Measured Results

This sub-section provides the details of feed structure which generates the required modes and also how the broadband cross-polar performance is achieved. Our proposed matched feed structure, including all the dimensions is shown in Figure 6.22(a). A **C**-band circular waveguide having radius 16.256 mm operated with TE_{11}^{2} mode is used as a source to generate the TE_{H}^{D} diagonal mode. Matching of such junction between circular and diagonal waveguide (without post) for the conversion of TE_{11}^{2} to TE_{H}^{D} is investigated in case of open ended waveguide and the magnitude of reflection coefficient is found to be quite acceptable for the **C**-band application as shown in Figure 6.23. The junction suitable

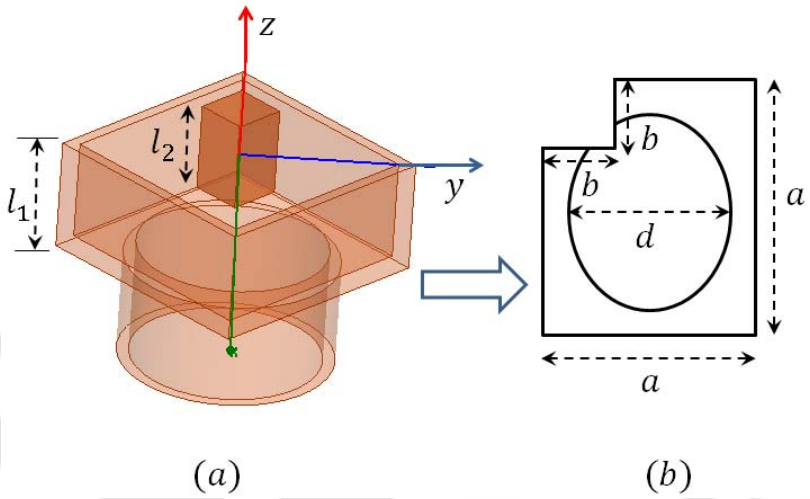

Figure 6.22: Our proposed feed structure and its dimensions: $\{a,\ l_1,\ l_2,\ b,\ d\} = \{37,\ 17,\ 15,\ 9,\ 32.512\}$ mm; (a) matched feed; (b) junction between circular and diagonal waveguide in presence of post.

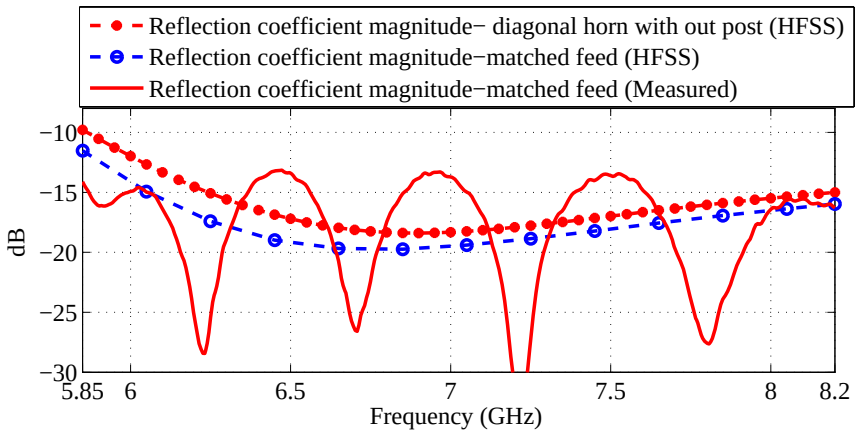

Figure 6.23: Reflection coefficient magnitude of matched feed for presence of post and without post.

for generation of TE_{11}^{D} mode is finalized after studying the performance of a number of junctions using HFSS.

Conventionally, generation of TE_{11} mode in rectangular waveguide is done using a post [6]. As mentioned in the literature, the post is located in the direction of the maximum electric field of TE_{01} mode and it shorts this field to generate the TE_{11} mode. Generally, such junction degrades the return loss. But, behavior of such junction in case of diagonal waveguide is quite different in comparison of rectangular junction as observed in our studies. When a post is kept in the direction of electric field of TE_{H}^{D} ($-y$ axis), it generates the TM_{11}^{D} mode. On the other hand, it is found that TE_{11}^{D} mode is generated when post is kept in the $-x$ axis. Further, it is found that when such post is kept in the vicinity of the junction formed by circular and diagonal waveguide to generate the conjugate matching mode TE_{11}^{D}, it also improves the return loss.

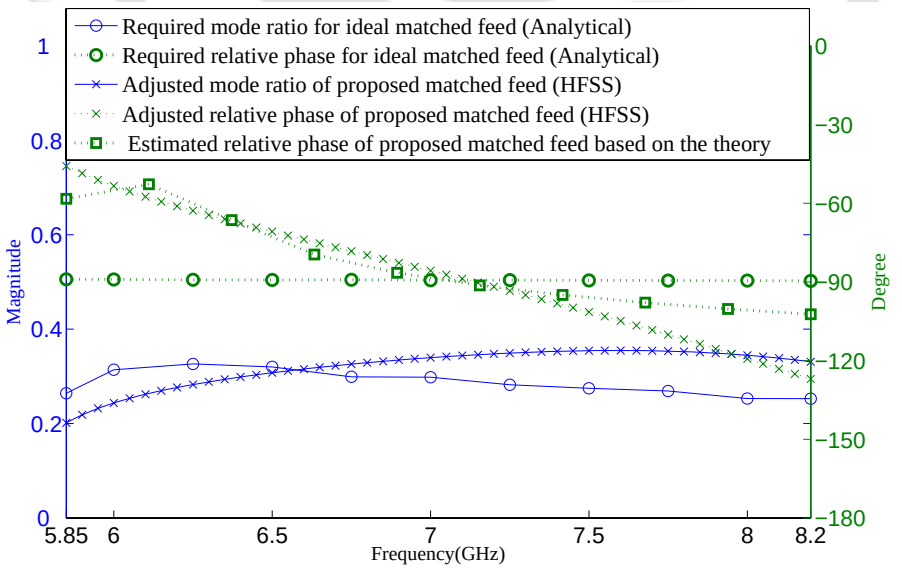

Figure 6.24: Estimated mode coefficients and relative phases for optimum cross-polar pattern using analytical technique and adjusted mode coefficients and relative phases of our design over a wide-band of frequencies.

As per our understanding, this improvement is observed due to reduction of the mismatch of impedance between main operating mode TE_{11}^{2} (circular mode) and a mode very close to TE_{H}^{D} mode over the post region (TE_{H}^{DP}) as compared to TE_{11}^{2} and TE_{H}^{D} (diagonal mode). It is also observed that a desired amount of a mode having pattern close to TE_{11}^{D} mode over the post area (TE_{11}^{DP}) is generated at the vicinity of the junction and it has a extra relative phase of $-\frac{3\pi}{4}$ with respect to TE_{H}^{DP} mode. Phase difference between TE_{11}^{DP} and TE_{H}^{DP} modes increases as they reach the other end of the post because the two modes have different propagation constants. At the discontinuity between the

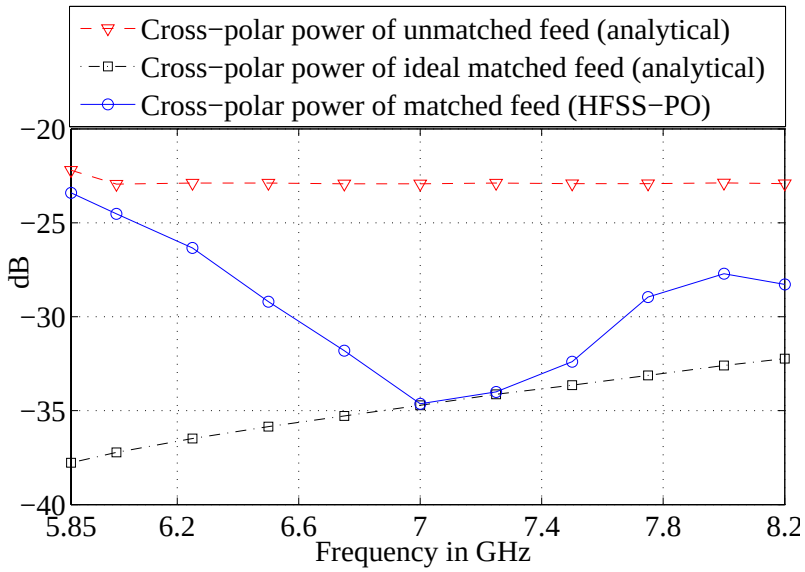

Figure 6.25: Maximum cross-polar power for our proposed matched feed using HFSS and ideal case using analytical technique.

end position of post and diagonal waveguide (located near the aperture as shown in Figure 6.22(a)), TE_{11}^{DP} is converted to TE_{11}^{D}. On the other hand, TE_{H}^{DP} at this discontinuity give rise to TE_{H}^{D} and TE_{11}^{D} modes. The magnitude of this generated TE_{11}^{D} component is small and has a phase different respect to TE_{11}^{D} mode converted from TE_{11}^{DP}. Both of TE_{11}^{D} components combine and overall magnitude of TE_{11}^{D} mode can increase based on the relative phases of the two components. Finally, TE_{H}^{D} and TE_{11}^{D} modes travel towards the aperture of diagonal waveguide with different propagation constants. It is observed that the relative phase of TE_{11}^{D} depends on the choice of l_1, b and l_2. On the other hand, mode ratio depends on the choice of dimensions b and l_2. The flexibility of choice of dimensions to maintain the relative phase and mode ratio of TE_{11}^{D} for conjugate matching is used to achieve for wide-band operation. Based on our understanding, the estimated relative phase of the conjugate mode is shown in Figure 6.24 for the design band and also compared with adjusted relative phase with HFSS simulated results of our proposed matched feed for the deciding parameters.

Using analytical technique (PO + PSO + analytical feed pattern) as mentioned in earlier Section, required mode ratios and relative phases of conjugate matching mode in C-band are calculated for the considered reflector antenna over a wide-band of frequencies. Figure 6.24 shows those values of required mode ratios and relative phases of conjugate matching mode of an ideal matched feed. The optimum cross-polar power using these estimated values of TE_{11}^{D} mode is calculated employing

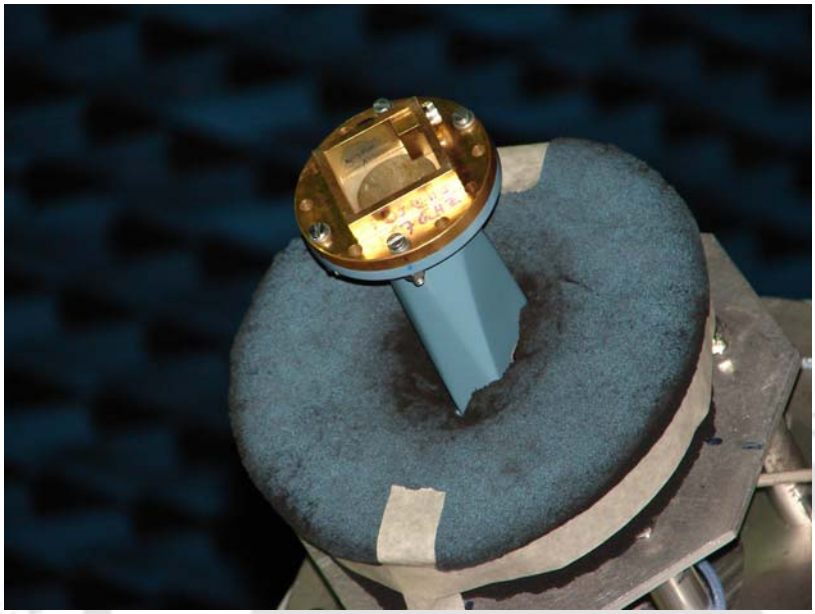

Figure 6.26: A figure of prototype matched feed structure during the measurement of far field patterns in an anechoic chamber.

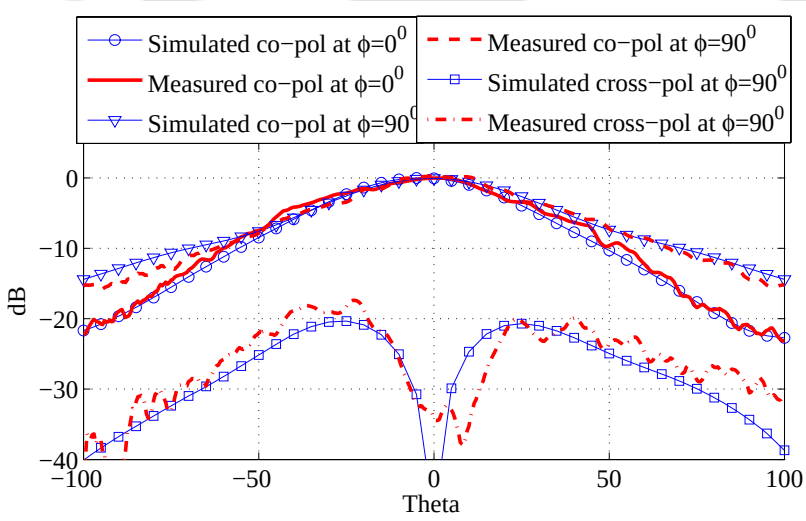

Figure 6.27: Primary cross-polar level (simulated and measured) of the proposed matched feed at 7 GHz.

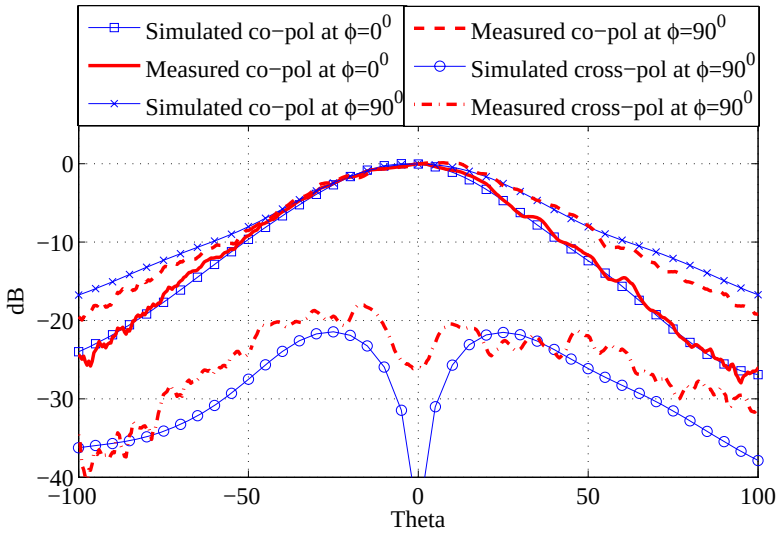

Figure 6.28: Primary cross-polar level (simulated and measured) of the proposed matched feed at 7.5 GHz.

our developed analytical technique and maximum cross-polar level (ideal matched feed) is shown in Figure 6.25. Height (l_1) of diagonal waveguide and dimensions (b, l_2) of post are decided based on a parametric study in HFSS to adjust the analytical estimated values of TE_{11}^{D}. Figure 6.23 shows the performance improvement of reflection coefficient of our designed matched feed as compared to the feed without any matching post. The performance of cross-polar pattern for the proposed matched feed using HFSS is calculated and its pattern at 7 GHz is shown in Figure 6.21 while maximum cross-polar power for **C**-band is shown in Figure 6.25.

A prototype matched feed structure is fabricated and it is shown in Fig. 6.26. It may be noted that an adapter (coaxial cable to WR-137) and one transition (WR-137 to WC-128) are used to feed the power to the prototype for the verification of its performances. The measured reflection coefficient magnitude, and far-field patterns at 7, and 7.5 GHz of our matched feed are shown in Figure 6.23, 6.27 and 6.28 respectively, also compared with simulated HFSS results and close agreements are obtained.

6.4 Conjugate field radiated from a square choke excited by two slots on a diagonal waveguide

It is found in the literature that presence of choke in front of horn can improve the radiation characteristic of reflector. However, very limited works have been published on design of matched feed

using the choke. In an interesting work, a multi-ring structure in front of a coaxial feed employing appropriate multi-modes, has been designed by Koch [87] to improve the aperture efficiency and spill-over of parabolic reflector. In another recent work, a ring choke is used to radiate the conjugate TE^1_{21} mode and central circular waveguide emits main operating mode TE^1_{11}, is proposed in [10] as a matched feed for wideband system.

In this Section, a square choke is proposed for the design of a diagonal matched feed as illustrated in Figure 6.29. For the matched feed proposed in this Section, a semi-analytical technique as specified in Section 5.3 is used to investigate the performance of a given offset reflector. It may be noted that PO is used in this framework for the observation of reflector pattern. Analytical far-field patterns of main operating modes (TE^D_H, TE^D_V) of diagonal horn as found in Section 6.3.1 are used for this semi-analytical study. Associated modes of square choke is calculated based on 2-D FEM technique. Normalized numerical far-field patterns of conjugate modes present at the square choke as TE_3 and TE_4 (rectangular higher order coaxial modes) are calculated based on the treatment as specified in Section 3.2. Conjugate mode TE_3 for TE^D_H operating mode and TE_4 for TE^D_V as the main diagonal mode are used for obtaining the low cross-polar pattern of reflector. The mode pairs are chosen based on our study using the semi-analytical technique developed for this purpose. The required relative phases and mode coefficients for the chosen pair of modes at the design frequency are calculated based on the study using PSO to ensure the low cross-polar pattern for the considered reflector. Further, finer adjustments in matched feed design is carried out through the parametric study in HFSS and using a proper junction. Our design is implemented based on the operating modes TE^D_V and TE_4. Using two identical longitudinal slots, TE_4 mode is generated inside the square choke which is shown in Figure 6.29. Such kind of design has the advantage that it is very easy to maintain the wideband conjugate matching as well as impedance bandwidth.

To the best of our knowledge, such kind of matched feed structure and associated modes of such feed aperture have not been studied in any kind of literature. Also, the proposed matched feed structure is simple, and it is expected that it will find widespread application in future considering its ability to maintain the wideband conjugate matching and impedance bandwidth.

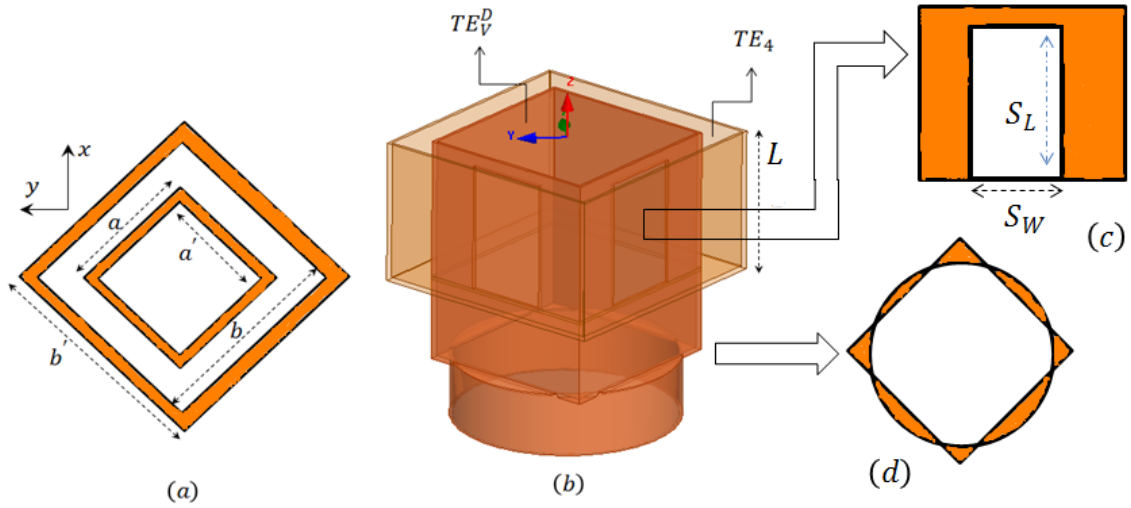

Figure 6.29: (a) Aperture: $\{a',\ a,\ b,\ b'\} = \{26,\ 29,\ 35,\ 43\}$ mm. (b) Proposed matched feed structure: $L = 22$ mm. (C) Slot:$\{S_L,\ S_W\} = \{20,\ 12\}$ mm. (d) Junction between standard circular waveguide (diameter 32.512 mm) and diagonal waveguide.

6.4.1 Feed Geometry and Operated modes

The design of matched feed is carried out for J-band ($5.85 - 8.2$ GHz). The feed structure, which is considered for study, is shown in Figure 6.29. It consists of mainly three parts. First part is J-band standard circular waveguide WC-128 which is operated in circular TE_{11}^{1} mode to supply the power into second part. Second part is a inner diagonal waveguide; its one side is connected with standard circular waveguide and other side is open ended which is used to radiate the $\mathrm{TE}_{\mathrm{V}}^{\mathrm{D}}$ mode. Side a' of inner diagonal waveguide as specified in Figure 6.29, is chosen based on the cutoff value $\frac{\pi}{a'}$ of $\mathrm{TE}_{\mathrm{V}}^{\mathrm{D}}$ operating mode. Side a' is chosen to be 26 mm so that the guide operates only in $\mathrm{TE}_{\mathrm{V}}^{\mathrm{D}}$ mode approximately over the desired band of 5.85 to 8.2 GHz. Two identical longitudinal slots are used to excite the third section which is basically another outer diagonal waveguide looking like a choke as shown in Figure 6.29. Such longitudinal slots are utilized to generate a higher order rectangular coaxial mode (TE_4) inside the choke. Moreover, it is found through semi-analytical study that use of such higher order rectangular coaxial mode has the ability to suppress the cross-polar level of offset reflector antenna. Section 6.4.2 presents this study in detail. Main advantage of the proposed scheam is that such kind of junction generates the relative phase of conjugate mode as required for conjugate matching and also the desired mode coefficient of TE_4 can be easily adjusted through the parametric study by varying the slots length (S_L) and width (S_W). It may be noted that the identical slots are

only used to generate TE_4 mode in the square choke. Otherwise, other higher order modes will appear with TE_4 mode which may degrade the performance of matched feed.

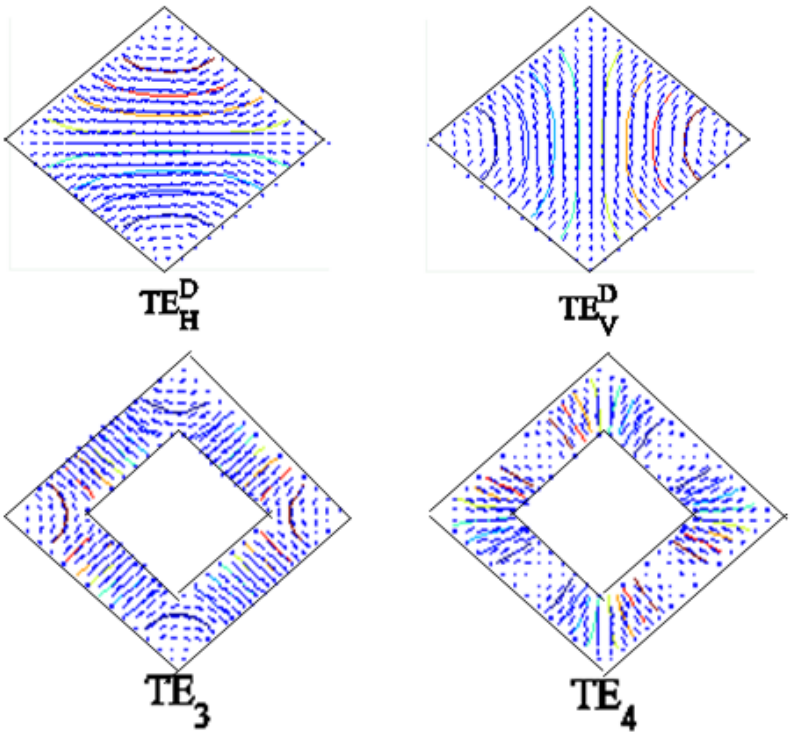

Figure 6.30: Operated modes pattern.

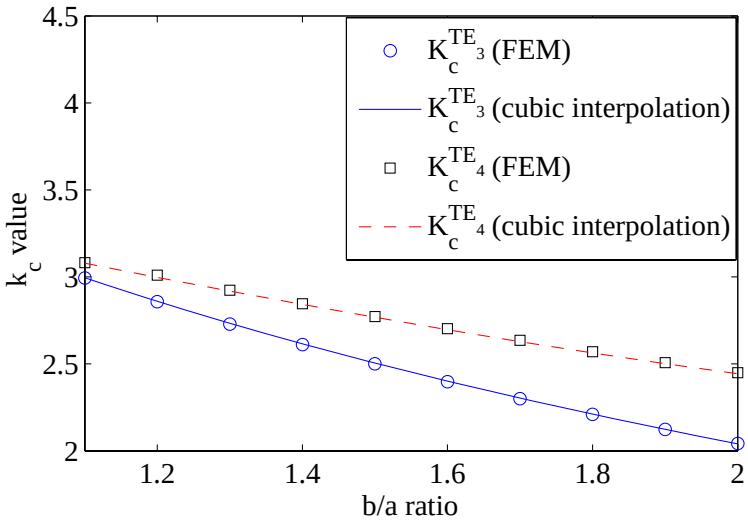

Figure 6.31: Cut-off of conjugate modes.

As discussed earlier, total radiated far field of matched feed is a summation of the fields of two

modes which are excited from two separate apertures (illustrative drawing of aperture is shown in Figure 6.29 (a)). It is well known that associated modes of diagonal horn are analogous to rectangular modes. If we consider first four modes in the analytical solution of Helmholtz equation, two groups of degenerated modes are found. First group is $\{\mathrm{TE}_{\mathrm{V}}^{\mathrm{D}},\ \mathrm{TE}_{\mathrm{H}}^{\mathrm{D}}\}$ having cutoff $\frac{\pi}{a'}$ and its field distributions are shown in Figure 6.30. Second group is similar to rectangular TE_{11} and TM_{11} modes having cutoff $\frac{\pi\sqrt{2}}{a'}$. Other aperture as specified as a square choke has the analogous modes of rectangular coaxial cable as the solution of Helmholtz equation. Generally, exact analytical solution is not available for such aperture. However, some approximated solutions are found in [88, 89]. For the sake of accuracy, solution of this aperture is carried out using 2-D FEM technique using the same treatment as specified in Section 3.2. First mode is a TEM mode and after that four TE modes appear according to cutoff value in this solution. Second and third modes are odd mode having the similar pattern of rectangular TE_{01} and TE_{10} mode, respectively. Our interest is only for conjugate matching modes which appear in fourth (TE_3) and fifth (TE_4) positions and its field distributions are shown in Figure 6.30. Calculated cutoff values using the mentioned numerical technique for such modes with respect to $\frac{b}{a}$ ratios (related to dimensions of such geometry) are plotted in Figure 6.31. Some approximated equations are derived using cubic interpolation technique employing the cutoffs of FEM solution for such modes. The cubic interpolated equations are given below.

$$k_c^{\mathrm{TE}_3} = -0.12\frac{b^3}{a^4} + 0.88\frac{b^2}{a^3} - 2.9\frac{b}{a^2} + \frac{5.28}{a}$$

$$k_c^{\mathrm{TE}_4} = 0.045\frac{b^3}{a^4} - 0.064\frac{b^2}{a^3} - 0.84\frac{b}{a^2} + \frac{4.02}{a}$$

To observe the accuracy of our derived equations, they are compared with exact solution based on FEM technique and comparisons are shown in Figure 6.31. The derived equations are very useful to predict cutoff values of those modes.

The dimensions of our considered feed aperture are decided based on the cutoff value of operating modes. As mentioned, the arm's length a' of inner diagonal waveguide is based on the cutoff of main operating mode. On the other hand, the dimensions a and b of square choke are chosen based on the physical reliability as well as having the cutoff value of TE_4 close to $\mathrm{TE}_{\mathrm{V}}^{\mathrm{D}}$ mode cutoff value $\frac{\pi}{a'}$. As we discuss, TE_4 mode is generated inside the square choke by slots and it provides the required conjugate phase in the vicinity of junction within the design band. It may be noted that a extension

length of waveguides ($L - S_L$; as shown in Figure 6.29) from the end point of junctions (longitudinal slots) are required for the stability of generated TE_4 mode. To avoid the change of the relative phase of TE_4 mode for this extended length, cutoff value of TE_4 is fixed closed to TE_V^D mode by the choice of dimensions b and a. On this basis, a', a, and b are decided for J band matched feed design.

6.4.2 Semi-analytical study to reduce the cross-polar level of offset reflector

As mentioned earlier, the performances of associated modes of proposed feed are investigated using a semi-analytical technique. This technique is developed based on the PO to investigate the reflector pattern and multi-mode approximated feed pattern are used as a source for reflector. Here, feed pattern is considered as the combination of analytical and numerical far-field patterns of the associated modes of specified apertures. The closed-form expressions for the analytical mode field patterns of main operating modes TE_V^D and TE_H^D of center diagonal waveguide are given in Section 6.3.1. The conjugate mode patterns of specified TE_3 and TE_4 modes which get radiated from square choke are calculated based on the numerical technique as given in Section 3.2.

Generally, most crucial planes to observe the cross-polar level of secondary pattern are at $\phi = \{45^0,\ 90^0\}$ for matched and unmatched cases, respectively. However, the cross-polar levels have been investigated for $\phi = \{0^0,\ 5^0,\ 10^0,\ .....175^0\}$. It may be noted that power balance of far-field pattern of feed is maintained and 1 W power is considered while investigating the reflector pattern in this semi-analytical study.

The cross-polar performance of reflector for main operating mode TE_H^D for a considered offset reflector having diameter 1.3 m, focal length 1 m and offset height 0.12 m is investigated at 7.5 GHz using our developed semi-analytical technique and its cross-polar level is specified in Table 6.7 as well as its cross-polar patterns are shown in Figure 6.32. To verify the developed code, TE_H^D mode performance is investigated for same reflector using HFSS-15 and the obtained results are compared with the results of our semi-analytical technique which is shown in Figure 6.32. As expected, almost similar results are found for both cases. It may be pointed out that 3D-FEM and PO are used in HFSS-15 to evaluate the feed pattern and reflector pattern, respectively. To suppress the high level of cross-polar power, TE_3 mode is used with the specified main operating mode and PSO optimization technique is used to estimate the required mode coefficient and relative phase of conjugate mode. Significant improvement of cross-polar levels are found and their values and required mode coefficients

are presented in Table 6.7.

Table 6.7: Cross-polar performance of y polarized unmatched and matched feed and its mode coefficients at 7.5 GHz.

Mode	TE_H^D	TE_3	Cross-polar power	
			45°	90°
Case 1:	$1\angle -$	-	−26.1 dB	−22.85 dB
Case 2:	$0.9417\angle 0°$	$0.3365\angle -89.33°$	−38.62 dB	−43.12 dB

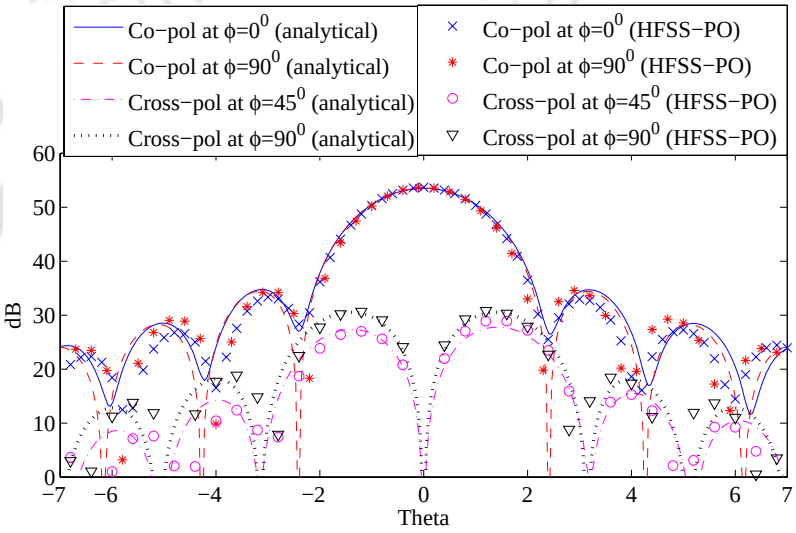

Figure 6.32: Cross-polar performance of y polarized unmatched feed at 7.5 GHz.

Similarly, x polarized main operating TE_V^D mode is studied for same reflector using the developed semi-analytical technique as well as HFSS-15. The obtained patterns for both cases are presented in Figure 6.33 and close agreements are found. Also, the cross-polar levels are presented in Table 6.8. As mentioned, TE_4 mode is used to cancel the cross-polar power of considered reflector for the main operating TE_V^D mode. The estimation of required conjugate mode coefficient and its relative phase are given in Table 6.8 which are calculated by PSO technique. For this case, the optimum cross polar levels are specified in Table 6.8. The obtained cross-polar patterns are shown in Figure 6.34.

Table 6.8: Cross polar performance of x polarized unmatched and matched feed and its mode coefficients at 7.5 GHz.

Mode	TE_V^D	TE_4	Cross-polar power	
			45°	90°
Case 3:	$1\angle -$	-	−26.53 dB	−23.24 dB
Case 4:	$0.8735\angle 0°$	$0.4868\angle -91.9°$	−42.68 dB	−44.24 dB

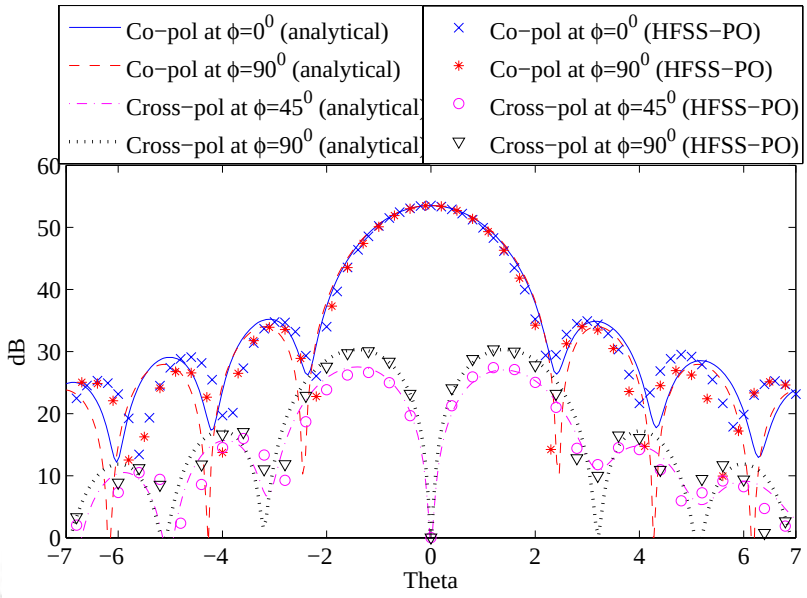

Figure 6.33: Cross-polar performance of x polarized unmatched feed at 7.5 GHz.

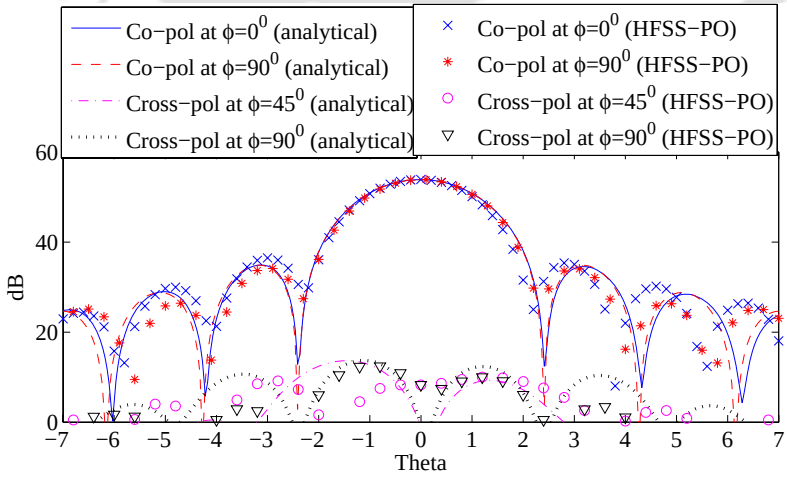

Figure 6.34: Optimum cross-polar level of ideal matched feed (analytical) and our proposed structure (HFSS) at 7.5 GHz.

As observed, the cross-polar performances at secondary pattern of the both cases $TE_H^D + TE_3$ and $TE_V^D + TE_4$ are quite similar. But, for practical realization of matched feed, the TE_4 mode at the square choke can be easily generated using the primary source of diagonal TE_V^D mode. Moreover, our proposed structure as discussed in Section 6.4.1 has the ability to maintain the required relative phase as well as impedance matching for wideband of frequencies.

6.4.3 Final Simulation and Measured Results

The preliminary design of the feed is carried out using semi-analytical technique described in the previous section while fine tuning of the feed parameters are carried performing parametric study in HFSS-15. As discussed, two symmetric longitudinal slots as illustrated in Figure 6.29 are used to generate TE_4 mode. Slot length (S_L) and width (S_W) are fixed on the basis of adjusting conjugate mode coefficient as specified in Table 6.8 at the design frequency. Simultaneously, the waveguide length (L) is decided to adjust the relative phase of conjugate mode of our proposed matched feed. Finally, a fine tuning on crucial parameters ($L,\ S_L,\ S_W$) of feed is carried out using HFSS-15 to obtain proper matching with the reflector. The process of fine tuning involves varying the crucial dimensions which effect the cross polar performance of the reflector so as to obtain lowest cross polar power at the design frequency. While carrying out the fine tuning using HFSS-15. Feed pattern is evaluated using 3D FEM and reflector pattern using PO module.

After fine tuning, the adjusted feed dimensions are shown in Figure 6.29. The cross-polar performance of our proposed matched feed structure is shown in Figure 6.34. It can be seen that the patterns computed using our semi analytical technique match with the patterns obtained using HFSS. The adjusted mode ratio and relative phase of TE_4 mode at the feed aperture are given in Figure 6.35.

A prototype matched feed structure is fabricated and it is shown in Fig. 6.36. It may be noted that an adapter (coaxial cable to WR-137) and one transition (WR-137 to WC-128) are used to feed the power to the prototype for the verification of its performances.

Fig. 6.37 presents the simulated and measured magnitude of reflection coefficient of the matched feed. A close match is observed between them. The simulated cross-polar performance of the reflector antenna system for unmatched and matched conditions are shown in Fig 6.37.

The measured result of co-polar and cross-polar patterns of the matched feed at the selective planes

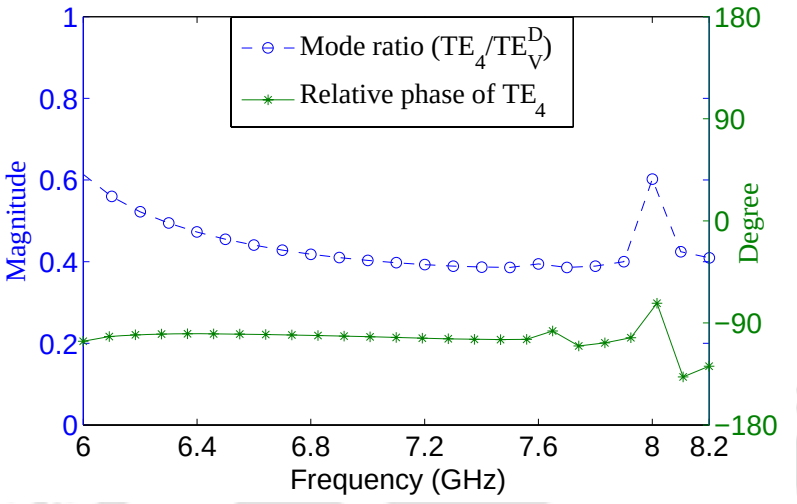

Figure 6.35: Adjusted mode ratio and relative phase of TE_4 mode of our proposed matched feed.

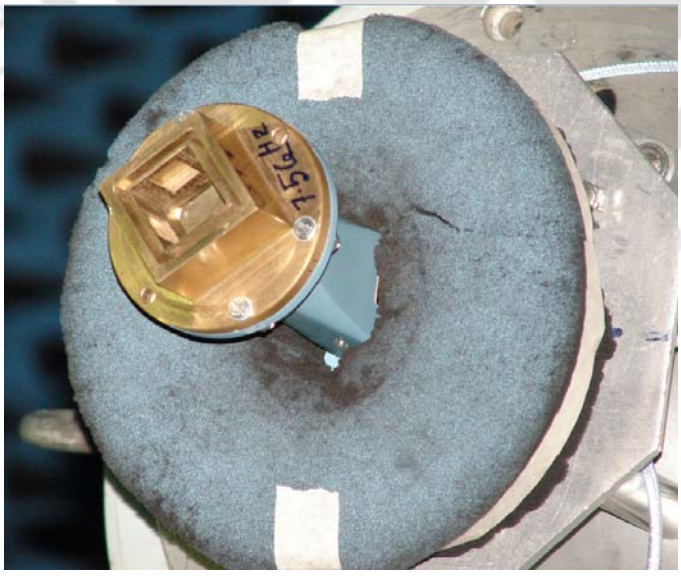

Figure 6.36: A figure of prototype matched feed structure during the measurement of far field patterns at anechoic chamber.

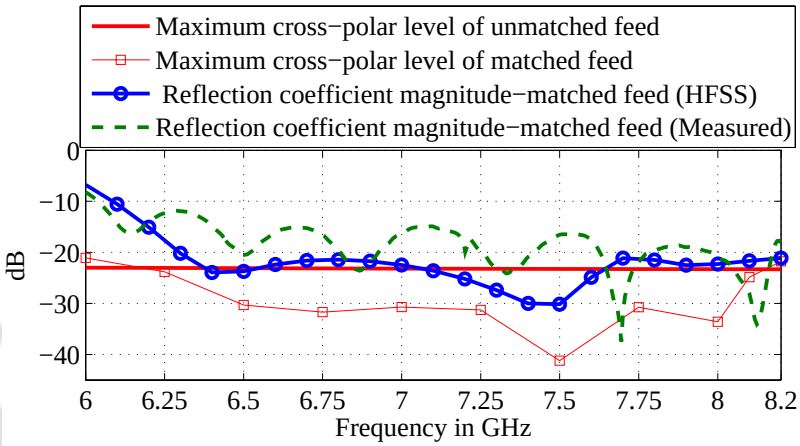

Figure 6.37: Cross-polar and impedance bandwidth of our proposed matched feed.

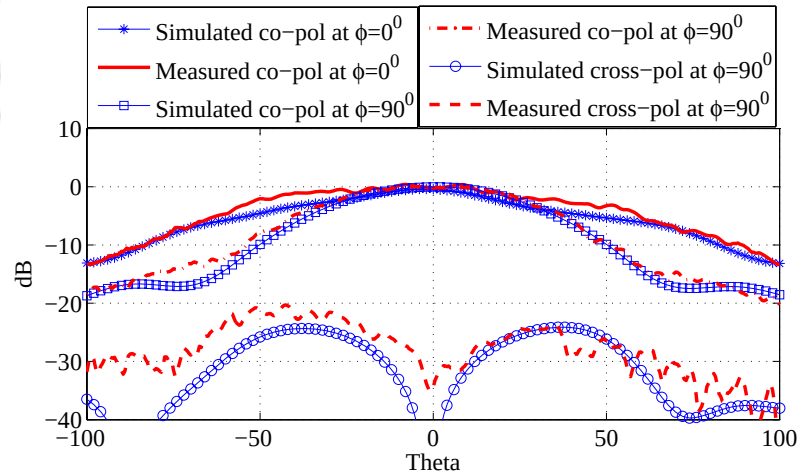

Figure 6.38: Normalized simulated and measured co-pol and cross-pol level at 7 GHz.

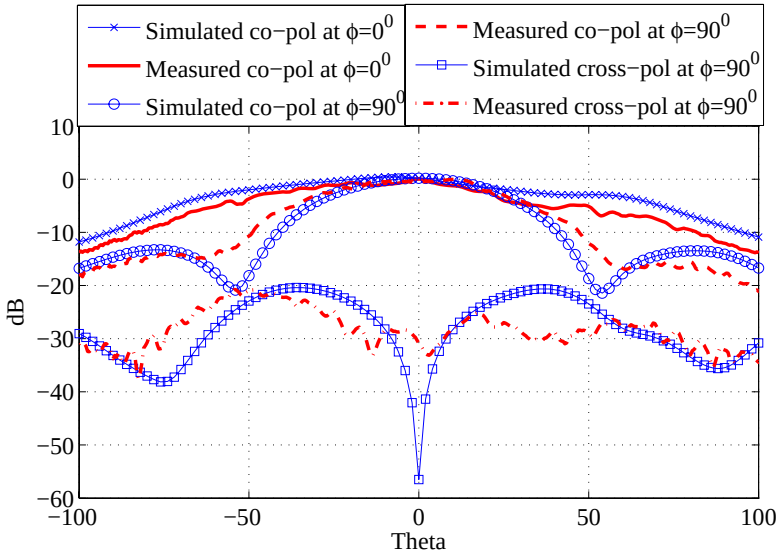

Figure 6.39: Normalized simulated and measured co-pol and cross-pol level at 7.5 GHz.

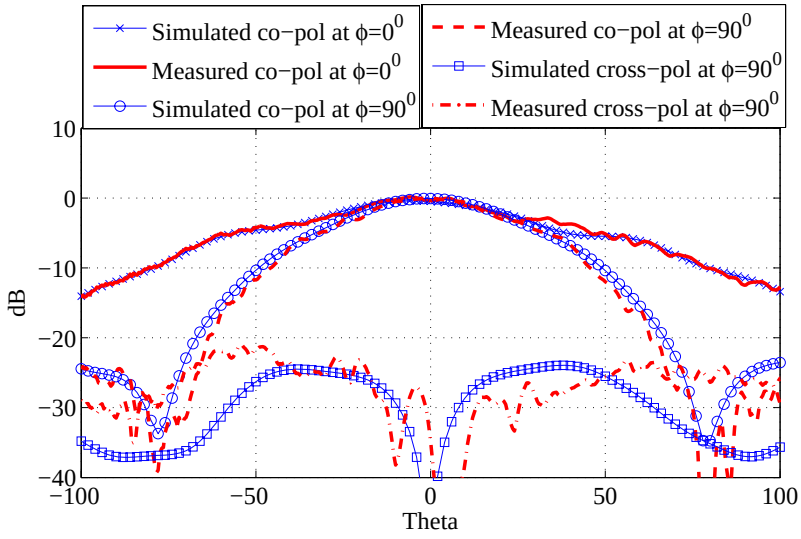

Figure 6.40: Normalized simulated and measured co-pol and cross-pol level at 8 GHz.

Table 6.9: Simulated and measured gain of our proposed matched feed.

Frequency in GHz	7	7.25	7.5	7.75	8
Simulated gain	8.7 dBi	9.1 dBi	8.1 dBi	9.7 dBi	9.7 dBi
Measured gain	7.5 dBi	9.4 dBi	8.5 dBi	9.1 dBi	9.6 dBi

are compared with simulated results of HFSS at the frequency 7, 7.5 and 8 GHz, respectively as shown in Fig. 6.38, 6.39, 6.40. As expected, simulated and measured far field patterns agree quite satisfactorily with each other for the considered test frequencies. Also, the measured and simulated gains of our proposed matched feed for several frequencies are compared in Table 6.9 and close agreements are obtained.

6.5 Conclusion

In this chapter, four novel matched feed structures have been proposed to remove the depolarization effect on an offset reflector. The basis of the design of such matched feed structures and the performance results as obtained through analytical and simulation studies are summarized below:

In the first feed structure, a dual mode smooth walled rectangular matched feed involving TE_{01} and TM_{11} modes have been presented in detail. The design of such feeds has not been dealt adequately in the available literature. The cross-polar performance of this dual mode horn as a matched feed for an offset reflector antenna has been evaluated both analytically as well through the simulation of the entire antenna system in HFSS. A -30 dB cross polar bandwidth of 130 MHz has been achieved at the design frequency of 6 GHz. The proposed feed structure is simple and it maintains good return loss performance over a wide band of frequencies.

In the second feed structure, a novel dual mode non-regular shape matched feed using TE_2 and TM_1 modes has been presented in detail. Design of such kind of feed aperture and its associated modes have not been dealt in the literature. The cross-polar performance has been investigated using semi-analytical technique and through HFSS/CST Microwave Studio simulation, and the results are in close agreement. Our proposed feed exhibits wideband characteristics since difference between cutoff wave number of TE_2 and TM_1 mode is kept less at the feed aperture. Final simulations are carried out using HFSS and a -30 dB cross-polar bandwidth of 545 MHz (8.79% fractional bandwidth) has been achieved.

In the third feed structure, a y polarized diagonal matched feed to suppress the depolarization effect of an offset reflector has been introduced. Such associated diagonal modes for the design of matched feed has not been addressed in the literature. Analytical models have been developed for matched feed design and performance enhancement is carried out using HFSS. In conventional design of matched feed, use of shorting post degrades return loss performance, while in our design of this diagonal feed, return loss improves with use of post. The proposed feed geometry can provide wide impedance as well as cross-polar bandwidth.

In the Fourth feed structure, a novel dual mode matched feed has been investigated for an offset reflector antenna to achieve the wide-band impedance and cross-polar bandwidth. Presented conjugate modes (TE_3, TE_4) associated with square choke of proposed matched feed to reduce the cross-polar power of an offset reflector antenna induced by main operating diagonal modes TE_H^D and TE_V^D, respectively have not been reported in any earlier study. Further, a practical feed realization has been carried out on the basis of operating modes TE_V^D and TE_4 for a given dimensions of an offset reflector antenna. Moreover, the main mode and the conjugate mode have been kept spatially separated so that they can be adjusted individually to achieve overall wide-band system design. It has been observed that required relative phase of TE_4 mode of our proposed matched feed could be easily maintained for wide-band conjugate matching. On the other hand, the required amount of TE_4 mode could be easily adjusted by varying the length and width of slots. Moreover, generation amount of TE_4 mode does not effect on impedance matching. Such characteristics are always desirable for a good matched feed.

7

Summary and Future Work

Contents

In this chapter, the summary of the works is presented and conclusions are drawn. Possible directions of extending some of these works are also discussed in the chapter.

7.1 Summary of Contribution

In this sub-section, the main contributions of the thesis are summarized as follows:

(A) **Development of a hybrid numerical technique to investigate the patterns of an offset reflector and its feed:** A hybrid method having low computational complexity has been developed using a combination of MM/2D-FEM/MoM techniques to study the performance of feeds which have been addressed in Chapter 2, Chapter 3 and Chapter 4. Finally, this numerically calculated feed pattern has been used to excite the reflector. The PO has been used for such large scatterer (reflector) to observe the reflector patterns which has been properly addressed in Chapter 5. The major issues which have been considered during the development of this hybrid technique and have been appropriately addressed in this thesis, are mentioned below:

(a) The closed form expressions of reaction matrix for different waveguide junctions for application of mode matching technique have been formulated.

(b) The presence of discontinuities inside the waveguide have been investigated using the combination of MM and 2D-FEM techniques.

(c) The open ended wave guide problem having finite ground plane has been formulated and solved using Kirchhoff-Huygen's principle based on 2D-MoM technique employing RWG function.

(d) The PO based technique to evaluate the reflector pattern has been developed.

(B) **Development of analytical and semi-analytical techniques and their application in the design of matched feed:** Analytical feed pattern of multi-mode horn has been calculated using the available analytical solution of Helmholtz equation. When an aperture contains a non-regular geometry or a regular geometry for which analytical solution of Helmholtz equation are not available, a numerical technique 2D-FEM has been used for the solution of mode fields and cutoff values. For such cases, radiation patterns of multi-mode horn have been calculated using numerical integration (barycentric subdivision four points) using the calculated mode fields and

cutoff values based on 2D-FEM technique. PO has been used to evaluate the reflector patterns, analytical or semi-analytical multi-mode feed pattern has been used to excite the reflector and PSO technique has been used for the estimation of required mode ratio and relative phase of conjugate mode to obtain the low cross-polar secondary pattern at the design frequency.

(C) **Proposed several novel matched feed structures to achieve the wideband characteristics:** Several novel matched feed structures have been proposed to eliminate the depolarization effects of offset reflector. Mostly, these have been introduced in the Chapter 5 and Chapter 6 of the thesis.

(a) A tri-mode ($TE_{11}^1 + TE_{21}^1 + TM_{11}^1$) circular matched feed using stepped junctions has been proposed for wideband operation and its performance has been investigated using the developed hybrid technique.

(b) A smooth walled rectangular matched feed operated with $TE_{01} + TM_{11}$ modes using shifted waveguide has been proposed and its performance has been reported in this thesis.

(c) A new kind of aperture which is an intersection of circular and rectangular surfaces, is used for wideband dual mode matched feed design where both operated modes have close cutoff frequencies. In this design, an x-polarized TE mode is used as the main operating mode and a TM mode as the conjugate mode.

(d) A diagonal matched feed structure using a post has been designed for the wideband on the basis of operated modes TE_H^D and TE_{11}^D.

(e) An appropriate conjugate field radiated from a square choke excited by two slots on a diagonal waveguide using the main operating mode TE_D^V has been proposed as a conjugate matched feed.

7.2 Suggestions for Future Research

Although in this thesis, efforts have been made to investigate the various aspects of matched feed design as exhaustively as possible, still there are many issues which could be investigated further and there exist a lot of scope for further extension of the works reported in this thesis. Some possible directions in which the present work can be extended are outlined below:

(a) In this thesis, attempts have been made to eliminate the depolarization effect of offset reflector using a single multi-mode feed horn. More degrees of freedom is available if muti-mode antenna array is used as matched feed. However, antenna array as a feed will increase the complexity of the system and the amount of computation that will be needed to analyze, model and design will be very high. Cross polar reduction through proper design of multi-mode feed array by developing techniques which are computationally less demanding can be a challenging work.

(b) As discussed, an efficient hybrid model for feed and reflector using MM/2D-FEM/MoM/PO has been developed to study the performance of a complete system. However, matched feed design has been carried out using manual intervention by fine tuning and through the parametric study to adjust the required mode ratio, and relative phase of conjugate mode in the feed aperture. Parametric study as well as fine tuning through manual intervention can be avoided using the developed methodology for the matched feed design combining proper probabilistic optimization technique along with MM/2D-FEM/MOM/PO technique. This work can be completed to realize an automated system.

(c) Investigations can be continued to find new matched feed geometries supporting multiple modes which do not involve complicated geometries and also do not occupy much space.

8

Appendix

Contents

8.1 Appendix A

The block matrix calculation of equation numbers (2.23), (2.24), (2.25) and (2.25) are given below:

$$\begin{pmatrix} -[A] & [I] \\ [B] & [0] \end{pmatrix}^{-1} \begin{pmatrix} [0] & [C] \\ [I] & -[D] \end{pmatrix} = \begin{pmatrix} [X] & [Y] \\ [Z] & [W] \end{pmatrix}$$

$$\begin{pmatrix} [0] & [C] \\ [I] & -[D] \end{pmatrix} = \begin{pmatrix} -[A] & [I] \\ [B] & [0] \end{pmatrix} \begin{pmatrix} [X] & [Y] \\ [Z] & [W] \end{pmatrix} = \begin{pmatrix} [-AX+Z] & [-AY+W] \\ [BX] & [BY] \end{pmatrix}$$

$$\begin{pmatrix} -[A] & [I] \\ [B] & [0] \end{pmatrix}^{-1} \begin{pmatrix} [0] & [C] \\ [I] & -[D] \end{pmatrix} = \begin{pmatrix} \left[B^{-1}\right] & \left[-B^{-1}D\right] \\ \left[AB^{-1}\right] & \left[C-AB^{-1}D\right] \end{pmatrix}$$

8.2 Appendix B

Surface integration of triangle:

$$u_1 = \frac{A_1}{A}, \quad u_2 = \frac{A_2}{A}, \quad u_3 = \frac{A_3}{A}$$

$$u_1 + u_2 + u_3 = 1$$

$$\iint g(r)ds = 2A \int_0^1 \int_0^{1-u_2} g\left[u_1(r_1 - r_3) + u_2(r_2 - r_3) + r_3\right] du_1 du_2$$

$$\iint u_1^l u_1^m u_1^n ds = \frac{l!m!n!2!A}{(l+m+n+2)!}$$

8.3 Appendix C

Global **C** and **T** matrix generation:

First step is to generate the local $\mathbf{C}^n$ and $\mathbf{T}^n$ matrix using equation 3.11 and 3.12 by considering the variation of ϕ as 1^{st} order polynomial for every element (n). As per the consideration of mesh surface in Figure 8.1, scaler function ϕ can be written as $\phi = [\phi_f^1 \quad \phi_p^2 \quad \phi_p^3 \quad \phi_p^4]$, where ϕ_f^1 is only one free node. Since, $\mathbf{C}^n$ and $\mathbf{T}^n$ are symmetric matrix as a result global **C** and **T** are also be symmetric matrix. The coefficients of global **C** and **T** are given below:

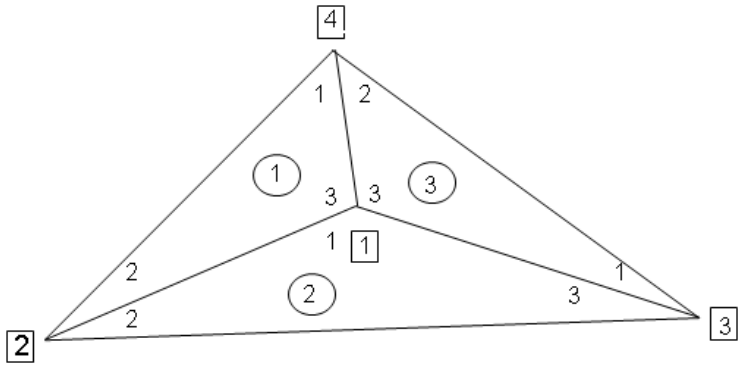

Figure 8.1: Discretization of a homogenous solution.

$$\mathbf{C}^n = \begin{bmatrix} C_{11}^{(n)} & C_{12}^{(n)} & C_{13}^{(n)} \\ C_{21}^{(n)} & C_{22}^{(n)} & C_{23}^{(n)} \\ C_{31}^{(n)} & C_{32}^{(n)} & C_{33}^{(n)} \end{bmatrix} \qquad \mathbf{T}^n = \begin{bmatrix} T_{11}^{(n)} & T_{12}^{(n)} & T_{13}^{(n)} \\ T_{21}^{(n)} & T_{22}^{(n)} & T_{23}^{(n)} \\ T_{31}^{(n)} & T_{32}^{(n)} & T_{33}^{(n)} \end{bmatrix}$$

$$\mathbf{C} = \begin{bmatrix} C_{11} & C_{12} & C_{13} & C_{14} \\ C_{21} & C_{22} & C_{23} & C_{24} \\ C_{31} & C_{32} & C_{33} & C_{34} \\ C_{41} & C_{42} & C_{43} & C_{44} \end{bmatrix} \qquad \mathbf{T} = \begin{bmatrix} T_{11} & T_{12} & T_{13} & T_{14} \\ T_{21} & T_{22} & T_{23} & T_{24} \\ T_{31} & T_{32} & T_{33} & T_{34} \\ T_{41} & T_{42} & T_{43} & T_{44} \end{bmatrix}$$

$$C_{11} = C_{33}^{(1)} + C_{11}^{(2)} + C_{33}^{(3)} \qquad T_{11} = T_{33}^{(1)} + T_{11}^{(2)} + T_{33}^{(3)}$$

$$C_{12} = C_{21} = C_{32}^{(1)} + C_{12}^{(2)} \qquad T_{12} = T_{21} = T_{32}^{(1)} + T_{12}^{(2)}$$

$$C_{13} = C_{31} = C_{13}^{(2)} + C_{31}^{(3)} \qquad T_{13} = T_{31} = T_{13}^{(2)} + T_{31}^{(3)}$$

$$C_{14} = C_{41} = C_{13}^{(1)} + C_{31}^{(3)} \qquad T_{14} = T_{41} = T_{13}^{(1)} + T_{31}^{(3)}$$

$$C_{22} = C_{22}^{(1)} + C_{22}^{(2)} \qquad T_{22} = T_{22}^{(1)} + T_{22}^{(2)}$$

$$C_{23} = C_{32} = 0 \qquad T_{23} = T_{32} = 0$$

$$C_{24} = C_{24} = C_{21}^{(1)} \qquad T_{24} = T_{24} = T_{21}^{(1)}$$

$$C_{33} = C_{33}^{(2)} + C_{11}^{(3)} \qquad T_{33} = T_{33}^{(2)} + T_{11}^{(3)}$$

$$C_{34} = C_{34} = C_{12}^{(3)} \qquad T_{34} = T_{34} = T_{12}^{(3)}$$

$$C_{44} = C_{11}^{(1)} + C_{22}^{(3)} \qquad T_{44} = T_{11}^{(1)} + T_{22}^{(3)}$$

भारतीय प्रौद्योगिकी संस्थान गुवाहाटी
Indian Institute of Technology Guwahati

Bibliography

[1] A. Rudge and N. Adatia, "Offset-parabolic-reflector antennas: A review," *Proceedings of the IEEE*, vol. 66, no. 12, pp. 1592–1618, Dec. 1978.

[2] W. Stutzman and M. Terada, "Design of offset-parabolic-reflector antennas for low cross-pol and low sidelobes," *Antennas and Propagation Magazine, IEEE*, vol. 35, no. 6, pp. 46–49, Dec 1993.

[3] T. S. Chu, "Cancellation of polarization rotation in an offset paraboloid by a polarization grid," *The Bell Sys. Tech., J.,*, vol. 56, no. 6, pp. 977 – 986, July 1977.

[4] E. Lier and S. Skyttemyr, "A shaped single reflector offset antenna with low cross-polarization fed by a lens horn," *Antennas and Propagation, IEEE Transactions on*, vol. 42, no. 4, pp. 478–483, Apr 1994.

[5] Z. Pour and L. Shafai, "A novel impedance matched mode generator for excitation of the {TE21} mode in compact dual-mode circular waveguide feeds," *Antennas and Wireless Propagation Letters, IEEE*, vol. 10, pp. 427–430, 2011.

[6] S. Sharma, D. Pujara, S. Chakrabarty, and V. Singh, "Improving the cross-polar performance of an offset parabolic reflector antenna using a rectangular matched feed," *Antennas and Wireless Propagation Letters, IEEE*, vol. 8, pp. 513 –516, 2009.

[7] K. Bahadori and Y. Rahmat-Samii, "Tri-mode horn feeds revisited: Cross-pol reduction in compact offset reflector antennas," *IEEE Transactions on Antennas and Propagation*, vol. 57, no. 9, pp. 2771–2775, Sept. 2009.

[8] S. Sharma, D. Pujara, S. Chakrabarty, and R. Dey, "Cross-polarization cancellation in an offset parabolic reflector antenna using a corrugated matched feed," *IEEE Antennas and Wireless Propagation Letters*, vol. 8, pp. 861–864, 2009.

[9] Z. Pour and L. Shafai, "A simplified feed model for investigating the cross polarization reduction in circular- and elliptical-rim offset reflector antennas," *Antennas and Propagation, IEEE Transactions on*, vol. 60, no. 3, pp. 1261–1268, March 2012.

[10] ——, "A ring choke excited compact dual-mode circular waveguide feed for offset reflector antennas," *Antennas and Propagation, IEEE Transactions on*, vol. 60, no. 6, pp. 3011–3015, June 2012.

[11] ——, "A novel dual-mode dual-polarized circular waveguide feed excited by concentrically shorted ring patches," *Antennas and Propagation, IEEE Transactions on*, vol. 61, no. 10, pp. 4917–4925, Oct 2013.

[12] R. Dey, S. Chakrabarty, and R. Sharma, "Broadband conjugate matched feed horn- a novel concept," *Antennas and Wireless Propagation Letters, IEEE*, vol. PP, no. 99, pp. 1–1, 2015.

[13] Z. Pour and L. Shafai, "Improved cross-polarization performance of a multi-phase-center parabolic reflector antenna," *Antennas and Wireless Propagation Letters, IEEE*, vol. 13, pp. 540–543, 2014.

[14] Z. Pour, L. Shafai, and B. Tabachnick, "A practical approach to locate offset reflector focal point and antenna misalignment using vectorial representation of far-field radiation patterns," *Antennas and Propagation, IEEE Transactions on*, vol. 62, no. 2, pp. 991–996, Feb 2014.

[15] Z. Pour and L. Shafai, "Investigation of asymmetric phase errors of an optimized dual-mode primary feed on the cross polarization of offset reflector antennas," *Antennas and Wireless Propagation Letters, IEEE*, vol. 9, pp. 872–875, 2010.

[16] R. Bunger and F. Arndt, "Moment-method analysis of arbitrary 3-d metallic n-port waveguide structures," *Microwave Theory and Techniques, IEEE Transactions on*, vol. 48, no. 4, pp. 531–537, Apr 2000.

[17] F. Arndt, J. Brandt, V. Catina, J. Ritter, I. Rullhusen, J. Dauelsberg, U. Hilgefort, and W. Wessel, "Fast cad and optimization of waveguide components and aperture antennas by hybrid mm/fe/mom/fd methods-state-of-the-art and recent advances," *Microwave Theory and Techniques, IEEE Transactions on*, vol. 52, no. 1, pp. 292–305, 2004.

[18] R. Beyer and F. Arndt, "Efficient modal analysis of waveguide filters including the orthogonal mode coupling elements by an mm/fe method," *Microwave and Guided Wave Letters, IEEE*, vol. 5, no. 1, pp. 9 –11, jan 1995.

[19] Y. Rahmat-Samii, D.-W. Duan, D. Giri, and L. Libelo, "Canonical examples of reflector antennas for high-power microwave applications," *Electromagnetic Compatibility, IEEE Transactions on*, vol. 34, no. 3, pp. 197 –205, aug 1992.

[20] M. Terada and W. Stutzman, "Computer-aided design of reflector antennas: the green bank radio telescope," *Microwave Theory and Techniques, IEEE Transactions on*, vol. 46, no. 3, pp. 250–253, Mar 1998.

[21] S. Silver, *Microwave Antenna Theory and Design.*, 3rd ed. New York: McGraw Hill, 1949.

[22] W. A. T. Rusch and P. Potter, *Analysis of Reflector Antennas.* New York: Academic Press, 1970.

[23] A. W. Rudge, K. Milne, A. D. Olver, and P. Knight, *The Handbook of Antenna Design.* London: Peter Peregrinus Ltd., 1982.

[24] Y. T. Lo and S. W. Lee, *Antenna Handbook.* London: Springer., 1993.

[25] Scott., *Modern Methods of Reflector Antenna Analysis and Design.* Norwood, MA: Artech House,, 1993.

[26] W. A. Imbriale, *Spaceborne Antennas for Planetary Exploration,.* Hoboken, NJ.: JohnWiley & Sons, 2006.

[27] N. Adatia and A. Rudge, "Beam squint in circularly polarised offset-reflector antennas," *Electronics Letters*, vol. 11, no. 21, pp. 513 –515, october 1975.

[28] Z. Pour and L. Shafai, "Reducing crosspolarization of an offset reflector antenna using a dual-mode horn feed," in *Antenna Technology and Applied Electromagnetics and the Canadian Radio Science Meeting, 2009. ANTEM/URSI 2009. 13th International Symposium on*, 15-18 2009, pp. 1 –4.

[29] Y. Rahmat-Samii, "Array feeds for reflector surface distortion compensation: concepts and implementation," *Antennas and Propagation Magazine, IEEE*, vol. 32, no. 4, pp. 20 –26, aug 1990.

[30] M. N. O. Sadiku, *Numerical techniques in electromagnetics*, 2nd ed. New York, Washington D.C: CRC press LLC, 2001.

[31] R. Thabet and L. M. Riabi, "Rigorous design and efficient optimization of quarter-wave transformers in metaric circular waveguides using the mode-matching method and the genetic algorithm," *Progress in Electromagnetics Research*, vol. 68, pp. 15–33, Sept. 2007.

[32] R. Bunger, R. Beyer, and F. Arndt, "Rigorous combined mode-matching integral equation analysis of horn antennas with arbitrary cross section," *IEEE Transaction on Antenna and Propagation*, vol. 47, no. 11, pp. 1641–1648, Nov. 1999.

[33] G. S. Diamantis, P. A. Orfanidis, and A. G. Kyriacou, "Conical horn antennas employing an offset moment method and mode matching technique," *IEEE Transaction on Magnetics*, vol. 45, no. 3, pp. 1092–1095, March 2009.

[34] A. Wexler, "Solution of waveguide discontinuities by modal analysis," *IEEE Transactions on Microwave Theory and Techniques*, vol. 15, no. 9, pp. 508–517, Sept. 1967.

[35] J. Reiter, M and F. Arndt, "A boundary contour mode-matching method for the rigorous analysis of cascaded arbitrarily shaped h-plne discontinuities in rectangular waveguides," *IEEE Microwaves and Guide Wave Letters*, vol. 2, no. 10, pp. 403–405, Oct. 1992.

[36] D. J. Hoppe, "Modal analysis applied to circular, rectangular and coaxial waveguides," Radio Frequency and Microwave Subsystems Section, Tech. Rep., July-September 1988.

[37] R. E. Collin, *Field Theory of guided waves*, 1st ed. New York: McGraw Hill, 1960.

[38] R. Mittra and S. Lee, W, *Analytical Techniques in the Theorey of guided waves.*, 1st ed. New York: Collier-Macmillan Limited, 1971.

[39] R. F. Harrington, *Time-Harmonic Electromagnetic Fields*, 1st ed. New York: IEE Press and Wiley Interscience, 1961.

[40] F. Arndt and J. Brandt, "Direct em based optimization of advanced waffle-iron and rectangular combline filters," in *Microwave Symposium Digest, 2002 IEEE MTT-S International*, vol. 3, 2002, pp. 2053–2056 vol.3.

[41] ——, "Mm/fe cad and optimization of rectangular combline filters," in *Microwave Conference, 2002. 32nd European*, sept. 2002, pp. 1 –4.

[42] F. Alessandri, G. Bartolucci, and R. Sorrentino, "Admittance matrix formulation of waveguide discontinuity problems: computer-aided design of branch guide directional couplers," *Microwave Theory and Techniques, IEEE Transactions on*, vol. 36, no. 2, pp. 394–403, 1988.

[43] M. Yahia, J. Tao, H. Benzina, and M.-N. Abdelkrim, "Analysis of complex rectangular waveguide discontinuities using hybrid mvm-fem." in *Microwave Conference, 2009. APMC 2009. Asia Pacific*, 2009, pp. 111–114.

[44] R. Lotz and F. Arndt, "Fd-fd gsm technique for the cad and optimization of combline filters," in *Microwave Symposium Digest, 2001 IEEE MTT-S International*, vol. 2, 2001, pp. 1253–1256 vol.2.

[45] H.-W. Yao, K. Zaki, A. Atia, and R. Hershtig, "Full wave modeling of conducting posts in rectangular waveguides and its applications to slot coupled combline filters," *Microwave Theory and Techniques, IEEE Transactions on*, vol. 43, no. 12, pp. 2824–2830, 1995.

[46] Y. Rong and K. Zaki, "Full-wave analysis of coupling between cylindrical combline resonators," *Microwave Theory and Techniques, IEEE Transactions on*, vol. 47, no. 9, pp. 1721–1729, 1999.

[47] A. Rong, H. Yang, X. H. Chen, and A. Cangellaris, "Efficient fdtd modeling of irises/slots in microwave structures and its application to the design of combline filters," *Microwave Theory and Techniques, IEEE Transactions on*, vol. 49, no. 12, pp. 2266–2275, 2001.

[48] V. Crino, C. Tomassoni, M. Mongiardo, and A. Omar, "Hybrid full-wave analysis of stepped horn antennas with waveguides of arbitrary cross-sections," in *Microwave Conference, 2004. 34th European*, vol. 2, 2004, pp. 597–600.

[49] G. Figlia and G. Gentili, "On the line-integral formulation of mode-matching technique," *Microwave Theory and Techniques, IEEE Transactions on*, vol. 50, no. 2, pp. 578–580, 2002.

[50] G. Gentili, "Properties of te-tm mode-matching techniques," *Microwave Theory and Techniques, IEEE Transactions on*, vol. 39, no. 9, pp. 1669–1673, 1991.

[51] M. Bozzi, G. Conciauro, and L. Perregrini, "On the evaluation of modal coupling coefficients by contour integrals," *Microwave Theory and Techniques, IEEE Transactions on*, vol. 50, no. 7, pp. 1853–1855, 2002.

[52] V. Crino, C. Tomassoni, and M. Mongiardo, "Line-integral formulation of the hybrid mm/fem technique," in *Microwave Symposium Digest, 2002 IEEE MTT-S International*, vol. 3, 2002, pp. 2033–2036 vol.3.

[53] D. B. Davidson, *Computational Electromagnetics for RF and Microwave Engineering*, 2nd ed. Cambridge Univercity Press, April 2011.

[54] J. M. JIN, *Theory and Computation of Electromagnetics Fields.* John Wiley & Sons, Inc., Hoboken, New Jersey, May 2010.

[55] Wikipedia. [Online]. Available: https://en.wikipedia.org/wiki/Delaunay_triangulation

[56] P. Ratajczak, P. Brachat, and J.-L. Guiraud, "Rigorous analysis of three-dimensional structures incorporating dielectrics," *Antennas and Propagation, IEEE Transactions on*, vol. 42, no. 8, pp. 1077 –1088, Aug 1994.

[57] P. Tirkas and C. Balanis, "Finite-difference time-domain method for antenna radiation," *Antennas and Propagation, IEEE Transactions on*, vol. 40, no. 3, pp. 334 –340, Mar 1992.

[58] M. Catedra, "Analysis of bodies of revolution composed of conductors and dielectrics using only electric equivalent currents: application to small horns with dielectric core," *Antennas and Propagation, IEEE Transactions on*, vol. 36, no. 9, pp. 1311 –1313, Sep 1988.

[59] J. Reiter and F. Arndt, "Full-wave analysis of circular waveguide horn antennas including the outer wall geometry with an hybrid mm/bcmm method," in *Antennas and Propagation Society International Symposium, 1996. AP-S. Digest*, vol. 3, Jul 1996, pp. 1984 –1987 vol.3.

[60] C. A. Balanis, *Antenna Theory: Analysis and Design, 3rd Edition*, 3rd ed. Wiley-Interscience, April 2005.

[61] J. Encinar and J. Rebollar, "A hybrid technique for analyzing corrugated and noncorrugated rectangular horns," *Antennas and Propagation, IEEE Transactions on*, vol. 34, no. 8, pp. 961 – 968, Aug 1986.

[62] J. Yu, R. Rudduck, and J. Peters, L., "Comprehensive analysis for e-plane of horn antennas by edge diffraction theory," *Antennas and Propagation, IEEE Transactions on*, vol. 14, no. 2, pp. 138 – 149, Mar 1966.

[63] T. Wang, R. Harrington, and J. Mautz, "Electromagnetic scattering from and transmission through arbitrary apertures in conducting bodies," *Antennas and Propagation, IEEE Transactions on*, vol. 38, no. 11, pp. 1805 –1814, nov 1990.

[64] K. Liu, C. Balanis, C. Birtcher, and G. Barber, "Analysis of pyramidal horn antennas using moment methods," *Antennas and Propagation, IEEE Transactions on*, vol. 41, no. 10, pp. 1379 –1389, oct 1993.

[65] R. Bunger, R. Beyer, and F. Arndt, "Rigorous combined mode-matching integral equation analysis of horn antennas with arbitrary cross section," *Antennas and Propagation, IEEE Transactions on*, vol. 47, no. 11, pp. 1641 –1648, nov 1999.

[66] T. Wriedt, K.-H. Wolff, F. Arndt, and U. Tucholke, "Rigorous hybrid field theoretic design of stepped rectangular waveguide mode converters including the horn transitions into half-space," *Antennas and Propagation, IEEE Transactions on*, vol. 37, no. 6, pp. 780 –790, Jun 1989.

[67] S. Rao, D. Wilton, and A. Glisson, "Electromagnetic scattering by surfaces of arbitrary shape," *Antennas and Propagation, IEEE Transactions on*, vol. 30, no. 3, pp. 409 – 418, may 1982.

[68] W. C. Gibson, *The Method of Moments in Electromagnetics*, 1st ed. Broken Sound Parkway NW: Chapman and Hall/CRC, 2008.

[69] H. Auda and R. Harrington, "A moment solution for waveguide junction problems," *Microwave Theory and Techniques, IEEE Transactions on*, vol. 31, no. 7, pp. 515 –520, jul. 1983.

[70] T. Eibert and V. Hansen, "On the calculation of potential integrals for linear source distributions on triangular domains," *Antennas and Propagation, IEEE Transactions on*, vol. 43, no. 12, pp. 1499 –1502, dec 1995.

[71] D. Taylor, "Accurate and efficient numerical integration of weakly singular integrals in galerkin efie solutions," *Antennas and Propagation, IEEE Transactions on*, vol. 51, no. 7, pp. 1630 – 1637, july 2003.

[72] J. Yuan, C. Gu, and G. Han, "Efficient generation of method of moments matrices using equivalent dipole-moment method," *Antennas and Wireless Propagation Letters, IEEE*, vol. 8, pp. 716 –719, 2009.

[73] A. Ludwig, "The definition of cross polarization," *IEEE Transactions on Antennas and Propagation*, vol. 21, no. 1, pp. 116–119, Jan. 1973.

[74] TICRA's GRASP 7.0 Software, TICRA Engineering Consultants, Copenhagen, Denmark.

[75] J. Kennedy and R. Eberhart, "Particle swarm optimization," in *Neural Networks, 1995. Proceedings., IEEE International Conference on*, vol. 4, 1995, pp. 1942–1948 vol.4.

[76] R. Eberhart and J. Kennedy, "A new optimizer using particle swarm theory," in *Micro Machine and Human Science, 1995. MHS '95., Proceedings of the Sixth International Symposium on*, 1995, pp. 39–43.

[77] J. Robinson and Y. Rahmat-Samii, "Particle swarm optimization in electromagnetics," *Antennas and Propagation, IEEE Transactions on*, vol. 52, no. 2, pp. 397 – 407, feb. 2004.

[78] N. Jin and Y. Rahmat-Samii, "Parallel particle swarm optimization and finite- difference time-domain (pso/fdtd) algorithm for multiband and wide-band patch antenna designs," *Antennas and Propagation, IEEE Transactions on*, vol. 53, no. 11, pp. 3459–3468, 2005.

[79] M. Capek and P. Hazdra, "Design of ifs patch antenna using particle swarm optimization," in *Antennas and Propagation (EuCAP), 2010 Proceedings of the Fourth European Conference on*, 2010, pp. 1–5.

[80] M. Islam, N. Misran, T. Take, and M. Moniruzzaman, "Optimization of microstrip patch antenna using particle swarm optimization with curve fitting," in *Electrical Engineering and Informatics, 2009. ICEEI '09. International Conference on*, vol. 02, 2009, pp. 711–714.

[81] A. Modiri and K. Kiasaleh, "Efficient design of microstrip antennas using modified pso algorithm," in *Electromagnetic Field Computation (CEFC), 2010 14th Biennial IEEE Conference on*, 2010, pp. 1–1.

[82] X.-L. Mao, H.-L. Zheng, and X.-H. Fan, "An optimization algorithm in shaped-beam antenna arrays," in *Synthetic Aperture Radar, 2009. APSAR 2009. 2nd Asian-Pacific Conference on*, 2009, pp. 571–574.

[83] B. Yang, X. Zhuge, A. Yarovoy, and L. Ligthart, "Uwb mimo antenna array topology design using pso for through dress near-field imaging," in *Radar Conference, 2008. EuRAD 2008. European*, 2008, pp. 463–466.

[84] Y. Shi and R. Eberhart, "Empirical study of particle swarm optimization," in *Evolutionary Computation, 1999. CEC 99. Proceedings of the 1999 Congress on*, vol. 3, 1999, pp. –1950 Vol. 3.

[85] M. Clerc and J. Kennedy, "The particle swarm - explosion, stability, and convergence in a multidimensional complex space," *Evolutionary Computation, IEEE Transactions on*, vol. 6, no. 1, pp. 58–73, 2002.

[86] D. Pujara and S. B. Chakrabarty, "Cancellation of high cross-polarization of an offset parabolic reflector antenna using a rectangular matched feed," *IETE Journal of Research*, vol. 58, no. 4, pp. 317–321, 2012. [Online]. Available: http://www.tandfonline.com/doi/abs/10.4103/0377-2063.102312

[87] G. F. Koch, "Coaxial feeds for high aperture efficiency and low spillover of paraboloidal reflector antennas," *Antennas and Propagation, IEEE Transactions on*, vol. AP, no. 21, pp. 164–169, Mar 1973.

[88] L. Gruner, "Higher order modes in rectangular coaxial waveguides," *Microwave Theory and Techniques, IEEE Transactions*, vol. 15, no. 8, pp. 483–485, August 1967.

[89] O. Cruzan and R. Garver, "Characteristic impedance of rectangular coaxial transmission lines," *Microwave Theory and Techniques, IEEE Transactions on*, vol. 12, no. 5, pp. 488–495, Sep 1964.